EFFECTS OF SINTERING ADDITIVE, MICROSTRUCTURE AND PROTON IRRADIATION ON THERMAL CONDUCTIVITY OF SPARK PLASMA SINTERED SIC CERAMICS

A thesis submitted to The University of Manchester for the degree of

Doctor of Philosophy

in the Faculty of Science and Engineering

2020

ZHENFEI CHAI

SCHOOL OF NATURAL SCIENCES

List of Contents

Word Count: 53363.

List of Figures

Chapter 2

Chapter 3

List of Tables

Chapter 2

Chapter 3

List of Abbreviations

Al_2O_3	alumina	HPS	hot pressing sintering
BSE	backscattered electron	LPS	liquid phase sintering
CFS	cation field strength	MD	molecular dynamics
CVD	chemical vapor deposition	NEMD	nonequilibrium molecular dynamics
DFT	density functional theory	PKA	primary knock-on atom
dpa	displacements per atom	Sc_2O_3	scandia
DSC	differential scanning calorimetry	SEM	scanning electron microscopy
EDS	energy dispersive X-ray spectroscopy	SiC	silicon carbide
EELS	electron energy loss spectroscopy	SPS	spark plasma sintering
FIB	focused ion beam	SRIM	stopping and range of ions in materials
GIXRD	grazing incidence X-ray diffraction	STEM	scanning transmission electron microscopy
GOF	goodness of fit	TEM	transmission electron microscopy
HAADF	high-angle annular dark-field	Y_2O_3	yttria
HRTEM	high-resolution transmission electron microscopy	XRD	X-ray diffraction

List of Publication

Z. Chai, Z. Gao, H. Liu, X. Zhang, G. Glodan, P. Xiao, Thermal conductivity of spark plasma sintered SiC ceramics with Alumina and Yttria, Journal of the European Ceramic Society 41(6) (2021) 3264-3273.

Abstract

Effects of Sintering Additive, Microstructure and Proton Irradiation on Thermal Conductivity of Spark Plasma Sintered SiC Ceramics

Zhenfei Chai

The University of Manchester for the degree of Doctor of Philosophy in Materials Science

2020

Silicon carbide (SiC) has very wide applications (e.g. heat exchangers, mechanical seals, cladding material, etc.) due to its high thermal conductivity, excellent high temperature strength, good oxidation resistance, and high radiation resistance. For those applications, thermal conductivity of SiC ceramics is an important property which however varies from 32 W/(m•K) to 490 W/(m•K) depending on microstructure. To further understand the effects of fabrication conditions on microstructure of SiC ceramics and dependence of thermal conductivity on microstructure, SiC ceramics were sintered by spark plasma sintering (SPS) with two different liquid phase sintering additives. Aside from that, SiC ceramics without sintering additive were also fabricated by SPS and subsequently irradiated by proton at 340 °C and different damage levels. Microstructure evolution and thermal conductivity degradation of the irradiated SiC were investigated and correlated.

In the SiC sintered with 3-10 wt.% Al_2O_3-Y_2O_3, an increase in the sintering additive content results in decrease in grain size and thermal conductivity of the SiC. Lower thermal conductivity of the SiC ceramic with higher sintering additive content is mainly due to smaller grain size rather than low intrinsic thermal conductivity of secondary phase. For the SiC sintered with same content of sintering additive and different holding time, increase in holding time has little influence on grain size but results in formation of continuous network of sintering additive in the SiC. Such continuous network of the sintering additive leads to increase of interfacial thermal resistance and thus decreases thermal conductivity.

In the SiC sintered with Y_2O_3-Sc_2O_3 at 1750-1850 ºC, the dominant grain growth mechanism changes from interface reaction at 1750 ºC to atom diffusion at 1850 ºC. Moreover, grain growth of the SiC sintered with Y_2O_3-Sc_2O_3 not only reduces the number of grain boundary per unit volume but also results in lattice purification originating from removing oxygen impurity of starting SiC powders by Y_2O_3-Sc_2O_3, which is suggested to be responsible for higher thermal conductivity of SiC ceramics with a larger grain size.

In the SiC sintered without sintering additive, the unit cell volume expansion and significant thermal conductivity reduction are observed after receiving proton irradiation at different damage level, which have been correlated with point defects and interstitial clusters induced by proton irradiation. It is suggested that interstitial-type defects make dominant contribution to unit cell volume expansion while vacancy-type defects and interstitial clusters are responsible for significant thermal conductivity degradation. Furthermore, higher damage level leads to higher volume expansion and lower thermal conductivity but variation extent of volume expansion and thermal conductivity at high damage level are smaller than that at low damage level, indicating more contribution from interstitial clusters at high damage level.

Declaration

No portion of the work referred to in the thesis has been submitted in support of an application for another degree or qualification of this or any other university or institution of learning.

Copyright Statement

Acknowledgements

Firstly, I would like to express sincere gratitude to my supervisor, Prof. Ping Xiao, for his supervision, encouragement and support on my PhD project over last four years. Besides, I would like to thank him for covering tuition fee during my PhD study.

Secondly, special thanks are given to the experimental officer, Dr Gyorgyi Glodan whose technical expertise, efforts and patience with the SPS equipment were essential for this PhD project. Also, I want to thank other experimental officers and technicians in Department of Materials for their valuable support on my project, Mr. Andy Wallwork and Mr. Andrew Forrest for thermal conductivity measurement, Mr. Matthew Smith, Dr. Teruo Hashimoto, Dr. Duc-The Ngo, Mr. Patrick Hill and Mr. Michael Faulkner for electron microscopy characterization, Dr. John Warren and Mr. Gary Harrison for XRD test, Mr. Kenneth Gyves, Dr. Xiangli Zhong, and Dr. Ali Gholinia for sample preparation training, Dr Samir de Moraes Shubeita and Dr Andrew Smith for proton irradiation experiments.

Thirdly, I would like to specially thank my senior colleague, Dr. Han Liu and Dr. Zhaohe Gao who gave me valuable suggestions and discussions for my project. Also, I would like to thank my colleagues, Dr. Xun Zhang, Dr Ying Chen and Dr. Nadia Rohbeck who gave me help and encouragement for my project. The accompanies and support of all members in our group are also appreciated and necessary for my PhD project. Furthermore, I would like to thank China Scholarship Council for its financial support on living expense during my PhD study.

Last but not least, I would like to thank my family for their endless love and support.

Chapter 1 Introduction

1.1 Research background

Silicon carbide (SiC) possess a number of excellent properties including high thermal conductivity (490 W/(m•K)), excellent high temperature strength, high wear resistance, good oxidation resistance to air and steam, and high corrosion resistance [1-6], which make it suitable in many fields, such as heat exchangers, mechanical seals, bearing, nozzles and so on [7-9]. For those applications, thermal conductivity is an important property and strongly influenced by microstructure of SiC ceramics. Diverse microstructure originating from different fabrication conditions results in huge variation in thermal conductivity (from 32 W/(m•K) to 490 W/(m•K)) of SiC ceramics [10-13]. Hence, it is necessary to understand effects of fabrication conditions on microstructure and dependence of thermal conductivity on resultant microstructure.

Due to great difficulties in densification of SiC which has extremely low self-diffusion coefficient and high fraction (88%) of covalent bonds, liquid phase sintering additives (e.g. Al_2O_3-Y_2O_3, Al_2O_3-Y_2O_3-CaO, AlN-Y_2O_3, Y_2O_3-Sc_2O_3, Y_2O_3-Sc_2O_3-MgO, etc), conventional sintering techniques (e.g. hot pressing sintering, gas pressure sintering, etc), or novel sintering technique such as spark plasma sintering (SPS), have been adopted to dramatically reduce sintering temperature for fabricating dense SiC ceramics [14-20]. Until now, there are very limited number of studies which combine SPS and liquid sintering additive to densify SiC ceramics and underlying mechanism about densification and grain growth of spark-plasma sintered SiC ceramics in the presence of liquid phase sintering additive remains unclear [16, 21].

Sintering additive has significant effects on both microstructure and thermal conductivity of sintered SiC ceramics. Firstly, sintering additive can effectively remove pores which could decrease thermal conductivity of sintered ceramics. The decrease in thermal conductivity was influenced by volume fraction, shape and spatial distribution of pores [22-24]. Besides, the presence of pores could change heat transfer mechanism in solid ceramics (especially in porous ceramics). Heat transfer is dominated by heat conduction at low temperature while the contribution of radiation to heat transfer

becomes prominent at high temperature (especially for ceramics containing pores of micrometer scale) [25, 26]. Secondly, sintering additive can change microstructure of sintered SiC ceramics by modifying grain size of SiC matrix, phase composition and distribution which could further influence thermal conductivity [19, 27-29]. Thirdly, sintering additives in the sintered SiC ceramics not only have intrinsically lower thermal conductivity than that of SiC matrix but also introduce interface with SiC which can alter thermal conductivity of sintered SiC ceramics [27, 30]. However, importance of porosity, grain size, sintering additive content/distribution as well as the interface between sintering additive and SiC on thermal conductivity of sintered SiC ceramics has not been thoroughly investigated, especially in cases where multiple factors are simultaneously affecting heat conduction in SiC ceramics.

Aside from microstructure changes of SiC ceramics caused by the sintering additive during fabrication process, dramatic microstructure evolution (e.g. irradiation induced segregation, amorphization and/or swelling of crystalline SiC) could take place under special environment (e.g. neutron and ion irradiation) [31-35]. SiC and SiC fiber-reinforced SiC matrix composites (SiC_f/SiC composites) were regarded as one type of very promising candidate of cladding material in nuclear reactors because of low thermal neutron absorption cross section, high thermal conductivity (320 W/(m•K) for 3C-SiC) and good radiation resistance [31, 36-38]. As SiC is exposed to neutron irradiation environment, the irradiation induced defects/defect clusters were responsible for serious thermal conductivity degradation [32, 39, 40]. Thermal conductivity of cladding materials is a crucial factor controlling heat transfer in nuclear reactors [41]. Hence, a deep understanding about underlying mechanism of microstructure evolution and thermal conductivity degradation of SiC after irradiation is required in terms of safety operation and efficient heat transfer of nuclear reactors.

1.2 Objectives and structure of dissertation

This project aims to further understand influence of microstructure on thermal conductivity of SiC ceramics sintered by SPS with and without liquid phase sintering additive. Effects of sintering additive content/distribution, interface between SiC and sintering additive, grain size and irradiation induced

damage on thermal conductivity of sintered SiC ceramics have been investigated. Structure of this dissertation is organized as below:

In chapter 2, sintering of dense SiC ceramics and microstructure development of liquid phase sintered SiC ceramics are reviewed. Also, fundamental of heat conduction and correlation between microstructure and thermal conductivity of SiC ceramics are reviewed. In addition, irradiation effects on microstructure and thermal conductivity are reviewed.

Chapter 3 are composed of 3 articles: Article I studies thermal conductivity of spark plasma sintered SiC ceramics with 3-10 wt.% Al_2O_3-Y_2O_3. Effects of fabrication conditions on microstructure and dependence of thermal conductivity on sintering additive content/distribution, interface and grain size are investigated, compared and discussed; Article II deals with grain growth of spark plasma sintered SiC ceramics with Y_2O_3-Sc_2O_3, which aims to further understanding about grain growth during SPS process in the presence of liquid phase sintering additive. Moreover, grain growth is correlated with thermal conductivity change; In Article III, proton irradiation is firstly adopted to investigate evolution of microstructure and thermal conductivity of sintered SiC ceramics without sintering additive at irradiation temperature of 340 °C and different damage levels, which may provide useful information for comparing proton irradiation with neutron irradiation in SiC.

Chapter 4 summarizes main conclusions of the dissertation and future work.

References

[1] G.A. Slack, Thermal conductivity of pure and impure silicon, silicon carbide, and diamond, Journal of Applied physics 35(12) (1964) 3460-3466.

[2] X. Duan, H. Zheng, Y. Chen, F. Qian, G. Liu, X. Wang, Y. Si, Study on the corrosion resistance of cordierite-mullite and SiC refractories to Li-ion ternary cathode materials, Ceramics International 46(3) (2020) 2829-2835.

[3] P.A. Mouche, K.A. Terrani, Steam pressure and velocity effects on high temperature silicon carbide oxidation, Journal of the American Ceramic Society 103(3) (2020) 2062-2075.

[4] Y.-W. Kim, S.H. Jang, T. Nishimura, S.-Y. Choi, S.-D. Kim, Microstructure and high-temperature strength of silicon carbide with 2000 ppm yttria, Journal of the European Ceramic Society 37(15) (2017) 4449-4455.

[5] R. Krishnarao, M.Z. Alam, D. Das, In-situ formation of SiC, ZrB_2-SiC and ZrB_2-SiC-B_4C-YAG coatings for high temperature oxidation protection of C/C composites, Corrosion Science 141 (2018) 72-80.

[6] B. Li, B. Mao, X. Wang, T. He, Fabrication and frictional wear property of bamboo-like SiC nanowires reinforced SiC coating, Surface and Coatings Technology (2020) 125647.

[7] M. Steen, L. Ranzani, Potential of SiC as a heat exchanger material in combined cycle plant, Ceramics international 26(8) (2000) 849-854.

[8] J. Ness, T. Page, Microstructural evolution in reaction-bonded silicon carbide, Journal of Materials Science 21(4) (1986) 1377-1397.

[9] H.-J. Choi, H.-T. Bae, J.-K. Lee, B.-C. Na, M. McNallan, D.-S. Lim, Sliding wear of silicon carbide modified by etching with chlorine at various temperatures, Wear 266(1-2) (2009) 214-219.

[10] G.A. Slack, Nonmetallic crystals with high thermal conductivity, Journal of Physics and Chemistry of Solids 34(2) (1973) 321-335.

[11] J.H. Eom, Y.K. Seo, Y.W. Kim, Mechanical and thermal properties of pressureless sintered silicon carbide ceramics with alumina–yttria–calcia, Journal of the American Ceramic Society 99(5) (2016) 1735-1741.

[12] T. Sakai, T. Aikawa, Phase Transformation and Thermal Conductivity of Hot-Pressed Silicon Carbide Containing Alumina and Carbon, Journal of the American Ceramic Society 71(1) (1988) C-7-C-9.

[13] K. Watari, H. Nakano, K. Sato, K. Urabe, K. Ishizaki, S. Cao, K. Mori, Effect of grain boundaries on thermal conductivity of silicon carbide ceramic at 5 to 1300 K, Journal of the American Ceramic Society 86(10) (2003) 1812-1814.

[14] K.J. Kim, K.Y. Lim, Y.W. Kim, Control of electrical resistivity in silicon carbide ceramics sintered with aluminum nitride and yttria, Journal of the American Ceramic Society 96(11) (2013) 3463-3469.

[15] R. Malik, Y.-H. Kim, Y.-W. Kim, Effect of additive content on the mechanical and thermal properties of pressureless liquid-phase sintered SiC, Journal of Asian Ceramic Societies 8(2) (2020) 448-459.

[16] Y.K. Seo, Y.W. Kim, T. Nishimura, W.S. Seo, High thermal conductivity of spark plasma sintered silicon carbide ceramics with yttria and scandia, Journal of the American Ceramic Society 100(4) (2017) 1290-1294.

[17] N.P. Padture, In situ-toughened silicon carbide, Journal of the American Ceramic Society 77(2) (1994) 519-523.

[18] Y.-H. Kim, Y.-W. Kim, K.-Y. Lim, S.-J. Lee, Mechanical and thermal properties of silicon carbide ceramics with yttria–scandia–magnesia, Journal of the European Ceramic Society 39(2-3) (2019) 144-149.

[19] K. Raju, D.-H. Yoon, Sintering additives for SiC based on the reactivity: a review, Ceramics International 42(16) (2016) 17947-17962.

[20] T. Yamamoto, H. Kitaura, Y. Kodera, T. Ishii, M. Ohyanagi, Z.A. Munir, Consolidation of nanostructured β-SiC by spark plasma sintering, Journal of the American ceramic Society 87(8) (2004) 1436-1441.

[21] P. Šajgalík, J. Sedláček, Z. Lenčéš, J. Dusza, H.-T. Lin, Additive-free hot-pressed silicon carbide ceramics—A material with exceptional mechanical properties, Journal of the European Ceramic Society 36(6) (2016) 1333-1341.

[22] S. Kultayeva, J.-H. Ha, R. Malik, Y.-W. Kim, K.J. Kim, Effects of porosity on electrical and thermal conductivities of porous SiC ceramics, Journal of the European Ceramic Society 40(4) (2020) 996-1004.

[23] D.R. Clarke, Materials selection guidelines for low thermal conductivity thermal barrier coatings, Surface and Coatings Technology 163 (2003) 67-74.

[24] Z.-Y. Deng, J.M. Ferreira, Y. Tanaka, Y. Isoda, Microstructure and thermal conductivity of porous ZrO2 ceramics, Acta materialia 55(11) (2007) 3663-3669.

[25] P. Klemens, M. Gell, Thermal conductivity of thermal barrier coatings, Materials Science and Engineering: A 245(2) (1998) 143-149.

[26] H. Zhan, Y. Nie, Y. Chen, J.M. Bell, Y. Gu, Thermal Transport in 3D Nanostructures, Advanced Functional Materials 30(8) (2020) 1903841.

[27] L. Sigl, Thermal conductivity of liquid phase sintered silicon carbide, Journal of the European Ceramic Society 23(7) (2003) 1115-1122.

[28] Y. Zhou, K. Hirao, K. Watari, Y. Yamauchi, S. Kanzaki, Thermal conductivity of silicon carbide densified with rare-earth oxide additives, Journal of the European Ceramic Society 24(2) (2004) 265-270.

[29] Y.-W. Kim, M. Mitomo, G.-D. Zhan, Mechanism of grain growth in liquid-phase-sintered β–SiC, Journal of materials research 14(11) (1999) 4291-4293.

[30] D. Hasselman, L.F. Johnson, Effective thermal conductivity of composites with interfacial thermal barrier resistance, Journal of composite materials 21(6) (1987) 508-515.

[31] L.L. Snead, T. Nozawa, Y. Katoh, T.-S. Byun, S. Kondo, D.A. Petti, Handbook of SiC properties for fuel performance modeling, Journal of nuclear materials 371(1-3) (2007) 329-377.

[32] L. Snead, S. Zinkle, D. White, Thermal conductivity degradation of ceramic materials due to low temperature, low dose neutron irradiation, Journal of nuclear materials 340(2-3) (2005) 187-202.

[33] L.L. Snead, Y. Katoh, S. Connery, Swelling of SiC at intermediate and high irradiation temperatures, Journal of nuclear materials 367 (2007) 677-684.

[34] W. Jiang, H. Wang, I. Kim, Y. Zhang, W.J. Weber, Amorphization of nanocrystalline 3C-SiC irradiated with Si+ ions, Journal of Materials Research 25(12) (2010) 2341-2348.

[35] X. Wang, H. Zhang, T. Baba, H. Jiang, C. Liu, Y. Guan, O. Elleuch, T. Kuech, D. Morgan, J.-C. Idrobo, Radiation-induced segregation in a ceramic, Nature Materials (2020) 1-7.

[36] C. Jiang, D. Morgan, I. Szlufarska, Structures and stabilities of small carbon interstitial clusters in cubic silicon carbide, Acta materialia 62 (2014) 162-172.

[37] K. Yueh, K.A. Terrani, Silicon carbide composite for light water reactor fuel assembly applications, Journal of Nuclear Materials 448(1-3) (2014) 380-388.

[38] S.J. Zinkle, K.A. Terrani, J.C. Gehin, L.J. Ott, L.L. Snead, Accident tolerant fuels for LWRs: A perspective, Journal of Nuclear Materials 448(1-3) (2014) 374-379.

[39] X. Dong, Y.C. Shin, Predictions of thermal conductivity and degradation of irradiated SiC/SiC composites by materials-genome-based multiscale modeling, Journal of Nuclear Materials 512 (2018) 268-275.

[40] V.S. Chauhan, M.F. Riyad, X. Du, C. Wei, B. Tyburska-Püschel, J.-C. Zhao, M. Khafizov, Thermal conductivity degradation and microstructural damage characterization in low-dose ion beam-irradiated 3C-SiC, Metallurgical and Materials Transactions E 4(2) (2017) 61-69.

[41] Y. Lee, H.C. No, J.I. Lee, Design optimization of multi-layer Silicon Carbide cladding for light water reactors, Nuclear engineering and design 311 (2017) 213-223.

Chapter 2 Literature Review

Part I Fabrication and microstructure of SiC ceramics

2.1 Crystal structure of SiC

Basic unit structure of SiC is a covalently bonded tetrahedron (88% covalent bond and 12% ionic bond), either in form of SiC_4 or CSi_4. Bond length between atom Si and nearest atom C is around 0.189 nm [1]. SiC possess a number of polytypes (>250) which are distinguished by stacking sequence of bilayer units composed of one layer of Si atoms and the other layer of C atoms [2]. A bilayer unit is denoted as A, B or C. Polytype of SiC is denoted based on its crystal structure and number of bilayer units in the direction of c-axis within a unit cell. Letter of C, H and R stand for cubic, hexagonal, and rhombohedral crystal respectively. Four main polytypes of SiC are shown in Figure 2. 1. According to Figure 2. 1, 3C-SiC is unique cubic crystal with 3 bilayer units which are stacked in sequence of ABC along [111] crystal direction. 6H-SiC is hexagonal crystal with 6 bilayers units which are stacked in sequence of ABCACB along [0001] crystal direction [3]. It is noted that 3C-SiC is generally called as β-SiC while all rest SiC polytypes are called as α-SiC [4].

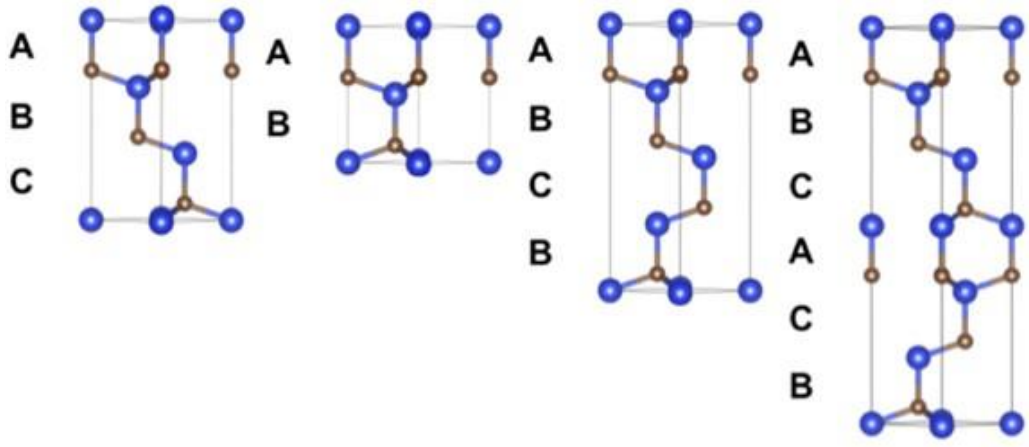

Figure 2. 1 Stacking sequence of main SiC polytypes: from left side to right side, they are called as cubic (3C-SiC), hexagonal (2H-SiC), hexagonal (4H-SiC) and hexagonal (6H-SiC). Large and small atoms stand for atom Si and atom C respectively. Pictures are taken from reference [3].

2.2 Sintering mechanism of SiC ceramics

The covalent nature of SiC crystal results in excellent properties (e.g. high thermal conductivity, excellent high temperature mechanical properties, good irradiation resistance, etc) and thus has been used in lots of fields (e.g. heat exchanger, nozzles, cladding materials, and so on) [5-10]. Sintering is the most common method to fabricate dense SiC ceramics, but it is very difficult to sinter dense SiC due to high content (88%) of covalent bonds and extremely low self-diffusion coefficient (~10^{-11} $cm^2 \cdot s^{-1}$ for C and ~10^{-13} $cm^2 \cdot s^{-1}$ for Si) [11]. Also, it is noted that driving force for ceramic densification is that ratio between grain boundary energy and surface energy of starting ceramic particle should be smaller than 2 [12]. However, it was found that grain boundary energy of SiC is so high that densification was practically restrained [4]. Even at high temperature, particle coarsening based on evaporation-condensation mechanism rather than densification took place due to high vapor pressure of SiC [4, 13]. Consequently, very high temperature (>2100 °C) and/or ultra-high pressure (~5 GPa) were required to fabricate dense SiC ceramics without sintering additive [1, 14, 15].

To fabricate dense SiC ceramics under moderate conditions, a number of sintering additives were developed and combined with conventional sintering techniques (e.g. pressureless sintering and hot pressing sintering) and some novel sintering techniques (e.g. spark plasma sintering and flash sintering) [1]. In part 2.2, sintering mechanism of SiC ceramics will be reviewed in terms of two common sintering mechanisms (liquid phase sintering and solid state sintering).

2.2.1 Solid state sintering

Solid state sintering takes place when green powder compact is densified in a solid state during whole sintering process. For solid state-sintered ceramics, there are several mechanisms related to densification and neck growth (also called as particle coarsening): lattice diffusion via point defects, dislocation and grain boundary, heterogeneous interface diffusion, surface diffusion and evaporation-condensation process [1]. Lattice diffusion and heterogeneous interface diffusion could result in reduced distance between particle centers and thus are necessary for densification while rest mechanisms make contribution to neck growth [1]. Solid state sintering additives have been

developed to promote densification of SiC ceramics in terms of increasing diffusion coefficient and/or driving force (smaller ratio between grain boundary energy and surface energy).

Prochazka et al. successfully fabricated dense SiC ceramics (relative density >96%) at 2100 °C using B and/or C [16]. It was found that single addition of B or C led to low relative density (57%-62%) and minimum content of boron in the mixture of B and C for complete densification should be higher than solubility limit of B in SiC. It was assumed that C reacted with silica in the surface of SiC particle and thus resulted in higher particle surface energy while B tended to segregate in grain boundaries of SiC and led to lower grain boundary energy [16, 17]. In other words, simultaneous addition of B and C decreases ratio of grain boundary energy to particle surface energy, resulting in larger driving force for densification. However, there are debates about role of boron in promoting densification of SiC. It was suggested that B could dissolve into SiC lattice and preferably replace Si site, resulting in more point defects (like C vacancy) and enhanced lattice diffusion [18, 19]. This assumption was somewhat supported by the experimental results of Stobierski et al. who studied densification and microstructure of solid state sintered SiC ceramic with constant carbon content and different boron contents [20]. It was found that density increased significantly with boron content when boron content was lower than 0.2 wt.% [20]. Such strong density dependence on the boron content (< 0.2 wt.%) implied that dissolution of B into SiC lattice was necessary for densification. In contrast, as boron content increased from 0.25 wt.% to 0.4 wt.%, relative density stabilized at around 97% [20]. Given that solubility limit of B into SiC is ~0.2 wt.% [4, 21], excessive B is expected to segregate in grain boundary and higher content of B should have increased density of sintered SiC ceramics if B segregation was dominant for densification.

Figure 2. 2(a) demonstrates typical microstructure of the SiC sintered with 3 wt.% C and 0.4 wt.% B. The SiC ceramic was mainly composed of elongated grains which generally were beneficial for obtaining high fracture toughness [20, 22]. Grain boundary of solid state sintered SiC with 0.5 wt.% B and 1 wt.% C was thoroughly detected via high-resolution transmission electron microscopy (HRETM), high-angle annular dark-field (HAADF) and electron energy loss spectroscopy (EELS) [23]. Figure 2. 2(b) shows HRTEM of the sintered SiC ceramics. It was found that although secondary

phase containing B and/or C was not found in grain boundary of SiC, EELS and HAADF confirmed segregation of B and C in grain boundaries and chemical width of segregation region was approximately 1 nm [23]. Presence of the B/C segregation could be explained by the high content of B and C.

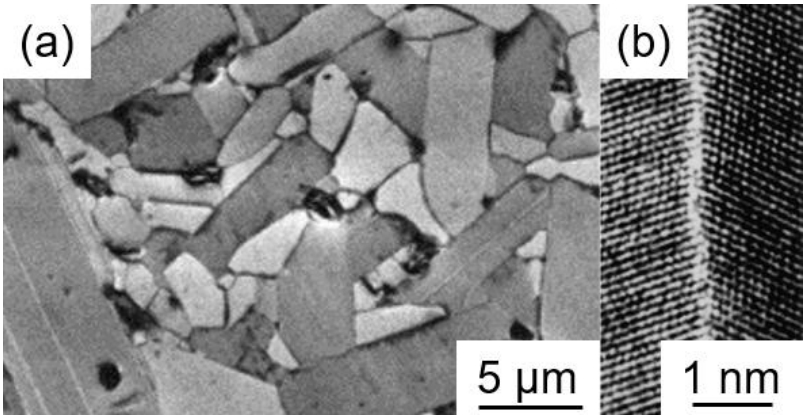

Figure 2. 2 Microstructure of solid state sintered SiC ceramics with B and C as sintering additives: (a) SEM micrograph of SiC with 3 wt.% carbon and 0.4 wt.% B [20]; (b) HRTEM image of SiC with 0.5 wt.% B and 1 wt.%C [23].

2.2.2 Liquid phase sintering

Liquid phase sintering (LPS) takes place when green powder/particle compact is densified in the presence of liquid phase. Liquid phase could come from single phase with low melting point, two phases with low eutectic temperature, or multiphase with low liquid formation temperature. Several key aspects should be satisfied for successful densification by liquid phase sintering: low contact angle and low dihedral angle, adequate liquid phase, high solubility of solid in the liquid and low solubility of liquid in the solid [24]. Compared with solid state sintering, liquid phase sintering has two advantages: firstly, lower sintering temperature is required for full density due to lower liquid formation temperature of sintering additives while sintering temperature for solid state sintering generally should be close to melting point of ceramics; secondly, microstructure with elongated grains and/or fine equiaxed grains is more easily to be obtained, which are beneficial for excellent comprehensive mechanical properties. Aside from those advantages, it is also noted that the high temperature mechanical properties, oxidation resistance and thermal conductivity of liquid phase

sintered ceramics could be worse than counterparts of solid state sintered ceramics due to intrinsically weak properties (e.g. low melting point and low thermal conductivity) of the secondary phase originating from the liquid phase sintering additives [25-27].

Liquid phase sintering mechanisms have been studied by several researchers [24, 28, 29]. Generally, liquid phase sintering process was divided the into 3 stages: First stage was referred as particle rearrangement. In this stage, liquid sintering additive is formed during heating process and spreads through particles. Particle will be rearranged under capillary force, which results in release of liquid into pores and significant densification. Densification in this stage is affected by several parameters: amount of liquid sintering additive content, sintering temperature, wetting angle, green density and so on. It was reported that when volume content of liquid sintering additive was sufficiently high (>35 vol.%), full density could be achieved without following stages [29].

Second stage was referred as solution-reprecipitation process, which is shown in Figure 2. 3. According to Figure 2. 3, mechanism a is referred as contact-flattening. Capillary force induced by the liquid between 2 particles results in larger compressive force in contact area. As a result, this area under larger compressive force preferably dissolves into liquid phase because of chemical potential gradient. The dissolved solid atoms diffuse through the liquid and reprecipitates onto regions away from contact area. This process is mainly responsible for densification due to positive role of capillary forces in reducing distance between particle centers. Mechanism b is called as dissolution of small grains and reprecipitation on large grains. This mechanism is responsible for grain growth and makes little contribution to densification except that the dissolution process promotes grain shape accommodation and thus increases packing density of solid. Mechanism c is called as solid-state bonding. Although particle surfaces are wetted by liquid phase, growth of inter grain contact is achieved by dissolution of convex areas in solid grains, diffusion through wetting liquid and then re-precipitation onto the contact areas (concave area). This mechanism is responsible for grain shape accommodation. In summary, three mechanisms in second stage together describe densification, grain growth and grain shape accommodation [29].

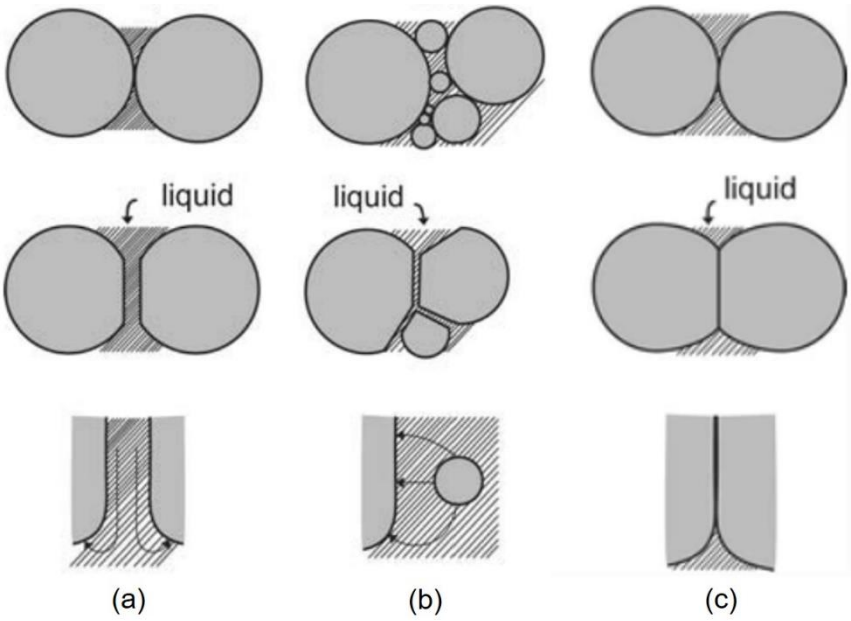

Figure 2. 3 Three mechanisms related to densification, grain growth and grain shape accommodation during solution-reprecipitation process of liquid phase sintering: (a) contact flattening, (b) dissolution of small grains, (c) solid state bonding. Pictures are taken from reference [24].

Third stage is referred as solid-state sintering. This stage is indicated by very slow densification due to much lower diffusivity in solid compared with that in liquid. Grain boundary diffusion is believed to be responsible for removal of residual closed pores [24].

Lange et al. fabricated fully dense SiC ceramics (relative density >99%) at 1950 °C under uniaxial pressure of 28 MPa with 2 vol.% Al_2O_3 as a sintering additive, verifying the effective role of Al_2O_3 in reducing sintering temperature [30]. There were other sintering additives (e.g. Al_2O_3-Y_2O_3, Al_2O_3-Y_2O_3-CaO, Al_2O_3-Y_2O_3-MgO, Y_2O_3-Sc_2O_3-MgO, etc.) for promoting densification of SiC ceramics at lower sintering temperature [25, 31-33]. Al_2O_3-Y_2O_3 is one typical sintering additive adopted for fabricating dense SiC ceramics due to its excellent wettability on SiC [34]. Figure 2. 4 shows the binary phase diagram of Al_2O_3-Y_2O_3. According to Figure 2. 4, when the molar ratio of Al_2O_3 and Y_2O_3 is chosen as 4:1, the eutectic temperature is approximately 1780 °C. At the eutectic composition, Al_2O_3 and Yttrium Aluminum Garnet ($Y_3Al_5O_{12}$, YAG) would generate when the liquid mixture of Al_2O_3-Y_2O_3 is cooled down to room temperature [34]. As the mixture is used as sintering additive to

densify SiC ceramics, the liquid formation temperature could be further reduced due to the SiO_2 on the surface of starting SiC powder. It was reported that the lowest eutectic temperature in the ternary system of Al_2O_3-Y_2O_3-SiO_2 was 1350 °C [35, 36]. It is also noted that SiC did not react with Al_2O_3-Y_2O_3 at low temperature (<1900 °C) [31, 37]. Presence of such small amount of silica in starting SiC powders was suggested to have negligible effects on the final composition of Al_2O_3-Y_2O_3 [37]. However, at high temperature (≥1900 °C), Al_2O_3 could react with SiC and lead to formation of gas products (like CO and SiO) which would retard release of liquid into pores [31, 38]. To minimize detrimental effects of reaction between Al_2O_3 and SiC, Mulla et al. adopted pressurized CO atmosphere (0.105 MPa) to prevent the reaction and fabricated dense SiC (relative density >98%) by pressureless sintering at 2050 °C with 10 wt.% Al_2O_3 as a sintering additive [38].

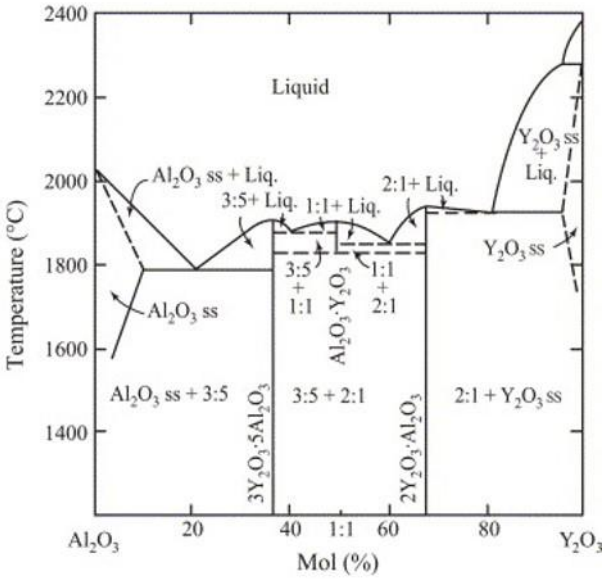

Figure 2. 4 Phase diagram of Al_2O_3-Y_2O_3 [34].

Given that inevitable weight loss during pressureless sintering of SiC ceramics with Al_2O_3 based sintering additive, non-oxide sintering additives (like Al-B-C and Al_4C_3-B_4C-C) have also been developed. It was found that highly dense SiC ceramics (relative density >95%) could be pressureless sintered at 1850 °C with assistance of Al_4C_3-B_4C-C, which was 200°C-300 °C lower than counterparts required for solid state sintered SiC ceramics with mixture of B and C as a sintering additive [39]. The lower sintering temperature was attributed to formation of liquid phase $Al_8B_4C_7$ at 1800 °C and absence of reaction between SiC and sintering additive [40]. Except exploring new

sintering additives to reduce sintering temperature, adopting external force (e.g. uniaxial pressure and hot-isostatic pressure) is another effective approach to promoting densification of liquid phase sintered SiC ceramics because external force could promote particle arrangement and enhance chemical potential of atoms under the contact surface which is beneficial for mass transport during solution reprecipitation process [41].

2.3 Spark plasma sintering

As mentioned in part 2.2, to achieve densification at less severe conditions, sintering additive has been combined with different sintering techniques (e.g. pressureless sintering, gas pressure sintering, hot pressing sintering and hot-isostatic pressing sintering) and some novel sintering techniques (e.g. spark plasma sintering and flash sintering). Among these sintering techniques, the advanced spark plasma sintering (SPS) is most interesting due to its unique advantages (e.g. shorter sintering time, higher heating/cooling rate and lower sintering temperature) over conventional sintering techniques [1]. In part 2.3, only SPS will be reviewed and details of other sintering techniques can be found in the reference [1].

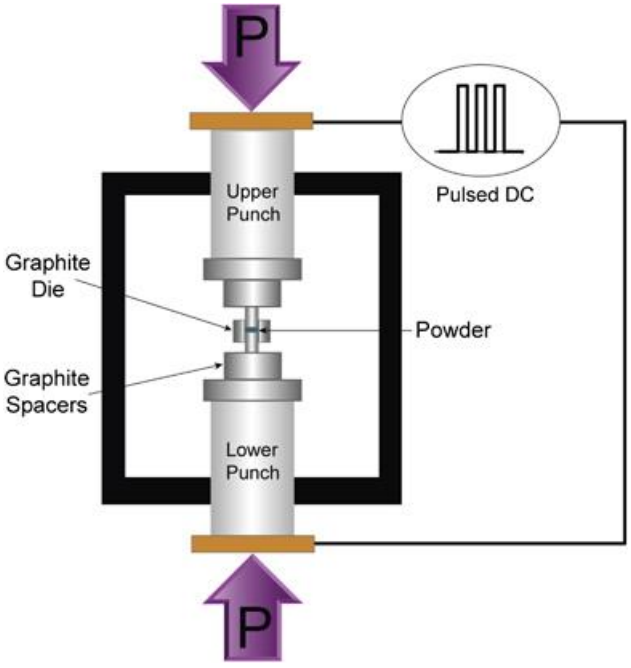

Figure 2. 5 A schematic diagram of spark plasma sintering apparatus with pulsed direct current [42].

A typical SPS apparatus is illustrated in Figure 2. 5 [42]. Starting powders or green powder compacts are loaded into a graphite die and subject to uniaxial pressure provided by top and bottom punches. Normally a hole inside the graphite die will be made for more accurate temperature measurement by the pyrometer. During SPS process, a large pulsed direct current (typical 30-60 ms pulse current of ~1000 A) will be used to generate Joule heating via going through the green powder compacts and/or graphite dies depending on electrical conductivity of the powder compacts. For instance, it was reported that only 100 mA current went through the insulting Al_2O_3 powders at 1000 °C, which is negligible compared with total current of around 1000 A [43]. For non-electrically conductive powder compact, both Joule heating and heat conduction from the graphite die to the powder compact are responsible for sintering process.

Sakkaki et al. simulated the distribution of temperature and electric current during the spark plasma sintering process of electrically conductive ZrB_2 and non-conductive Al_2O_3 [44]. It was found that the temperature distribution was more uniform for Al_2O_3 compared with counterparts of ZrB_2, resulting in more homogenous properties in the sintered specimens. The electric current concentrated in the graphite die close to Al_2O_3 whereas a more uniform current distribution was presented in the ZrB_2 [44].

The adoption of pulsed direct current could enhance mass transfer via several mechanism: electromigration [45, 46], increasing concentration and/or mobility of point defects [47-50], electric field [43] and spark plasma formation [51]. Lan et al. studied the microstructural evolution and thermoelectric properties of PbTe compounds fabricated with and without direct pulse current [49]. It was found that the PbTe compound sintered with direct pulse current has much larger grain size and higher electrical conductivity compared with counterparts of the hot pressing sintered compounds without assistance of direct current regardless of same heating profile. The higher electrical conductivity was attributed to the larger grain size and increased carrier concentrations originating from enhanced formation of Pb-rich precipitates and the vacancy (V_{Pb}) defects in the presence of pulse direct current [49]. For non-electrically conductive powders, the electric field can enhance densification and change microstructure although current almost does not go through powder

compacts in SPS process. Shinoda et al. investigated influence of electric field on texture formation of mullite in SiC sintered with Al_2O_3-SiO_2 additive [52]. It was found that c-axis of the mullite in SiC ceramics sintered without introducing electric field were vertical to the compressive axis at 1600-1900 °C while c-axis of the mullite in SiC ceramics sintered with electric field were parallel to the compressive axis (also the electric field direction) at high temperature (1800-1900 °C) [52]. The preferred polarization induced by the electric field during mullite nucleation process was thought to be responsible for the special texture at the high temperature [52].

It is noted that presence of plasma is still under debate [53, 54]. It was believed that spark discharge could be generated in the gaps of powder particles upon the application of pulsed direct current, which would result in local high temperature that promoted melting and evaporation of particle surface [55, 56]. Cleaning of particle surface might enhance diffusion and densification. However, other researchers claimed that neither spark discharge nor plasma was present in the spark plasma sintering process of electrically conductive powders (e.g. Al, Mg, Zn, and TiAl) and non-electrically conductive powders (e.g. Al_2O_3 and NaCl) [53, 57]. Recently, Zhang et al. confirmed that spark plasma could be generated during the spark plasma sintering process of the electrically conductive TiB_2 powders which was uniformly spread between graphite punches [54]. Besides, Chaim declared that generation of spark plasma in the sintering process of non-electrically conductive powder was dependent on particle size, adopted voltage and the dielectric strength [58]. Marder et al. fabricated nanoscale YAG using spark plasma sintering and suggested that the material jets between the spherical nano-particles were induced by the spark plasma and could promote densification [59]. Regardless of the ambiguity about plasma presence, it was found that the so-called spark and plasma formation had negligible effects on densification rate of metallic powders while the mechanical pressure adopted in SPS could accelerate materials transport by orders of magnitude [60].

In addition to the pulsed direct current, high heating rate (100-1000 °C/min) is another special feature of SPS compared with conventional hot pressing sintering (HPS) technique. The high heating rate of SPS results in quick pass of low-temperature regions at which surface diffusion takes place and

leads to particle coarsening [61]. Larger particle means lower surface energy and lower driving force for densification. In other words, high heating rate could keep larger driving force for densification to higher temperature and increase densification rate.

Yamamoto fabricated dense SiC ceramics (relative density of 98%) without any sintering additive by SPS at the lowest sintering temperature of 1700 °C under a uniaxial pressure of 40 MPa [62]. It is stressed that starting SiC powders with crystalline size of 5-20 nm were fabricated by high-energy ball-milling method and only had peaks at 2θ (Bragg angle) of 36°, 60° and 72° in the X-ray diffraction (XRD) spectrum. It was found that as-fabricated disordered SiC could transform into ordered SiC at sintering temperature between 1600-1700 °C and the disorder to order transformation was responsible for achieving densification without obvious grain growth. Sintering temperature for spark plasma sintered SiC ceramics could be further reduced with assistance of sintering additive. Lee at al. reported that sintering temperature for obtaining fully dense SiC ceramics could be reduced to 1450 °C with 10 wt.% Al_2SiC_4 as a sintering additive under uniaxial pressure of 120 MPa [63]. Densification of the sintered SiC ceramics was neither due to liquid phase sintering since lowest eutectic temperature in Al_2O_3-SiO_2-Al_4O_4C system was 1595 °C nor enhanced lattice diffusion resulting from doping of Al into SiC lattice. They attributed densification of the sintered SiC ceramics at such low temperature to grain boundary diffusion of segregated Al and suggested that the grain boundary diffusion could be further improved by electrical current [63].

2.4 Microstructure development of liquid phase sintered SiC ceramics

Liquid phase sintered SiC ceramics have attracted more attention because of not only its lower sintering temperature but also higher feasibility of tailoring microstructure and properties compared with counterparts of solid state sintered SiC ceramics. For liquid phase sintered SiC ceramics, liquid sintering additive is generally present as secondary phase for the volume fraction of liquid sintering additive (>3 vol.%) is higher than its solubility limit in SiC grains. The sintering additive distributing in grain boundaries is referred as intergranular film while the sintering additive distributing in triple junctions is referred as triple junction phase. In part 2.4, grain growth, phase transformation, and

distribution of sintering additive will be reviewed as they are crucial for microstructure development of liquid phase sintered SiC ceramics.

2.4.1 Grain growth

As mentioned in section 2.2.2, grain growth in liquid phase sintering process is mainly achieved by dissolution of small grains into liquid phase sintering additive and reprecipitation onto large grains. The solution-reprecipitation process in liquid phase sintered SiC ceramics was firstly confirmed by Sigl and Kleebe [64]. They characterized microstructure of liquid phase sintered SiC with YAG as a sintering additive by scanning transmission electron microscopy-Energy dispersive X-ray spectroscopy (STEM-EDS) and scanning electron microscopy (SEM).

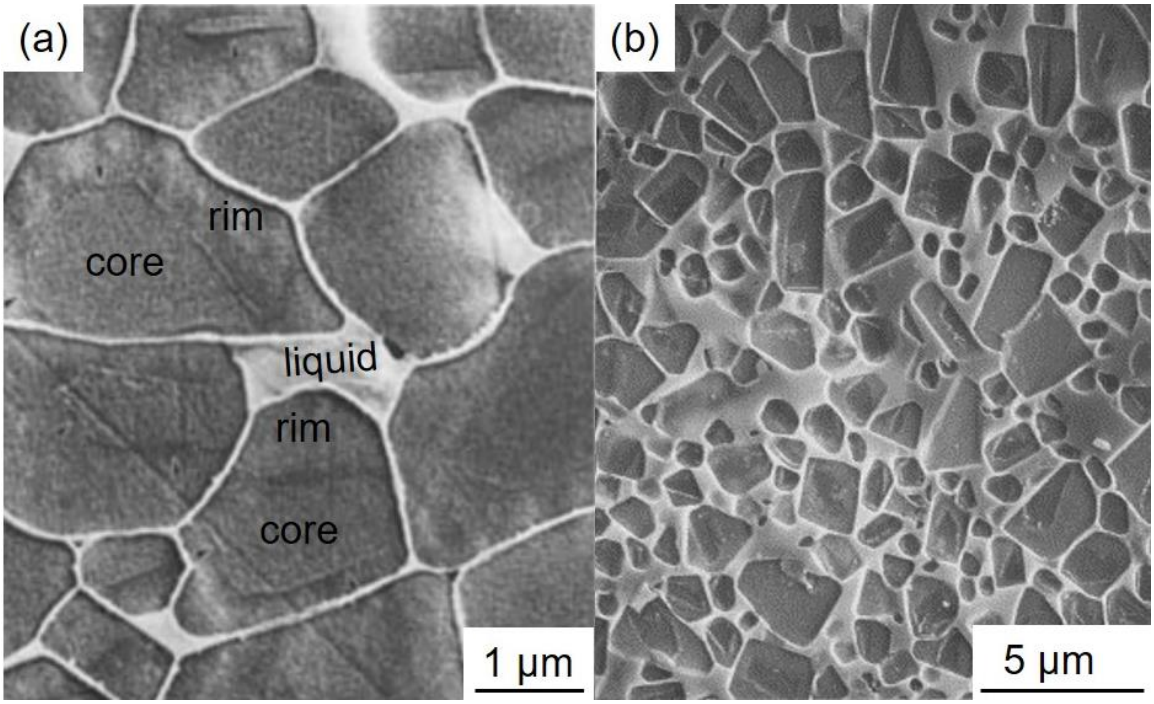

Figure 2. 6 SEM images of the plasma etched microstructures of liquid phase sintered SiC ceramics with YAG as a sintering additive: (a) 10 vol.% YAG and sintering temperature of 1950 °C were used [64]; (b) 20 vol.% YAG, heat treatment temperature of 2000 °C and holding time of 1 h were used [65].

Figure 2. 6 shows SEM images of the sintered SiC ceramics after being plasma etched for 75 min. According to Figure 2. 6(a), core-rim structure can be clearly seen in a single grain and the contrast difference between core and rim region was attributed to high sensitivity of plasma etching rate on chemical composition. STEM-EDS analysis on the core and rim regions indicated that Si, C and

small amount of impurities (e.g. Al and O) from liquid sintering additives were present in rim region but only Si and C were detected in core regions [64]. Similar core-rim structures were also observed by Ye et al. who adopted same type of starting powders (α-SiC and YAG) [65]. They found that grain growth rate was independent of sintering additive content and thus speculated that it was the interface-reaction process rather than the process of atom diffusion in liquid that controlled grain growth via solution-reprecipitation process [65]. In contrast, Kim et al. studied grain growth mechanism of sintered SiC with β-SiC and oxynitride glass as starting materials and concluded that it was atom diffusion in the liquid that controlled grain growth based on the fact that grain growth of sintered SiC ceramics was inhibited at higher content of sintering additive [66]. It should be noted that core-rim structure may not be observed due to absence of plasma etching or chemical homogenization during long heat treatment [67]. But based on shape of SiC grains embedded in large pockets of liquid phase sintering additives, solution-reprecipitation process could also be inferred [68].

2.4.2 Phase transformation

Knippenberg and Inomata et al. determined thermal stability of most common SiC polytypes via investigating growth of SiC crystals fabricated by 2 methods (i.e. the molten metal method and the sublimation and recrystallization method) at different temperatures and results are shown in Figure 2. 7 [69-71]. The top and bottom pictures in Figure 2. 7 were obtained by different researchers and the bottom picture demonstrated the composition of long-period/stable SiC at given temperatures [69, 70]. It was found that polytypes of SiC crystal were dependent on growth rate and synthesis temperature [72]. Specifically, when growth rate of SiC was very high, β-SiC was initially formed at temperature range from 1000 °C to 2700 °C, after certain time β-SiC transformed into α-SiC. If growth rate of SiC was low, α-SiC was directly formed at high temperature [72].

According to Figure 2. 7, 3C-SiC is regarded as stable phase between 1400-1600 °C. 2H-SiC keeps stable between 1300-1600 °C while some α-SiC (e.g. 4H-SiC, 6H-SiC and 15R-SiC) can co-exist at temperature region of 1600-2600 °C. Co-existence of these α-SiC was mainly attributed to small differences in internal energy of the polytypes [71]. In addition, it was reported that several common

impurities (e.g. Al, B and N) may affect thermal stability of SiC polytypes. For example, Al and B were found to stabilize 4H-SiC while N tended to stabilize 3C-SiC [71, 72]. In summary, phase transformation may take place depending on sintering conditions and type of starting powders.

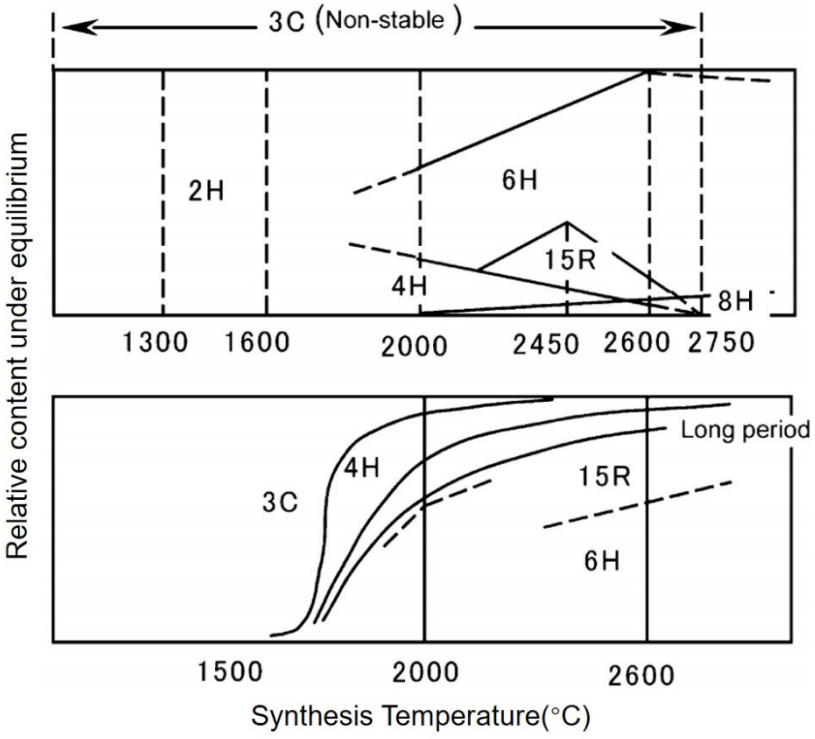

Figure 2. 7 Relative content of SiC polytypes under equilibrium as a function of synthesis temperature [69-71].

Heuer et al. investigated phase transformation from β-SiC to α-SiC in solid state sintered SiC ceramics with mixture of B and C as a sintering additive. It was concluded that β-SiC to α-SiC transformation was achieved in 2 stages: first stage was rapid growth of the composite grains composed of α-SiC sandwiched between envelopes of recrystallized β-SiC. The core of α-SiC in composite grains may nucleate at stacking fault of β-SiC. The recrystallization of β-SiC was achieved by forming a coherent interface with α-SiC for interfacial energy of that interface between $\{111\}_{\beta\text{-SiC}}$ and $\{0001\}_{\alpha\text{-SiC}}$ was several orders of magnitudes lower than counterparts of other random β/α-SiC interface [73]. Rapid growth of the composite grains into β-SiC matrix with fine grains was also driven by reduction in number of random β/α-SiC interface per unit volume. Second and final stage involved elimination of β-SiC envelope, which was achieved by nucleation and growth of α-lamella at twin boundary and stacking fault of β-SiC [74, 75]. Hence, it can be concluded that grain growth of

elongated grains is promoted by phase transformation. In addition, Lodhe et al. adopted the stress exponents (n) developed in the Bernard-Granger and Guizard model to study the underlying mechanism of the transformation from β-SiC to α-SiC during the spark plasma sintering process of as-pyrolyzed SiC and SiC whisker reinforced SiC composites without additional sintering additives [76]. It was reported that the phase transformation at 1600 °C was determined by the diffusion process due to small n (n<2) while the dislocation glide/climb dominated the transformation at 1700–1800 °C due to large n (2<n<5) [76].

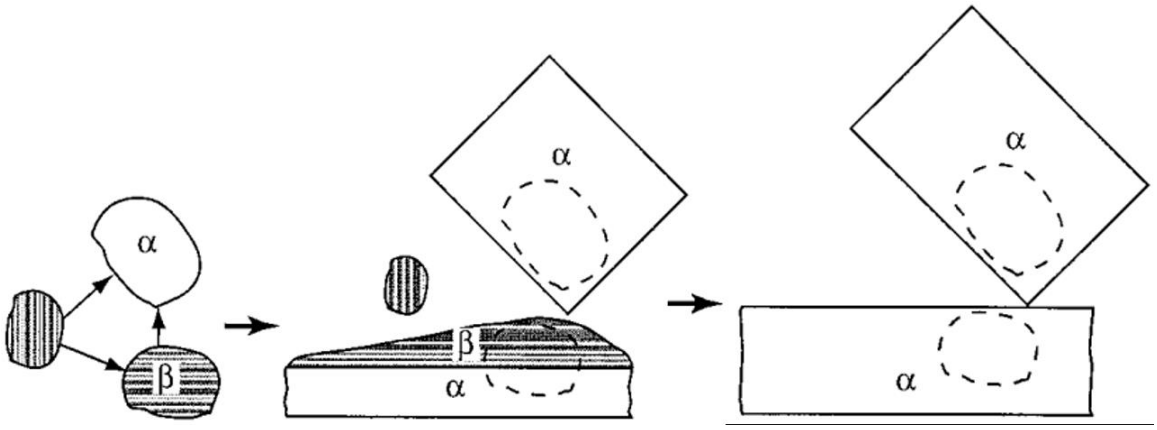

Figure 2. 8 Schematic demonstration of phase transformation model in LPS-SiC ceramics, picture is taken from [77].

Xu et al. studied phase transformation in liquid phase sintered SiC ceramics with 10 wt.% mixture of Al_2O_3 and Y_2O_3 as a sintering additive [67]. Figure 2. 8 shows the phase transformation model in liquid phase sintered SiC [77]. It was proposed that α-SiC firstly nucleated at stacking faults and/or coherent twin boundary in β-SiC and thus formed composite grains consisting of β-SiC cap and α-SiC. As coarsening progressed, smaller grains including untransformed β-SiC and composite grains dissolved into liquid sintering additives and reprecipitated onto larger composite SiC grains. It should be noted that Si and C tended to reprecipitate as α-SiC at elevated temperatures (>1800 °C) due to its higher thermal stability compared with that of β-SiC. Similar to phase transformation in solid-state sintered SiC ceramics, growth rate along length direction of composite grains was much higher compared with counterpart along thickness direction because of anisotropic interfacial energy. Elimination of β-SiC cap was achieved by much slow solid state diffusion [67]. Aside from the

conventional solution-reprecipitation mechanism, it was recently reported that oxidation of β-SiC could induce the phase transformation from β-SiC to α-SiC at extremely low temperature of 600 °C [78]. It has been verified that oxidation of β-SiC led to the formation of SiO_2. Furthermore, the thermal residual stress on the SiC/SiO_2 interface was generated due to their difference in the coefficient of thermal expansion. The driving force for the transformation from β-SiC to α-SiC was attributed to the smaller thermal residual stress of the α-SiC/SiO_2 interface compared with counterpart of the β-SiC/SiO_2 interface [78].

Further study showed that small addition of α-SiC into β-SiC powders did not have effects on transformation rate from β-SiC to α-SiC but could reduce aspect ratio of elongated grains because coarsening of α-SiC seed via solution-precipitation process was carried out in an equiaxed manner to near-equilibrium shapes [77]. Also, it was reported that grain growth and/or phase transformation of liquid phase sintered SiC ceramics were retarded in N_2 atmosphere despite of starting powder type, which was attributed to doping of N into the liquid. Such doping led to higher melting point and higher viscosity of liquid phase and thus slowed solution-reprecipitation process [79, 80]. It is noted that phase transformation from β-SiC to α-SiC is an effective approach to form interlock microstructure with improved fracture toughness [33, 81].

2.4.3 Sintering additive distribution

As mentioned above, sintering additive could distribute in grain boundaries (called as intergranular film) or triple junctions (called as triple junction phase). Triple junction phase is always present while absence/presence of intergranular film is determined by heat treatment conditions and sintering additive composition.

Roosen et al. studied microstructure of sintered SiC ceramics with 10 vol.% Al_2O_3-Y_2O_3 as a sintering additive at different sintering temperatures [82]. It was found that intergranular film was found in the SiC ceramic sintered at 1800 °C while intergranular film was absent when sintering temperature was increased to 1950 °C. Absence of intergranular film was attributed to reduced impurity content in

liquid phase and accelerated decomposition reaction between SiC and SiO_2 at higher sintering temperature [82].

Kim et al. investigated microstructure and high-temperature strength of liquid phase sintered SiC ceramics with 10 vol.% different sintering additive types consisting of AlN and Re_2O_3 (Re = Sc, Lu, Yb, Er and Y) at same molar ratio of 2:3 and same sintering temperature 2000 °C [5]. It was demonstrated that intergranular amorphous film was only present in the sintered SiC ceramic with AlN and Y_2O_3 as a sintering additive. There were not intergranular films in other sintered SiC ceramics, indicating sintering additive composition has important influence on the presence/absence intergranular film. Also, it should be noted that clean SiC-SiC grain boundary (absence of intergranular film) does not always result in more excellent high temperature strength. For instance, flexural strength at the measurement temperature higher than 1400 °C of the SiC ceramic sintered with AlN-Yb_2O_3 which possessed clean SiC-SiC grain boundaries were around 12%-20% lower than counterparts of the SiC ceramic sintered with AlN-Y_2O_3 which possessed intergranular amorphous film [5]. In addition, the intergranular film was suggested to reduce thermal/electrical conductivity of liquid phase sintered SiC ceramics due to its intrinsically low thermal/electrical conductivity [31, 83-86].

Given that possible effects of intergranular film on thermal conductivity, it is necessary to choose appropriate characterization technique. Currently, HRTEM is commonly used to identify presence/absence of intergranular film between 2 grain boundaries. To obtain HRTEM image containing several grain boundaries, grain boundary plane must be aligned with electron beam of TEM, which is practically very difficult for grain boundary plane is generally very thin (few nanometer). Besides, it was reported that highly curved grain boundaries may be impossible to be parallel to electron beam even if the TEM sample is extremely thin [87]. Alternatively, STEM-EDS can be used to detect presence/absence of element segregation in grain boundaries and qualitatively determine composition and width of intergranular film [87].

2.5 Summary of part I

In part I of chapter 2, sintering of dense SiC ceramics are reviewed in terms of sintering mechanisms and the advanced sintering technique. More importantly, microstructures development of liquid phase sintered SiC ceramics are reviewed from 3 aspects: grain growth, phase transformation and sintering additive distribution. Related information could be summarized as follows:

(1) Liquid phase sintering is more effective than solid state sintering in promoting densification of SiC due to much higher diffusion rate in liquid than that in solid. SPS could further improve densification because of high heating rate and possibly adoption of pulsed direct current.

(2) For SiC ceramics, phase transformation is driven by the thermal stability of SiC polytype and grain growth is driven by reduction of grain boundary energy. During liquid phase sintering process, both phase transformation and grain growth are achieved by solution-reprecipitation process and the rate-controlling step is dependent on the fabrication conditions (e.g. temperature, sintering additive composition and sintering atmosphere).

(3) For liquid phase sintered SiC ceramics, sintering additive always distributes in the triple junctions while distribution of sintering additive in grain boundaries is dependent on fabrication conditions (e.g. temperature and sintering additive composition). The sintering additive distributing in grain boundaries is suggested to reduce thermal/electrical conductivity due to its intrinsically low thermal/electrical conductivity.

Part II: Thermal conductivity of SiC ceramics

2.6 Heat conduction mechanism

Thermal conductivity is one basic property that determines material's ability to transfer heat. According to Fourier's law shown in equation 2.1, thermal conductivity was defined as the result of heat flux density divided by temperature gradient [88].

$$k = -\frac{Q}{\nabla T} \tag{2.1}$$

Where k is thermal conductivity (W/(m•K)), Q is heat flux density (heat flow per seconds per unit cross section vertical to direction of heat flow, (W/m^2)) and ∇T is temperature gradient along heat flow direction (K/m).

Given that very limited number of free mobile electrons are present in non-metals, phonon (a quasiparticle describing lattice vibration) is believed to dominate heat conduction. Debye has derived thermal conductivity of non-metals using simple kinetic theory about heat conduction in gas, which is shown in equation 2.2 [88].

$$k = \frac{1}{3} C_v * v^2 * \tau \tag{2.2}$$

where C_v, v, and τ are specific heat capacity per unit volume (J•K^{-1}•m^{-3}), phonon group velocity (m/s) and relaxation time (s).

Generally infinite relaxation time is not possible due to presence of different scattering sources in lattice (e.g. other phonons, lattice defects and electrons). Thermal conductivity dominated by phonons (called as lattice thermal conductivity, k_L) could be obtained by a simplified Callaway model in which theory of relaxation time approximation was adopted to solve Phonon Boltzmann equation (PBE). In that model, several assumptions were made: a. all scattering process could be described by corresponding relaxation time; b. an average velocity ($\boldsymbol{v}$) of acoustic phonons with different polarizations was adopted for all phonons despite of phonon branches and polarization because optical phonons possesses much lower velocity compared with counterparts of acoustic phonons; c.

phonon dispersion relation is united ($\omega = v * q$) [61]. Equation 2.3 gives lattice thermal conductivity calculated by the simplified Callaway model [88].

$$k_L = \frac{k_B}{2\pi^2 v} * (\frac{k_B}{\hbar})^3 * T^3 * \int_0^{\theta_D/T} \tau_q(x) * \frac{x^4 e^x}{(e^x-1)^2} dx \quad (2.3)$$

Where k_B is Boltzmann constant, v is the average velocity for all phonons, $\hbar$ is reduced Planck constant, θ_D is Debye temperature of SiC, ω is angular frequency of a phonon, q is wave number of a phonon, T is absolute temperature, x equals to $\hbar\omega/(k_B T)$ and τ_q stands for total relaxation time of a phonon with wave number of q.

As long as relaxation time for each scattering process is provided, total relaxation time could be calculated based on Matthiessen's rule, as shown in equation 2.4 [88, 90].

$$\tau_q^{-1} = \sum_i \tau_i^{-1} \quad (2.4)$$

Where τ_q^{-1} stands for reciprocal of total relaxation time, and τ_i^{-1} stands for reciprocal of relaxation time of a type of phonon scattering process (e.g. τ_D^{-1} representing phonon-point defect scattering, τ_{GB}^{-1} representing phonon-grain boundary scattering, τ_U^{-1} representing Umklapp process and τ_N^{-1} for representing normal process). Although only normal process is a conservative momentum process, it was proven that Matthiessen's rule was still reasonable for calculating lattice thermal conductivity of most crystals which contained significant amount of impurity (e.g. point defect, isotopes, grain boundary and so on) and thus relaxation time for normal process is much longer than counterparts of other scattering processes [88, 89].

According to the simplified Callaway model, relaxation time are determined by phonon frequency and temperature. Dependence of reciprocal of relaxation time for each scattering process on phonon frequency can be summarized as: $\tau_D^{-1} \sim \omega^4$, $\tau_U^{-1} \sim \omega^2$, $\tau_N^{-1} \sim \omega^2$ and τ_{GB}^{-1} is independent of phonon frequency [89].

2.7 Thermal conductivity of SiC ceramics

As mentioned in Chapter 1, thermal conductivity of SiC ceramics ranged from 32 W/(m•K) to 490 W/(m•K) [36, 91-93]. Such huge variation of thermal conductivity is caused by diverse microstructure.

In this part, effects of sintering additives and microstructure including grain size and point defects on thermal conductivity of SiC ceramics will be reviewed.

2.7.1 Grain size effects

Generally thermal conductivity of single crystal is higher than counterpart of polycrystalline ceramic due to additional phonon-grain boundary scattering in polycrystalline ceramics. It was reported that thermal conductivity of a single crystal 6H-SiC was as high as 490 W/(m•K) at 300 K while thermal conductivity of polycrystalline SiC ceramics at 300 K was generally below 270 W/(m•K) [91, 92]. Collins et al. has studied effects of grain size on thermal conductivity of CVD-SiC and indicated that as grain size increased from 6.8 μm to 17.2 μm, thermal conductivity at 273.15 K increased from 90 W/(m•K) to 175 W/(m•K) [94]. Besides, it was found that at low temperature (<223 K), thermal conductivity of CVD-SiC increased with measurement temperature, which was mainly caused by specific heat dependence on temperature (known as $C_V \sim T^3$). With increasing temperature, more phonons with higher frequency make contribution to heat conduction and thus Umklapp process (one type of phonon-phonon scattering process) becomes more and more significant. Consequently, at temperature close to or higher than Debye temperature (in the range of 860-1200 K) of SiC ceramics, Umklapp process dominates heat conduction while other phonon scattering process could be ignored [94, 95].

Although above mentioned simplified Callaway model (equation 2.3) could theoretically describe different phonon scattering process dominating heat conduction, it does not have any analytical solution and is hardly correlated with microstructure. To correlate grain size with thermal conductivity of polycrystalline ceramic, Yang proposed a one-dimensional model in which grain and grain boundary subjected to same heat flux are arranged serially [96]. Figure 2. 9(a) shows heat conduction process in the one-dimensional model. According to Figure 2. 9(a), there is a temperature discontinuity in the grain boundary because of phonon-grain boundary scattering. Such temperature discontinuity in grain boundary could be described by grain boundary thermal resistance (also called as Kapitza resistance). Based on Fourier's law, equation 2.5 was given to incorporate grain boundary thermal resistance into thermal conductivity of polycrystalline ceramic [96].

$$k = \frac{k_0}{1+k_0 * R/d} \tag{2.5}$$

Where k and k_0 are thermal conductivity of polycrystalline ceramic and bulk single crystal, respectively. R and d are grain boundary thermal resistance and grain size of polycrystalline ceramic, respectively.

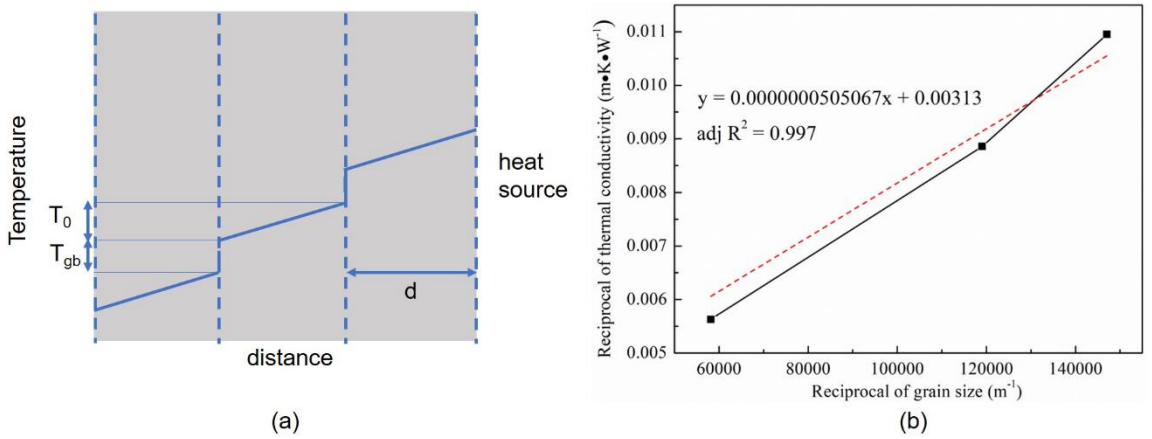

Figure 2. 9 Diagram of a temperature profile along a polycrystalline sample subjected to heat flow [96]; (b) reciprocal of thermal conductivity of CVD-SiC as a function of reciprocal of grain size [94], red dotted line is a fitted curve and black solid line connects experimental data.

In Yang's model, thermal conductivity of a grain in polycrystalline ceramic was assumed to be the same as that of bulk single crystal. Such assumption may not be reasonable at low temperature for dominant phonons controlling heat conduction at low temperature possess long wavelength which is possibly close to grain size [97]. Frequency of dominant phonons could be estimated using equation $\omega = 4.25 * k_B * T/\hbar$ and sound of velocity of SiC could be estimated to be around 8268 m/s [98-100]. One can easily obtain that the wavelength of dominant phonon in SiC ceramic ($v = \lambda * \omega/2\pi$) at 10 K is around 9.2 nm and decreases with increasing measurement temperature until its shortest wavelength corresponding to Debye frequency. Therefore, it is reasonable to use Yang's model to describe phonon-grain boundary scattering process of polycrystalline SiC ceramics with sub-micro/micro grains at temperature above 300 K.

By fitting reported experimental data of CVD-SiC with equation 2.5 [94], grain boundary thermal resistance of the CVD-SiC was approximately 5.05 X 10^{-8} W^{-1}•m^2•K, as shown in Figure 2. 9(b). The

derived grain boundary thermal resistance value is around 2 orders of magnitude higher than counterpart (~4.88 X 10^{-10} W^{-1}•m^2•K) calculated by molecular dynamics (MD) simulation [101]. Such significant discrepancy between those 2 values was possibly attributed to 2 reasons: firstly, grain growth achieved by increasing deposition temperature in CVD-SiC may change intragranular thermal conductivity due to variation of defects inside grains during heat treatment process; secondly, there may be impurity segregation in grain boundary which would affect grain boundary thermal resistance but a perfect grain boundary without any impurity was constructed via inserting array of edge dislocations or simple symmetry and shift method during calculation process of MD simulation [101, 102]. For example, it was found that 1 monolayer segregation of dopant in SiC grain boundary could result in 1 order of magnitude increase of grain boundary thermal resistance compared with counterpart of undoped SiC grain boundary [102].

2.7.2 Point defects effects

Point defects are zero-dimensional defects in a crystal lattice and could occur in several forms: vacancy, interstitial, substitutional atom and antisite defect [75]. Presence of point defect in lattice could strongly scatter phonons with high frequency based on following mechanism: (1) mass difference between host atom and solute atom; (2) binding force difference between normal linkage and linkage around point defects; and (3) elastic strain field around point defects [76]. As mentioned above, the reciprocal of relaxation time (τ_D^{-1}) corresponding to phonon-point defect scattering process is dependent on phonon frequency [61]. Moreover, τ_D^{-1} is determined by scattering cross section (Γ) of point defects that could be depicted via equation 2.6 [98].

$$\Gamma = \sum_i \Gamma_i = \sum_i x_i[(\frac{\Delta M_i}{M})^2 + 2(\frac{\Delta G_i}{G} - 6.4 * \gamma * \frac{\Delta \delta_i}{\delta})^2] \quad (2.6)$$

Where x_i is fraction of the point defect with mass M_i and radius δ_i, M and δ are mass and radius of substituted atom/ion in pure host lattice respectively. G_i corresponds to average stiffness of bonds from the defect atom to its adjacent host atoms while G is average stiffness of bonds from the substituted atom to its adjacent atoms in a perfect lattice. γ is Grüneisen parameter which reflects anharmonicity of lattice. Three items in equation 2.6 stands for above mentioned three types of phonon-point defect scattering process, respectively [98].

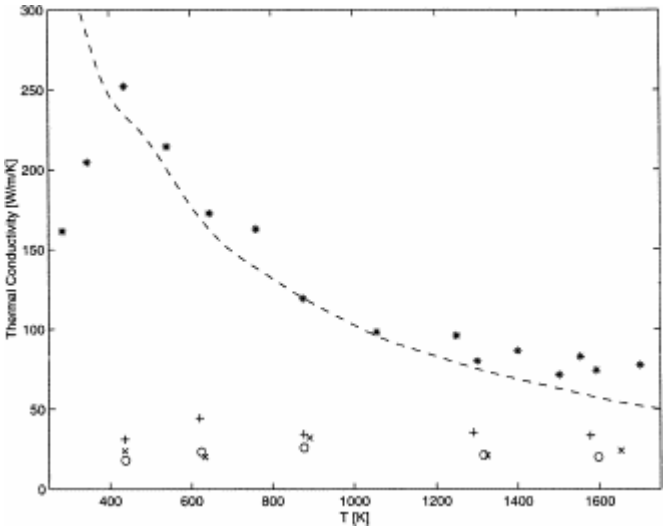

Figure 2. 10 Thermal conductivity of SiC as a function of measurement temperature: dash line stands for experimental values of perfect SiC crystals, stars correspond to calculated results for perfect SiC crystal, pluses stand for SiC crystal with 0.5% carbon vacancy, crosses correspond to SiC crystal with 0.5% carbon antisite, circles stand for SiC crystal with 0.5% Si vacancy. All calculated results are obtained by MD [105].

Thermal conductivity reduction due to point defects in SiC lattice has been verified by MD simulation, as shown in Figure 2. 10 [105]. According to Figure 2. 10, thermal conductivity at 436 K could reduce from 252 W/(m•K) for a perfect SiC crystal to 19.8 W/(m•K) for SiC crystal with 0.5% Si vacancy, implying strong phonon-point defect scattering. Also, thermal conductivity of SiC crystal with 0.5% point defects almost does not show dependence on measurement temperatures. In contrast, both calculated and experimental thermal conductivity of perfect SiC crystal decrease significantly with measurement temperature at temperature above 400 K, which was attributed to the dominant role of Umklapp process in controlling heat conduction [105].

As reviewed in part I, liquid phase sintering additives (like Al_2O_3-based sintering additive and rare-earth oxide based sintering additive) have been widely developed to promote densification of SiC ceramics. In liquid phase sintered SiC ceramics with Al_2O_3 based sintering additive, it was assumed that Al_2O_3 would dope into SiC lattice via typical solution-reprecipitation mechanism during liquid phase sintering process, resulting in formation of point defects inside SiC lattice, i.e. Si vacancy and substitutional atoms of Al and O, as shown in defect equation 2.7 [103, 106]. The assumption related

to Al_2O_3 doping into SiC lattice has been verified by XRD and STEM-EDS analysis [64, 107]. Besides, SiO_2 originating from surface of raw SiC powder could also dissolve into SiC lattice and create point defects, as shown in equation 2.8 [106].

$$Al_2O_3 \xrightarrow{SiC} 2Al'_{Si} + 3O_C^{\bullet\bullet} + V_{Si}'''' \quad (2.7)$$

$$SiO_2 \xrightarrow{SiC} Si_{Si} + 2O_C^{\bullet\bullet} + V_{Si}'''' \quad (2.8)$$

Where Al'_{Si} stands for Si site in SiC lattice is replaced by Al and charge of this substitutional Al is +1, Si_{Si} means Si from dissolved SiO_2 inside SiC lattice occupies Si site in SiC lattice, $O_C^{\bullet\bullet}$ means that C site in SiC lattice is replaced by O and charge of this substitutional O is -2, and V_{Si}'''' means that Si vacancy with charge of +4 is formed due to electroneutrality inside SiC lattice doped with SiO_2 or Al_2O_3.

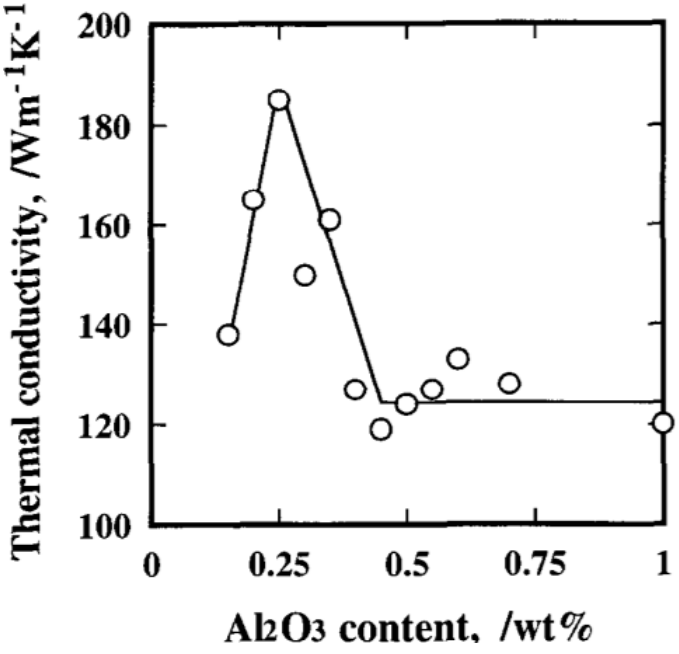

Figure 2. 11 Thermal conductivity of liquid phase sintered SiC ceramics as a function of Al_2O_3 content. After reference [107].

Kinoshita et al. fabricated SiC ceramics with 0.15-1.0 wt.% Al_2O_3 as a sintering additive and reported that thermal conductivity increased with Al_2O_3 content as the content was between 0.15-0.25 wt.% and achieved its maximum values at the content of 0.25 wt.%, as shown in Figure 2. 11 [107]. Enhancement of thermal conductivity due to increasing Al_2O_3 content within that range (0.15-0.25

wt.%) was attributed to decreased porosity at higher Al_2O_3 content [107]. Maximum thermal conductivity (185 W/(m•K)) of the sintered SiC ceramic with Al_2O_3 as a sintering additive is about 38% of counterpart (490 W/(m•K)) of single crystal 6H-SiC, which is mainly attributed to strong phonon scattering by additional point defects (e.g. lattice defects of Al_{Si}, V_{Si} and O_C) formed during liquid phase sintering process.

According to Figure 2. 11, as Al_2O_3 content was above 0.25 wt.%, thermal conductivity decreased with increasing Al_2O_3 content up to 0.4 wt.% while relative density almost kept constant at around 99.9%. Meanwhile, it was found that both impurity concentration (e.g. lattice defects of Al_{Si} and O_C) inside SiC grains and concentration of Al and O segregated in grain boundary increased with Al_2O_3 content within range of 0.25-0.4 wt.%. The reduction of thermal conductivity with increasing Al_2O_3 content was mainly attributed to increasing grain boundary segregation although no convincing explanation was given for neglecting contribution of increasing impurity concentration inside SiC grains. As Al_2O_3 content is higher than 0.45 wt.%, thermal conductivity fluctuated at approximately 120 W/(m•K), which was correlated with constant grain boundary concentration of Al and O [107].

2.7.3 Sintering additive effects

Adoption of liquid sintering additive not only promotes densification of SiC at less harsh sintering conditions but also results in various microstructures which have significant effects on thermal conductivity of sintered SiC ceramics. Up to now, relatively high content (>3 vol.%) of liquid phase sintering additive was used for densifying SiC ceramics in most reported studies and thus resulted in formation of secondary phase distributing in triple junctions and/or grain boundaries. To evaluate thermal conductivity of sintered SiC ceramics with non-negligible amount of secondary phase, it is necessary to review thermal conductivity of composites.

2.7.3.1 Effects of sintering additive content

Lots of theoretical models have been developed to describe thermal conductivity of two-phase composites, which are distinguished by microstructure characteristics of the composites [108, 109]. Typically, series model and parallel model describe thermal conductivity of composites consisting of slabs in serial and parallel configuration relative to heat flow directions respectively [108]. Maxwell

model represents thermal conductivity of composites consisting of continuous matrix and discrete secondary phase (also called as dispersion), as shown in Figure 2. 12(a). It is noted that local thermal interactions between adjacent discrete secondary phase was ignored and thermal contact between matrix and discrete secondary phase was assumed to be perfect in Maxwell model. Hence, Maxwell model is more suitable for composites with low volume fraction of discrete secondary phase [109, 110]. Bruggeman model incorporated thermal interactions between heterogeneous phases by assuming that sphere matrix and secondary phase were symmetrically embedded into an unknown effective medium with thermal conductivity of the composite, as shown in Figure 2. 12(b). Consequently, Bruggeman model is more appropriate for composites with high volume fraction of secondary phase but it is mentioned that thermal interaction is maximized in Bruggeman model for interactions between matrix and its neighboring secondary phase was assumed to be the same as counterpart between matrix and other non-neighboring secondary phase [111-113].

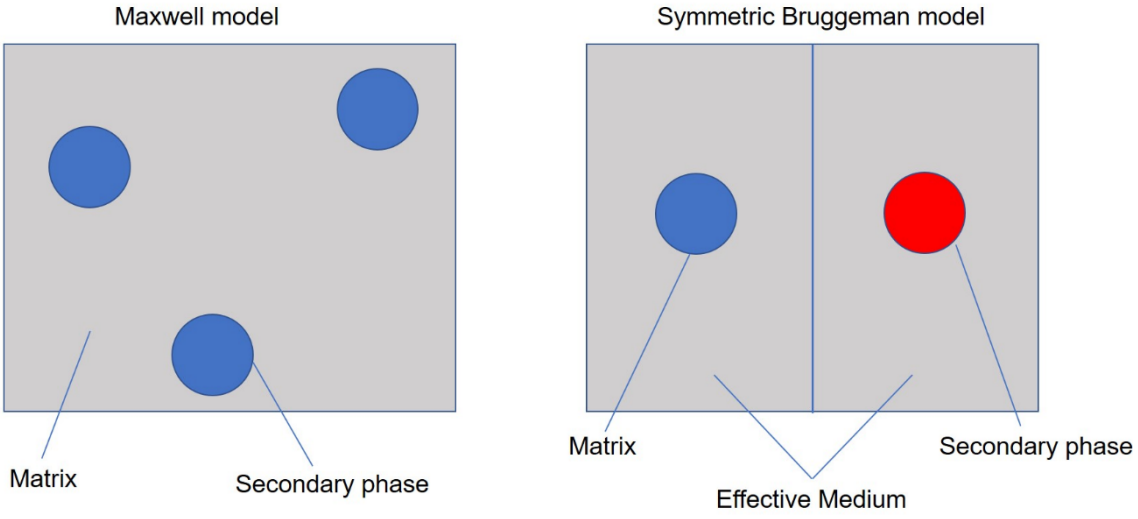

Figure 2. 12 Schematic diagrams of different models for thermal conductivity of composites: (a) Maxwell model assumes lack of interactions between temperature fields of adjacent secondary phase [109], (b) Symmetric Bruggeman model in which sphere matrix and secondary phase were symmetrically embedded and interact with each other via the unknown effective medium with thermal conductivity of the composite [112].

Sigl et al. studied thermal conductivity of liquid phase sintered SiC composites with 3-30 vol.% mixture of $Y_3Al_5O_{12}$ and AlN (molar ratio $Y_3Al_5O_{12}$: AlN = 4:1) as a sintering additive. XRD and SEM

results together showed that the sintered SiC composites were composed of discrete SiC doped with AlN and continuous $Y_3Al_5O_{12}$ [114, 115]. Figure 2. 13 shows thermal conductivity of the sintered SiC composites as a function of volume fraction of SiC. According to Figure 2. 13, higher volume fraction of SiC results in higher thermal conductivity due to higher thermal conductivity of SiC compared with that of $Y_3Al_5O_{12}$ [115]. Different models have also been employed to fit experimental data (solid circles), as shown in Figure 2. 13. Series model and parallel models give upper and lower limit of thermal conductivity of sintered SiC composites respectively. According to Figure 2. 13, thermal conductivity calculated by Maxwell model (as depicted in the dash-dotted line) are higher than counterparts of experimental values within all studied volume fraction of SiC. That discrepancy was attributed to ignorance of amorphous grain boundary film surrounding SiC grains. The Maxwell model was thus modified to accommodate real microstructure of sintered SiC composites and matched well with experimental data, as shown in the solid line in Figure 2. 13. The results showed that presence of grain boundary film was responsible for around 20% reduction of thermal conductivity [114].

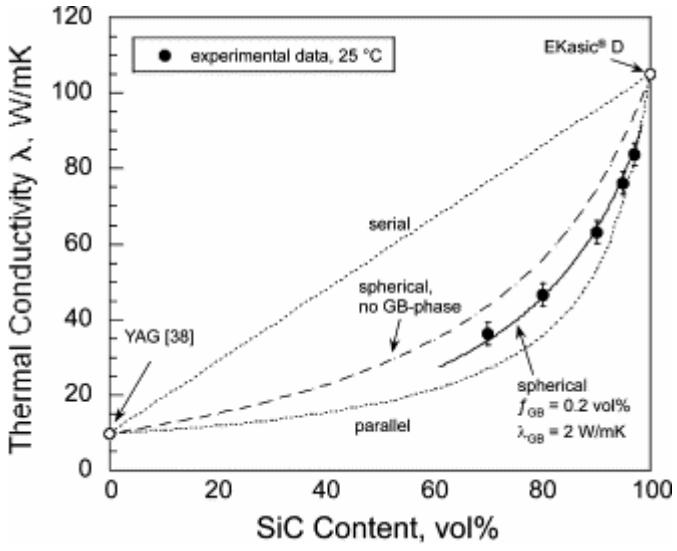

Figure 2. 13 Thermal conductivity of liquid phase sintered SiC composites as a function of volume fraction of SiC (solid circles). $Y_3Al_5O_{12}$ (YAG) is used as a sintering additive, 2 dashed lines were plotted according to series and parallel model respectively, dash-dotted line was plotted based on Maxwell model without considering grain boundary phase, solid line was plotted by modified Maxwell model incorporating grain boundary phase with thermal conductivity of 2 W/(m•K) and volume fraction of 0.2 vol.%, picture is taken from reference [114].

2.7.3.2 Effects of interfacial thermal resistance

As mentioned above, a perfect thermal contact between 2 phases was assumed in Maxwell model but interfacial thermal resistance may be significant in real composites especially when 2 phases possess extremely different physical properties. To include effects of interfacial thermal resistance on thermal conductivity, Hasselman and Johnson proposed a modified Maxwell model, as shown in equation 2.9 [116].

$$k_e = k_1 \frac{[2(\frac{k_2}{k_1}-\frac{k_2}{ah_c}-1)v_2+\frac{k_2}{k_1}+\frac{2k_2}{ah_c}+2]}{[(1-\frac{k_2}{k_1}+\frac{k_2}{ah_c})v_2+\frac{k_2}{k_1}+\frac{2k_2}{ah_c}+2]} \quad (2.9)$$

Where k_e, k_1, k_2, v_2 and a stand for effective thermal conductivity of composites, thermal conductivity of continuous phase and discrete phase, volume fraction and radius of discrete phase respectively while h_c is thermal boundary conductance (reciprocal of thermal boundary resistance).

Interfacial thermal resistance consists of 2 parts: one part is referred as thermal contact resistance and the other part is described as thermal boundary resistance [109]. Thermal contact resistance is caused by poor mechanical/chemical bonding or cracks resulting from mismatch of thermal expansion coefficient [117]. Thermal boundary resistance is caused by mismatch of acoustic impedance according to Acoustic Mismatch Model (AMM) or mismatch of phonon density state according to Diffusion Mismatch Model (DMM) [118]. For those 2 models, two materials separated by an interface are assumed to be isotropic Debye solids, which means only acoustic phonons have been considered. In AMM models, phonons that are considered as plane waves propagates through materials which are regarded as continua and incidents on an interface considered as a plane. Incident of phonons on an interface complies with Snell's law and transmission probability is determined by mismatch between acoustic impedance (product of mass density and phonon velocity) of 2 materials and incident angle. Moreover, both elastic and inelastic scattering of phonon at an interface are ignored. Bases on these assumptions, equation 2.10-2.13 were proposed to calculate thermal boundary conductance (reciprocal of thermal boundary resistance) [118, 119].

$$h_c = \frac{1}{4} * v_1 * C_{\rho 1} * \rho_1 * \Gamma_1 \quad (2.10)$$

$$\Gamma_1 = \int_0^{\theta c} \alpha_1 * cos\theta * sin\theta d\theta = \frac{1}{2} * \alpha_1 * (sin\theta_c)^2 \quad (2.11)$$

$$\alpha_1 = \frac{4Z_1 * Z_2}{(Z_1 + Z_2)^2} \quad (2.12)$$

$$sin\theta_c = \frac{v_1}{v_2} \quad (2.13)$$

Where phonons were assumed to incident from material 1 with lower sound velocity compared with counterpart of material 2, h_c, $C_{\rho 1}$, v_1, and ρ_1 are thermal boundary conductance (reciprocal of thermal boundary resistance), specific heat, averaged sound velocity and density of material 1 respectively. Γ_1 stands for averaged transmission probability of phonons from material 1 to material 2. Z_1 and Z_2 are acoustic impedances ($Z = \rho * v$) of material 1 and material 2 separated by an interface respectively.

In contrast, in DMM models, all phonons incident on an interface are diffusely scattered and the transmission probability is determined by mismatch of phonon density of state between 2 materials. Based on this assumption, averaged transmission probability (Γ_1) in DMM model could be calculated via equation 2.14-2.15 [118].

$$\Gamma_1 = \int_0^{\pi/2} \alpha_1 * cos\theta * sin\theta d\theta = \frac{1}{2}\alpha_1 \quad (2.14)$$

$$\alpha_1 = \frac{{v_2}^{-2}}{{v_1}^{-2} + {v_2}^{-2}} \quad (2.15)$$

Where v_1 and v_2 are averaged sound velocities of material 1 and 2 respectively.

Dong et al. found that even though thermal conductivities of SiC and BeO were all higher than 330 W/(m•K), thermal conductivity of sintered SiC ceramic (grain size of ~5.6 μm) using BeO as a sintering additive was only 270 W/(m•K), implying the presence of thermal boundary resistance between SiC and BeO [91, 120]. The thermal boundary resistance could be predicted by nonequilibrium molecular dynamics (NEMD) and incorporated into a homogenized materials genome model for calculating thermal conductivity of SiC ceramics with BeO as a sintering additive. It was found that predicted thermal conductivity by the genome model was very close to experimental values of SiC ceramics with BeO, which verifies important role of thermal boundary resistance [120].

2.7.3.3 Effects of sintering additive type

Zhou et al. studied thermal conductivity of liquid phase sintered SiC ceramics with different types but same content of sintering additive (mixture of Al_2O_3-Y_2O_3 versus mixture of Y_2O_3-La_2O_3) [106]. Results showed that as Y_2O_3-La_2O_3 was chosen as a sintering additive, thermal conductivity of sintered SiC ceramics was higher than 167 W/(m•K). As Al_2O_3-Y_2O_3 was selected as sintering additive, thermal conductivity was lower than 71 W/(m•K). High thermal conductivity of SiC ceramics with Y_2O_3-La_2O_3 was attributed to the positive role of Y_2O_3-La_2O_3 in attracting oxygen dissolved into SiC lattice [106]. The assumption was confirmed by comparison between lattice oxygen of the sintered SiC ceramic with Y_2O_3-La_2O_3 and acid washed SiC powder. It was found that lattice oxygen (1500 ppm) of the sintered SiC ceramic was much lower compared with counterpart of acid washed SiC powders (5600 ppm). In contrast, lattice oxygen of the sintered SiC ceramic with Al_2O_3-Y_2O_3 possessed higher lattice oxygen (6200 ppm) than that of acid-washed SiC powders (5600 ppm). Hence, it was believed that doping of Al_2O_3 into SiC lattice resulted in lower thermal conductivity of SiC ceramic sintered with Al_2O_3-Y_2O_3. Besides, it was reported that phase transformation from β-SiC to α-SiC was suppressed as Y_2O_3-La_2O_3 was used as a sintering additive, which might have a positive role in increasing thermal conductivity although no convincing data was provided [106].

Table 2. 1 Microstructural characteristics of liquid phase sintered SiC ceramics with 2 vol.% Y_2O_3 based rare-earth oxide as a sintering additive.

Specimens	Sintering additive	Lattice oxygen (ppm)	Grain size (μm)	Thermal conductivity (W/(m•K))
SY1	Y_2O_3	N/A	6	188.6
SY2	Y_2O_3	2080	4	178.2
SYSm	Y_2O_3-Sm_2O_3	1860	3.6	198.2
SYGd	Y_2O_3-Gd_2O_3	2840	4.1	176.9
SYLu	Y_2O_3-Lu_2O_3	2000	4.4	181.1

Notes: Sintering additive content was fixed at 2 vol.% for all samples. Holding time, sintering temperature and atmosphere are 3 h, 2000 °C and N_2 respectively. Data related to specimen SY2 is after reference [121] and rest data is after reference [122].

Jang et al. studied thermal conductivity of pressureless-sintered SiC ceramics with 2 vol.% different types of mixture of Y_2O_3-RE_2O_3 (RE= Sm, Gd, Lu) as a sintering additives [122]. Microstructural characteristics and thermal conductivity of those samples are shown in Table 2. 1. According to Table 2. 1, thermal conductivity increases with decreasing lattice oxygen. For example, as lattice oxygen increases from 1860 ppm for sample SYSm to 2840 ppm for sample SYGd, thermal conductivity decreases from 198.2 W/(m•K) for sample SYSm to 176.9 W/(m•K) for sample SYGd. However, thermal conductivity does not seem to be influenced by grain size. Specifically, sample SYSm possess highest thermal conductivity of 198.2 W/(m•K) but smallest grain size of 3.6 μm, implying lattice oxygen is more critical than grain size in determining thermal conductivity. Given that lattice purification takes place during liquid phase sintering process, it was suggested that the mixture of Y_2O_3-Sm_2O_3 played a more effective role in reducing lattice oxygen in the SiC ceramic and thus resulted in higher thermal conductivity than counterparts of SiC ceramics with other sintering additives [122]. In summary, sintering additive can also affect thermal conductivity of SiC ceramics via changing concentration of lattice defects in SiC matrix.

2.8 Summary of part II

In part II of chapter 2, fundamental of heat conduction is reviewed. Microstructure and sintering additive effects on thermal conductivity of SiC ceramics are also reviewed, which could be summarized as follows:

(1) Larger grain size generally results in higher thermal conductivity due to reduced phonon-grain boundary scattering. In contrast, grain boundary segregation could enhance phonon-grain boundary scattering and thus reduce thermal conductivity.

(2) Point defects could effectively reduce thermal conductivity, which is attributed to the mass difference between host atom and solute atom, elastic strain field around point defects and the binding force difference between normal linkage and linkage around point defects.

(3) Thermal conductivity of SiC ceramics could be influenced by sintering additives, which could be explained by the intrinsically low thermal conductivity of sintering additive, the additional phonon-interface scattering and the change in lattice defects concentration in SiC.

Part III: Effects of irradiation on SiC ceramics

SiC has been regarded as one of the most promising candidates to replace current Zr alloy as cladding materials for nuclear reactors due to good radiation resistance, exceptional high-temperature mechanical property, high thermal conductivity, and excellent oxidation resistance to air and steam [6, 7, 123]. When SiC is used as cladding material and exposed to neutron irradiation environment, irradiation induced defects/defect clusters would lead to severe damage to microstructure and serious thermal conductivity degradation, which is an important issue for safety operation of nuclear reactors. In this part, irradiation effects on microstructure and thermal conductivity of SiC will be reviewed.

2.9 Irradiation types

Although similar irradiation conditions (neutron flux and energy spectrum) can be provided in special test reactors and applied to investigate suitable materials for nuclear reactors, limitation of test reactors, too long irradiation time and high activation of neutron-irradiated materials severely hindered meaningful and comprehensive study of irradiation damage on materials [124]. Alternatively, ion irradiation (e.g. proton, He ion and heavy ion) was developed to simulate effects of neutron irradiation on material microstructure and properties from 1960s [125]. Compared with neutron irradiation, high current ions can be generated by an ion accelerator using target materials with same mass as the ions and irradiation time could be greatly reduced due to high damage rate [124]. Also, activation of ion-irradiated materials is much weaker compared with that of neutron-irradiated materials [124]. Among those ions, although heavy ions have higher damage rate over counterparts of light ions and neutrons, heavy ions with modest energy (few MeV) have a much shallower damage profile than that of light ions with similar energy. For example, highest damage level in SiC ceramics irradiated by 4.5 MeV Si ion located at about 1.8 μm below surface [126]. In contrast, highest damage level in SiC ceramics irradiated by proton with smaller energy of 1.6 MeV was about 33 μm below surface. Moreover, a constant damage level was present from surface to around 25 μm below surface of proton irradiated SiC [127]. Hence, it is more feasible to adopt proton irradiation for carrying out comprehensive study on microstructure evolution and property degradation of SiC ceramics in terms of penetration depth and damage profile. In addition, it has been verified that the

evolution of microstructure and properties of stainless steels irradiated by proton at low damage level (< 10 displacements per atom, dpa) is very similar to counterparts under neutron irradiation in nuclear reactors [124].

2.10 Effects of irradiation on microstructure

High energy particles (e.g. neutron, proton and electron) collide with an atom in a lattice which consequently obtains massive kinetic energy and displaces from its original lattice site. That atom is called as primary knock-on atom (PKA). Subsequently, PKA collides with other surrounding atoms in a lattice, resulting in formation of many knock-on atoms. That process is called as displacement cascade. Those knock-on atoms stopped as interstitials, and simultaneously resulted in formation of vacancies [128]. Some radiation-induced defects could annihilate by recombination of interstitials with neighboring vacancies during irradiation process. Other defects or defect clusters that have not annihilated during irradiation process could generate complex agglomeration, such as dislocations loop, vacancy loop and lattice voids, which might lead to swelling and variation of material property [128]. In addition, both interstitial and vacancy could migrate towards sinks (e.g. surface, grain boundary and dislocations), resulting in possible formation of secondary phase and irradiation-induced segregation/depletion [128].

2.10.1 Dependence of lattice defects on irradiation conditions

Lattice defects generated during irradiation process are highly related to damage level and irradiation temperature. During irradiation process, the irradiation induced interstitials could firstly form clusters with small size (<1 nm). Such defect clusters appear as dark spots in bright field images and are thus called as black spot defects [129]. When damage level was increased, some defect clusters developed into the disk-shaped dislocation loops with the diameter between a few nanometres to a few tens of nanometres [130]. Depending on whether a fault in the stacking sequence of atomic plane has been introduced or not, the dislocation loop was named as the Frank faulted and unfaulted dislocation loop respectively [130]. The Frank faulted dislocation loops are parallel to the (111) crystal plane of cubic SiC and can result in extra streaks in the electron diffraction pattern. In contrast, the

unfaulted dislocation loop are parallel to the (110) crystal plane of cubic SiC and does not cause any stacking faults [129].

At low irradiation temperature (< 800 °C), black spot defects (i.e. interstitial clusters) and/or small dislocation loop were uniformly dispersed in the CVD-SiC irradiated by neutron and Si^{2+} [129]. Higher irradiation temperature and higher damage level led to coarsening of defect clusters and higher fraction of small unfaulted dislocation loop [129]. The absence of Frank faulted defects at relative low temperature was suggested to be caused by the stoichiometric nature of Frank loops and high migration energy (1.53 eV) of Si interstitials [129, 131, 132]. Furthermore, defect microstructure generated by different irradiation types (neutron versus Si^{2+} irradiation) at low temperature was very similar despite that ion irradiation had higher damage rate than that of neutron irradiation [129].

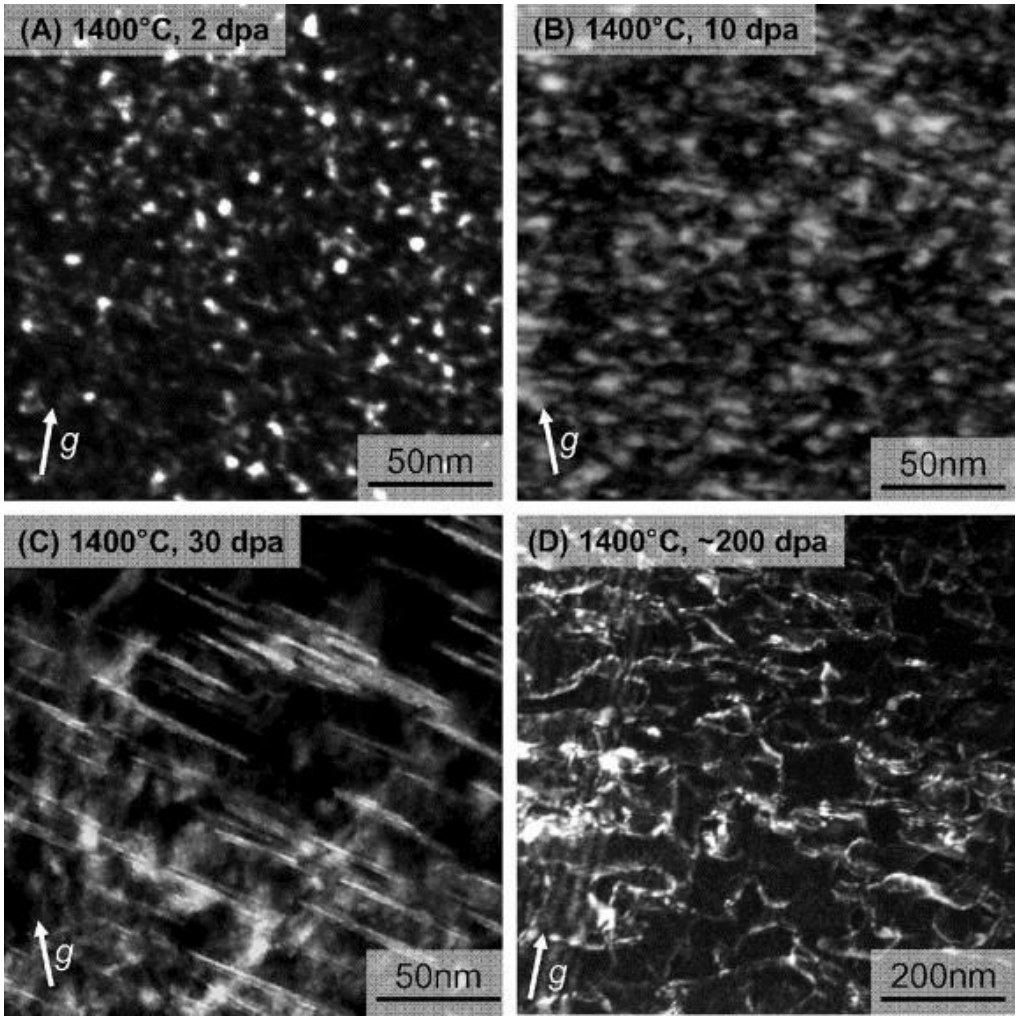

Figure 2. 14 Microstructure of Si^{2+} irradiated CVD-SiC at 1400 °C as a function of damage level. Electron beam direction ~[011], Burgers vector in parallel to $[01\bar{2}]$. Picture is taken from reference [129].

At high irradiation temperature (> 1000 °C), microstructure of Si^{2+} irradiated CVD-SiC remarkedly changed with increasing damage level, as shown in Figure 2. 14 [129]. Figure 2. 14 is the dark field images of irradiated SiC. According to Figure 2. 14, as damage level was 2 dpa, black spot defects and small dislocation loop were dominant in Si^{2+} irradiated CVD-SiC ceramic [129]. When damage level was increased to 10 dpa, Frank faulted loops were the main feature even though black spot defects and small non-faulted loops were still present. As damage level was 30 dpa, black spot defects and small dislocation loop completely transformed into the Frank faulted loop. As damage level was higher than 200 dpa, the Frank faulted loop developed into dislocation network [129]. Similar to the case at low irradiation temperature (< 800 °C), increasing irradiation temperature could

promote growth of defect clusters [129]. The Frank faulted loops formed by interstitials were observed in neutron irradiated CVD-SiC at irradiation temperature ranging from 1130 °C to 1460 °C [133]. It was found that growth rate of Frank loops at 1130 °C was lower than tenth of counterpart at 1460 °C, which was attributed to high sink strength resulting from lots of invisible cavities at 1130 °C. Decrease of loop density (numbers of loops per unit volume) with increasing irradiation temperature was possibly caused by coalescence of neighboring loops [133].

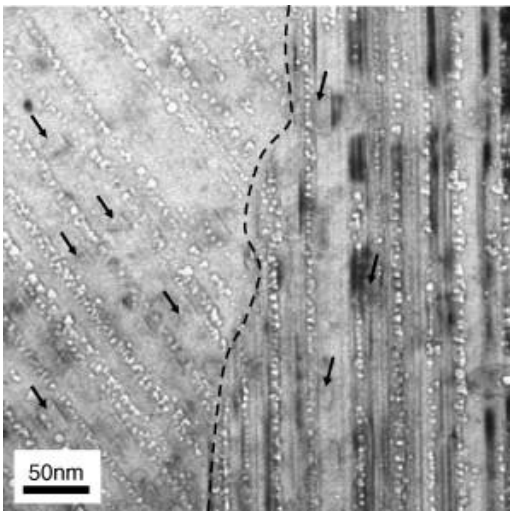

Figure 2. 15 TEM images of β-SiC ceramic irradiated by neutron with damage level of 5.8 dpa at 1460 °C. Electron beam is parallel to [110] for left grain. Arrows stands for invisible defect clusters between the faulted planes. A grain boundary is marked with dotted line. Picture is taken from reference [133].

In addition, cavities were observed in both neutron and Si^{2+} irradiated CVD-SiC ceramics at high irradiation temperature (>1000 °C) and high damage level of 10 dpa [129, 133]. Generally, size and density of cavities increased with increasing irradiation temperature and damage level. Majority of cavities were spherical below irradiation temperature of 1300 °C while most cavities are triangular with faceted side parallel to crystal planes of {111} at 1460 °C [133]. Moreover, preferentially nucleation of cavities in stacking faults were observed by TEM, as shown in Figure 2. 15. It can be clearly seen from Figure 2. 15 that density of cavities between faulted plane is much smaller than counterpart in stacking fault plane. Although it is difficult to observe cavities along the grain boundary, it was believed that grain boundary was another site for cavity formation [95, 129, 133].

2.10.2 Dependence of swelling on irradiation conditions

Swelling is very common in irradiated materials (e.g. alloy, metals, and ceramic) and characteristic of dimensional change. It is both practically and theoretically important to figure out underlying mechanism of swelling in SiC ceramics.

At temperature below 150 °C, swelling of neutron/ion irradiated SiC increased with damage level until occurrence of amorphization [95]. Swelling prior to amorphization was believed to be caused by differential strain between contraction of immobile vacancy and expansion of single interstitial or interstitial clusters [134]. Amorphization was favored in terms of greatly inhibiting increase in elastic energy resulting from accumulation of irradiation induced defects or defect clusters [135, 136].

At temperature ranging from 250 °C to 1000 °C, swelling demonstrated unique dependence on irradiation temperature and damage level, as shown in Figure 2. 16 [95]. Firstly, swelling at constant irradiation temperature increased with damage level until reaching saturated values. Secondly, saturated value was inversely proportional to irradiation temperature, which was caused by enhanced annihilation and/or coalescence of irradiation induced Frenkel defects due to higher mobility of interstitial at higher temperatures [137].

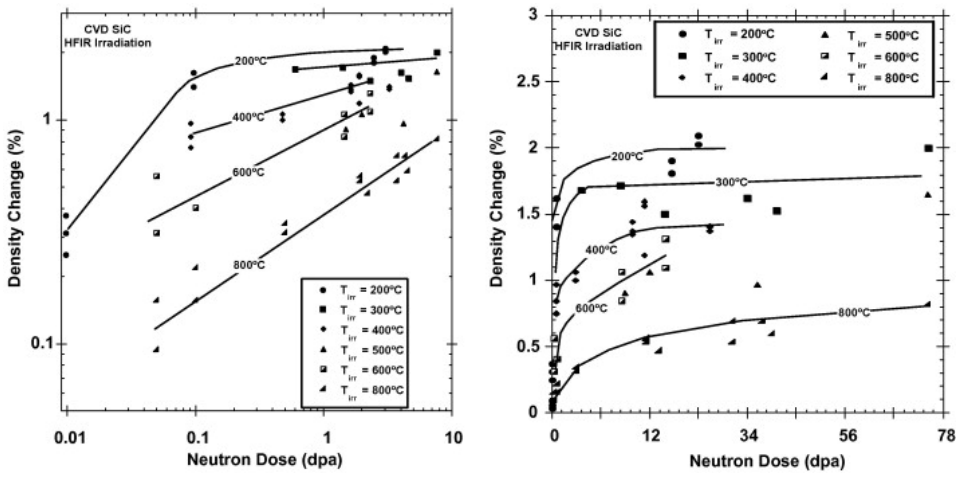

Figure 2. 16 Swelling and saturation of neutron-irradiated SiC versus irradiation conditions. Image is taken from reference [95].

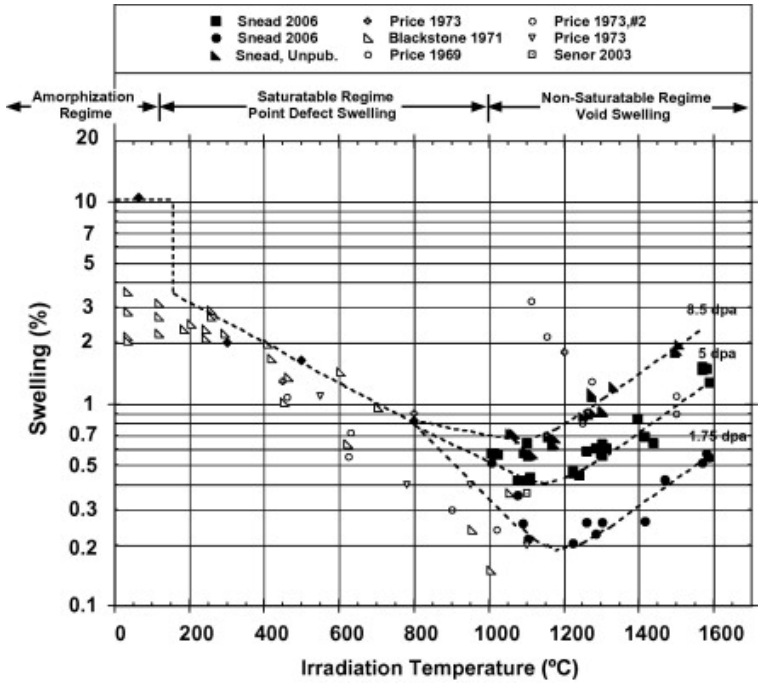

Figure 2. 17 Swelling of irradiated SiC as a function of irradiation temperature and damage level. Image is taken from reference [95] and references corresponding to different symbols in this pictures are also from [95].

At temperature from 1000 °C to 1600 °C, vacancy with sufficient mobility could combine with other vacancies to form 3D cavities (also called as voids) [138]. Swelling in that temperature range was found to increase with damage level and irradiation temperature, which was mainly attributed to enhancement role of high irradiation temperature and high damage level in production and growth of voids [95]. For example, at temperatures between 1100-1200 °C, volumetric swelling in neutron irradiated SiC increased from 0.2% at damage level of 2 dpa to 0.4% at damage level of 6 dpa. At temperature higher than 1200 °C, swelling increased with irradiation temperature up to 1500 °C and damage level. Maximum volumetric swelling of 1.5% could be achieved in SiC irradiated by neutron at damage level of 6 dpa at irradiation temperature of ~1470 °C [134]. Moreover, swelling saturation was not observed at that temperature range according to current available data. Figure 2. 17 shows summary of irradiation-induced swelling in SiC under different irradiation conditions [95].

2.11 Effects of irradiation on thermal conductivity

Thermal conductivity degradation was observed for SiC irradiated at different conditions, which was described using different items, like normalized thermal conductivity degradation ($(K_{unirr}-K_{irr})/K_{unirr}$),

and thermal defect resistance ($\Delta(1/K_{irr}-1/K_{unirr})$) [139]. Thermal defect resistance was able to better describe effects of damage level on thermal conductivity degradation in same materials with different grades as long as they possessed similar irradiation-induced microstructure [139].

At low irradiation temperature (60 °C) and low damage level (0.01 dpa), significant thermal conductivity degradation from 245 W/(m•K) to 30 W/(m•K) took place in neutron irradiated CVD-SiC [139]. Thermal conductivity of the CVD-SiC further reduced to 3.8 W/(m•K) as damage level was increased to 2.6 dpa, which was accompanied by presence of amorphous SiC and volumetric swelling of 9.62% [139]. Furthermore, above mentioned thermal defect resistance of the CVD-SiC after irradiation showed a sublinear dependence on damage level (from 0.01 dpa to 0.1 dpa), implying strong phonon scattering by point defects or aggregation of point defects [139]. It is also noted that thermal defect resistance of sintered SiC was higher than counterpart of CVD-SiC despite they were exposed to same irradiation conditions, which was possibly attributed to increased phonon-grain boundary scattering originating from segregation of impurity/sintering additive in grain boundary and enhanced nucleation of defect clusters [139].

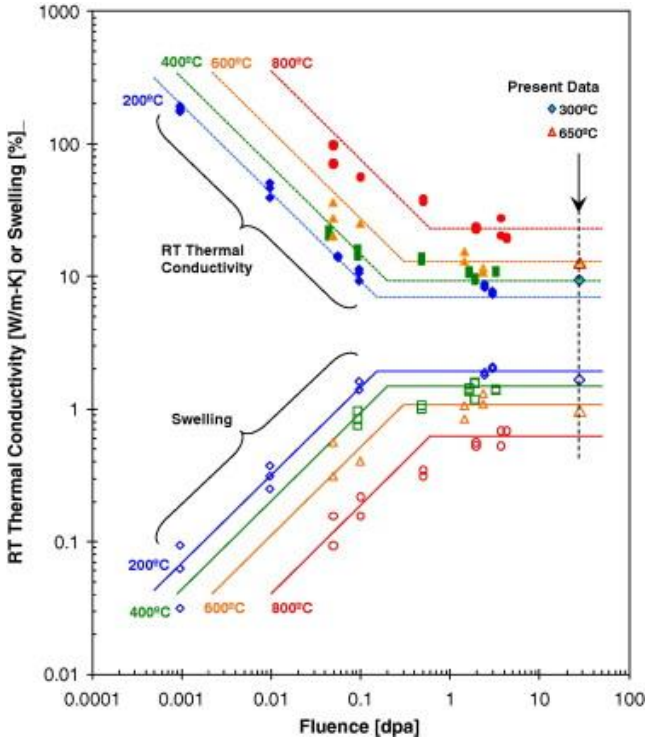

Figure 2. 18 Thermal conductivity and swelling at room temperature of SiC ceramics irradiated at different temperatures and damage level (also called as fluence). Picture is taken from reference [134].

At temperature ranging from 150 °C to 800 °C, it was found that the room temperature thermal conductivity of neutron irradiated CVD-SiC decreased very quickly with damage level until a saturated value which was achieved at very low damage level (<1 dpa), as shown in Figure 2. 18 [134]. In addition, Figure 2. 18 demonstrates that the swelling at room temperature increased with damage level until a saturated value [134]. The saturated swelling level decreased with increasing irradiation temperature while the saturated thermal conductivity showed opposite trend. In the temperature range (150~800 °C), irradiation induced defects accumulated with damage level up to a saturated level, which were thought to dominate swelling behavior and thermal conductivity degradation [134]. The temperature dependence of saturated swelling level and thermal conductivity was mainly attributed to enhanced recombination and/or coalescence of irradiation induced Frenkel pair originating from higher mobility of interstitial at higher temperatures [137]. Furthermore, it was suggested that immobile defect and defect cluster (e.g. vacancy, vacancy cluster and antisite defects) acted as main phonon scattering sources [139, 140]. Khafizov et al. have correlated the irradiation induced defects/defect clusters with thermal conductivity degradation of CeO_2 ceramics via fitting

experimental results with the Klemen-Callaway model. It was reported that the conductivity reduction was mainly dominated by the Frank faulted dislocation loops (large immobile interstitial clusters) rather than point defects and voids [130]. In addition, contribution from the highly mobile interstitials to thermal conductivity degradation was assumed to be small because interstitials tend to recombine with adjacent vacancy and/or form interstitial clusters due to their much lower migration energy than counterparts of other defects/defect clusters and higher strain energy than that of interstitial clusters with same amount of interstitials [139, 141].

At temperature above 1100 °C, thermal conductivity decreased with damage level and did not show saturated values [134]. In addition, linear/sublinear dependence of thermal defect resistance on damage level was not observed [134]. As mentioned above, at high irradiation temperature, sufficiently mobile vacancy could form three-dimensional defects (i.e. cavities and precipitates) in stacking fault and/or grain boundaries [133]. These three-dimensional defects have not demonstrated saturation behavior similar to the dominant irradiation induced defects within low temperature range (<800 °C). Besides, thermal defect resistance of SiC at high irradiation temperature range (>1100 °C) were smaller than counterpart of SiC irradiated at low temperature range (<800 °C), suggesting weaker scattering by these three-dimensional defects [134, 142].

Although thermal conductivity degradation is inevitable in irradiated SiC, it was reported that irradiation-induced thermal defect resistance could be reduced by isothermal annealing on irradiated SiC [139]. It was found that thermal defect resistance of the CVD-SiC irradiated by neutron with damage level of 0.01 dpa at 60 °C decreased with annealing temperature and could reduce to 0 when the annealing temperature and holding time were 1050 °C and 60 min respectively. In contrast, thermal conductivity of SiC irradiated by neutron with high damage level of 1.5 dpa only recovered to 25% of its unirradiated value even at higher annealing temperature of 1200 °C, which may be caused by high thermal stability of larger defect clusters formed at high damage level [139].

2.12 Summary of part III

In part III of chapter 2, irradiation types are simply compared. Moreover, evolution of microstructure and thermal conductivity under irradiation are reviewed, which could be summarized as follows:

(1) Proton is more preferred than heavy ion (e.g. silicon ion and carbon ion) for simulating neutron irradiation effects on microstructure and property evolution of SiC ceramics because of its larger penetration depth and more uniform damage profile.

(2) Type, size and number density of irradiation induced defects in CVD-SiC are determined by irradiation temperature and damage level. Increasing irradiation temperature results in higher mobility of point defects and enhanced recombination and clustering. Higher damage level further promotes formation and growth of defect clusters.

(3) With increasing irradiation temperature, swelling regimes are divided into 3 parts: amorphization at low temperature (<150 °C), saturable regime (250-1000 °C), and non-saturable regime (1000-1600 °C).

(4) Thermal conductivity degradation is observed after irradiation and such degradation is related to defect types generated under different irradiation conditions. Specifically, conductivity degradation at high irradiation temperature is dominated by the phonon-voids scattering process while phonon-point defects/defect clusters scattering dominates conductivity degradation at low irradiation temperature.

References

[1] K. Raju, D.-H. Yoon, Sintering additives for SiC based on the reactivity: a review, Ceramics International 42(16) (2016) 17947-17962.

[2] R. Cheung, Silicon carbide microelectromechanical systems for harsh environments, World Scientific (2006).

[3] N.G. Szwacki, Structural and electronic properties of silicon carbide polytypes as predicted by exact exchange calculations, Computational Condensed Matter 13 (2017) 55-58.

[4] K. Biswas, Solid state sintering of SiC-ceramics, Materials Science Forum, Trans Tech Publ, (2009), 71-89.

[5] Y.-W. Kim, Y.-S. Chun, T. Nishimura, M. Mitomo, Y.-H. Lee, High-temperature strength of silicon carbide ceramics sintered with rare-earth oxide and aluminum nitride, Acta Materialia 55(2) (2007) 727-736.

[6] G.A. Slack, Thermal conductivity of pure and impure silicon, silicon carbide, and diamond, Journal of Applied physics 35(12) (1964) 3460-3466.

[7] S.J. Zinkle, K.A. Terrani, J.C. Gehin, L.J. Ott, L.L. Snead, Accident tolerant fuels for LWRs: A perspective, Journal of Nuclear Materials 448(1-3) (2014) 374-379.

[8] J. Ness, T. Page, Microstructural evolution in reaction-bonded silicon carbide, Journal of Materials Science 21(4) (1986) 1377-1397.

[9] M. Steen, L. Ranzani, Potential of SiC as a heat exchanger material in combined cycle plant, Ceramics international 26(8) (2000) 849-854.

[10] L. Hallstadius, S. Johnson, E. Lahoda, Cladding for high performance fuel, Progress in Nuclear Energy 57 (2012) 71-76.

[11] J. Hong, M. Hon, R. Davis, Self-diffusion in alpha and beta silicon carbide, Ceramurgia International 5(4) (1979) 155-160.

[12] C. Greskovich, J. Rosolowski, Sintering of covalent solids, Journal of the American Ceramic Society 59(7‐8) (1976) 336-343.

[13] J. Drowart, G. De Maria, M.G. Inghram, Thermodynamic study of SiC utilizing a mass spectrometer, The Journal of Chemical Physics 29(5) (1958) 1015-1021.

[14] X. Mao-lin, L. De-li, X. Xiao-Bin, L. Bang-yi, C. Chang'an, L. Wei-yuan, Densification of nano-SiC by ultra-high pressure effects of time, temperature and pressure, Fusion engineering and design 85(7-9) (2010) 964-968.

[15] J.S. Nadeau, N. JS, Very high pressure hot pressing of silicon carbide, (1973).

[16] S. PROCHAZKA, R.M. SCANLAN, Effect of boron and carbon on sintering of SiC, Journal of the American Ceramic Society 58(1‐2) (1975) 72-72.

[17] H. Gu, Y. Shinoda, F. Wakai, Detection of Boron Segregation to Grain Boundaries in Silicon Carbide by Spatially Resolved Electron Energy‐Loss Spectroscopy, Journal of the American Ceramic Society 82(2) (1999) 469-472.

[18] D.P. Birnie III, A Model for Silicon Self-Diffusion in Silicon Carbide: Anti‐Site Defect Motion, Journal of the American Ceramic Society 69(2) (1986) C‐33-C‐35.

[19] M. Datta, A. Bandyopadhyay, B. Chaudhuri, Sintering of nano crystalline α silicon carbide doping with aluminium nitride, Bulletin of Materials Science 25(2) (2002) 121-125.

[20] L. Stobierski, A. Gubernat, Sintering of silicon carbide II. Effect of boron, Ceramics international 29(4) (2003) 355-361.

[21] P.T. Shaffer, The SiC phase in the system SiC-B_4C-C, Materials Research Bulletin 4(3) (1969) 213-219.

[22] H.-M. Kim, Y.-W. Kim, K.-Y. Lim, Pressureless sintered silicon carbide matrix with a new quaternary additive for fully ceramic microencapsulated fuels, Journal of the European Ceramic Society 39(14) (2019) 3971-3980.

[23] K. Kaneko, M. Kawasaki, T. Nagano, N. Tamari, S. Tsurekawa, Determination of the chemical width of grain boundaries of boron-and carbon-doped hot-pressed β-SiC by HAADF imaging and ELNES line-profile, Acta materialia 48(4) (2000) 903-910.

[24] R.M. German, P. Suri, S.J. Park, Review: liquid phase sintering, J. Mater. Sci 44(1) (2009) 1-39.

[25] Y.-H. Kim, Y.-W. Kim, K.-Y. Lim, S.-J. Lee, Mechanical and thermal properties of silicon carbide ceramics with yttria–scandia–magnesia, Journal of the European Ceramic Society 39(2) (2019) 144-149.

[26] Y.-W. Kim, S.H. Jang, T. Nishimura, S.-Y. Choi, S.-D. Kim, Microstructure and high-temperature strength of silicon carbide with 2000 ppm yttria, Journal of the European Ceramic Society 37(15) (2017) 4449-4455.

[27] J. Roy, S. Chandra, S. Das, S. Maitra, Oxidation behaviour of silicon carbide - A review, Reviews on Advanced Materials Science 38(1) (2014) 29-39.

[28] S.-J.L. Kang, Sintering: densification, grain growth and microstructure, Elsevier (2004).

[29] W. Kingery, Densification during sintering in the presence of a liquid phase. I. Theory, Journal of Applied Physics 30(3) (1959) 301-306.

[30] F. Lange, Hot-pressing behaviour of silicon carbide powders with additions of aluminium oxide, Journal of Materials Science 10(2) (1975) 314-320.

[31] R. Malik, Y.-H. Kim, Y.-W. Kim, Effect of additive content on the mechanical and thermal properties of pressureless liquid-phase sintered SiC, Journal of Asian Ceramic Societies 8(2) (2020) 448-459.

[32] M. khodaei, O. yaghobizadeh, S.H. Naghavi Alhosseini, S. esmaeeli, S.R. Mousavi, The effect of oxide, carbide, nitride and boride additives on properties of pressureless sintered SiC: A review, Journal of the European Ceramic Society 39(7) (2019) 2215-2231.

[33] N.P. Padture, In situ-toughened silicon carbide, Journal of the American Ceramic Society 77(2) (1994) 519-523.

[34] S. Taguchi, F. Motta, R. Balestra, S. Ribeiro, Wetting behaviour of SiC ceramics: part II—Y_2O_3/Al_2O_3 and Sm_2O_3/Al_2O_3, Materials Letters 58(22-23) (2004) 2810-2814.

[35] U. Kolitsch, H. Seifert, T. Ludwig, F. Aldinger, Phase equilibria and crystal chemistry in the Y_2O_3-Al_2O_3-SiO_2 system, Journal of materials research 14(2) (1999) 447-455.

[36] J.H. Eom, Y.K. Seo, Y.W. Kim, Mechanical and thermal properties of pressureless sintered silicon carbide ceramics with alumina–yttria–calcia, Journal of the American Ceramic Society 99(5) (2016) 1735-1741.

[37] Y. Jiang, L. Wu, Z. Wei, Z. Huang, Phase relations in the SiC–Al_2O_3–Y_2O_3 system, Materials Letters 165 (2016) 26-28.

[38] M. Mulla, V. Krstic, Pressureless sintering of β-SiC with Al_2O_3 additions, Journal of Materials science 29(4) (1994) 934-938.

[39] Y. Zhou, H. Tanaka, S. Otani, Y. Bando, Low-Temperature Pressureless Sintering of alpha-SiC with Al_4C_3-B_4C-C Additions, Journal of the American Ceramic Society 82(8) (1999) 1959-1964.

[40] Y. Inomata, PHASE RELATION IN SIC-Al_4C_3-B_4C SYSTEM AT 1800 °C, (1980).

[41] M.N. Rahaman, Ceramic processing and sintering, CRC press (2003).

[42] Z.A. Munir, D.V. Quach, M. Ohyanagi, Electric current activation of sintering: a review of the pulsed electric current sintering process, Journal of the American Ceramic Society 94(1) (2011) 1-19.

[43] Z. Munir, U. Anselmi-Tamburini, M. Ohyanagi, The effect of electric field and pressure on the synthesis and consolidation of materials: A review of the spark plasma sintering method, Journal of materials science 41(3) (2006) 763-777.

[44] M. Sakkaki, F.S. Moghanlou, M. Vajdi, M.S. Asl, M. Mohammadi, M. Shokouhimehr, Numerical simulation of heat transfer during spark plasma sintering of zirconium diboride, Ceramics International 46(4) (2020) 4998-5007.

[45] S. Deng, R. Li, T. Yuan, P. Cao, S. Xie, Electromigration-enhanced densification kinetics during spark plasma sintering of tungsten powder, Metallurgical and Materials Transactions A 50(6) (2019) 2886-2897.

[46] S. Deng, T. Yuan, R. Li, M. Zhang, S. Xie, M. Wang, L. Li, J. Yuan, Q. Weng, Influence of electric current on interdiffusion kinetics of W-Ti system during spark plasma sintering, International Journal of Refractory Metals and Hard Materials 75 (2018) 184-190.

[47] J.E. Garay, S.C. Glade, U. Anselmi-Tamburini, P. Asoka-Kumar, Z.A. Munir, Electric current enhanced defect mobility in Ni 3 Ti intermetallics, Applied Physics Letters 85(4) (2004) 573-575.

[48] P. Asoka-Kumar, M. Alatalo, V. Ghosh, A. Kruseman, B. Nielsen, K. Lynn, Increased elemental specificity of positron annihilation spectra, Physical Review Letters 77(10) (1996) 2097.

[49] C.-Y. Lan, C.-Y. Hsu, Y.-C. Lee, C.-N. Liao, Grain growth behavior and enhanced thermoelectric properties of PbTe consolidated by high-density pulse current, Journal of Alloys and Compounds 815 (2020) 152658.

[50] N. Chawake, P. Ghosh, L. Raman, A.K. Srivastav, T. Paul, S.P. Harimkar, J. Eckert, R.S. Kottada, Estimation of diffusivity from densification data obtained during spark plasma sintering, Scripta Materialia 161 (2019) 36-39.

[51] Z. Shen, M. Johnsson, Z. Zhao, M. Nygren, Spark plasma sintering of alumina, Journal of the American Ceramic Society 85(8) (2002) 1921-1927.

[52] Y. Shinoda, Y. Suzuki, K. Yoshida, Electric field effect on texture formation of mullite in spark plasma sintered SiC with Al_2O_3-SiO_2 additive, Scripta Materialia 100 (2015) 51-54.

[53] D.M. Hulbert, A. Anders, J. Andersson, E.J. Lavernia, A.K. Mukherjee, A discussion on the absence of plasma in spark plasma sintering, Scripta Materialia 60(10) (2009) 835-838.

[54] Z.-H. Zhang, Z.-F. Liu, J.-F. Lu, X.-B. Shen, F.-C. Wang, Y.-D. Wang, The sintering mechanism in spark plasma sintering–proof of the occurrence of spark discharge, Scripta materialia 81 (2014) 56-59.

[55] Z.-Y. Hu, Z.-H. Zhang, X.-W. Cheng, F.-C. Wang, Y.-F. Zhang, S.-L. Li, A review of multi-physical fields induced phenomena and effects in spark plasma sintering: Fundamentals and applications, Materials & Design 191 (2020) 108662.

[56] M. Tokita, Development of large-size ceramic/metal bulk FGM fabricated by spark plasma sintering, Materials science forum, Trans Tech Publ, (1999) 83-88.

[57] Z. Trzaska, A. Couret, J.-P. Monchoux, Spark plasma sintering mechanisms at the necks between TiAl powder particles, Acta Materialia 118 (2016) 100-108.

[58] R. Chaim, Densification mechanisms in spark plasma sintering of nanocrystalline ceramics, Materials Science and Engineering: A 443(1-2) (2007) 25-32.

[59] R. Marder, C. Estournès, G. Chevallier, R. Chaim, Spark and plasma in spark plasma sintering of rigid ceramic nanoparticles: A model system of YAG, Journal of the European Ceramic Society 35(1) (2015) 211-218.

[60] J. Trapp, A. Semenov, O. Eberhardt, M. Nöthe, T. Wallmersperger, B. Kieback, Fundamental principles of spark plasma sintering of metals: part II–about the existence or non-existence of the 'spark plasma effect', Powder Metallurgy 63(5) (2020) 312-328.

[61] E.A. Olevsky, S. Kandukuri, L. Froyen, Consolidation enhancement in spark-plasma sintering: Impact of high heating rates, Journal of Applied Physics 102(11) (2007) 114913.

[62] T. Yamamoto, H. Kitaura, Y. Kodera, T. Ishii, M. Ohyanagi, Z.A. Munir, Consolidation of nanostructured β-SiC by spark plasma sintering, Journal of the American ceramic Society 87(8) (2004) 1436-1441.

[63] J.S. Lee, Y.S. Ahn, T. Nishimura, H. Tanaka, S.H. Lee, Ultra-Low-Temperature Sintering of Nanostructured β-SiC, Journal of the American Ceramic Society 94(2) (2011) 324-327.

[64] L.S. Sigl, H.J. Kleebe, Core/Rim Structure of Liquid-Phase-Sintered Silicon Carbide, Journal of the American Ceramic Society 76(3) (1993) 773-776.

[65] H. Ye, V. Pujar, N. Padture, Coarsening in liquid-phase-sintered α-SiC, Acta materialia 47(2) (1999) 481-487.

[66] Y.-W. Kim, M. Mitomo, G.-D. Zhan, Mechanism of grain growth in liquid-phase-sintered β–SiC, Journal of materials research 14(11) (1999) 4291-4293.

[67] H. Xu, T. Bhatia, S.A. Deshpande, N.P. Padture, A.L. Ortiz, F.L. Cumbrera, Microstructural evolution in liquid-phase-sintered SiC: part I, effect of starting powder, Journal of the American Ceramic Society 84(7) (2001) 1578-1584.

[68] L. Falk, Microstructural development during liquid phase sintering of silicon carbide ceramics, Journal of the European Ceramic Society 17(8) (1997) 983-994.

[69] W.F. Knippenberg, Growth phenomena in silicon carbide, Philips Research Report 18 (1963) 161-274.

[70] Y. Inomata, Z. Inoue, M. Mitomo, H. Tanaka, Polytypes of SiC crystals grown from molten silicon, EMMANUEL COLL BOSTON MASS ORIENTAL SCIENCE RESEARCH LIBRARY, (1970).

[71] H. Tanaka, Silicon carbide powder and sintered materials, Journal of the ceramic society of Japan 119(1387) (2011) 218-233.

[72] N. Jepps, T. Page, Polytypic transformations in silicon carbide, Progress in crystal growth and characterization 7(1-4) (1983) 259-307.

[73] A. Heuer, G. Fryburg, L. Ogbuji, T. Mitchell, S. Shinozaki, β→α transformation in polycrystalline SiC: I, microstructural aspects, Journal of the American Ceramic Society 61(9-10) (1978) 406-412.

[74] L. Ogbuji, T. Mitchell, A. Heuer, The β→α Transformation in poly crystalline SiC: III, the thickening of α plates, Journal of the American Ceramic Society 64(2) (1981) 91-99.

[75] L. Ogbuji, T. Mitchell, A. Heuer, S. Shinozaki, The β→α transformation in polycrystalline SiC: IV, a comparison of conventionally sintered, hot-pressed, reaction-sintered, and chemically vapor-deposited samples, Journal of the American Ceramic Society 64(2) (1981) 100-105.

[76] M. Lodhe, N. Chawake, D. Yadav, M. Balasubramanian, On correlation between β→α transformation and densification mechanisms in SiC during spark plasma sintering, Scripta Materialia 115 (2016) 137-140.

[77] S.A. Deshpande, T. Bhatia, H. Xu, N.P. Padture, A.L. Ortiz, F.L. Cumbrera, Microstructural Evolution in Liquid-Phase-Sintered SiC: Part II, Effects of Planar Defects and Seeds in the Starting Powder, Journal of the American Ceramic Society 84(7) (2001) 1585-1590.

[78] R. Malik, Y.W. Kim, W.H. Nam, Intrinsic microstructures of silica-bonded porous nano-SiC ceramics, Journal of the American Ceramic Society (2021).

[79] A.L. Ortiz, T. Bhatia, N.P. Padture, G. Pezzotti, Microstructural Evolution in Liquid-Phase-Sintered SiC: Part III, Effect of Nitrogen-Gas Sintering Atmosphere, Journal of the American Ceramic Society 85(7) (2002) 1835-1840.

[80] Y.-H. Kim, Y.-W. Kim, Direct bonding of silicon carbide ceramics sintered with yttria, Journal of the European Ceramic Society 39(15) (2019) 4487-4494.

[81] J.J. Cao, W. Chan, L.C. De Jonghe, C.J. Gilbert, R.O. Ritchie, In Situ Toughened Silicon Carbide with Al-B-C Additions, Journal of the American Ceramic Society 79(2) (1995).

[82] E. Volz, A. Roosen, S.-C. Wang, W.-C. Wei, Formation of intergranular amorphous films during the microstructural development of liquid phase sintered silicon carbide ceramics, Journal of materials science 39(13) (2004) 4095-4101.

[83] H. Nakano, K. Watari, Y. Kinemuchi, K. Ishizaki, K. Urabe, Microstructural characterization of high-thermal-conductivity SiC ceramics, Journal of the European Ceramic Society 24(14) (2004) 3685-3690.

[84] Y.W. Kim, K.Y. Lim, W.S. Seo, Microstructure and thermal conductivity of silicon carbide with yttria and scandia, Journal of the American Ceramic Society 97(3) (2014) 923-928.

[85] T. Kusunose, T. Sekino, Increasing resistivity of electrically conductive ceramics by insulating grain boundary phase, ACS applied materials & interfaces 6(4) (2014) 2759-2763.

[86] S. Ge, X. Yao, Y. Liu, H. Duan, Z. Huang, X. Liu, Effect of Sintering Temperature on the Properties of Highly Electrical Resistive SiC Ceramics as a Function of Y_2O_3-Er_2O_3 Additions, Materials 13(21) (2020) 4768.

[87] P.R. Cantwell, M. Tang, S.J. Dillon, J. Luo, G.S. Rohrer, M.P. Harmer, Grain boundary complexions, Acta Materialia 62 (2014) 1-48.

[88] T.M. Tritt, Thermal conductivity: theory, properties, and applications, Springer Science & Business Media (2005).

[89] J. Callaway, Model for lattice thermal conductivity at low temperatures, Physical Review 113(4) (1959) 1046.

[90] P. Klemens, Thermal conductivity and lattice vibrational modes, Solid state physics, Elsevier (1958), 1-98.

[91] K. Watari, H. Nakano, K. Sato, K. Urabe, K. Ishizaki, S. Cao, K. Mori, Effect of grain boundaries on thermal conductivity of silicon carbide ceramic at 5 to 1300 K, Journal of the American Ceramic Society 86(10) (2003) 1812-1814.

[92] G.A. Slack, Nonmetallic crystals with high thermal conductivity, Journal of Physics and Chemistry of Solids 34(2) (1973) 321-335.

[93] T. Sakai, T. Aikawa, Phase Transformation and Thermal Conductivity of Hot-Pressed Silicon Carbide Containing Alumina and Carbon, Journal of the American Ceramic Society 71(1) (1988) C-7-C-9.

[94] A. Collins, M.A. Pickering, R.L. Taylor, Grain size dependence of the thermal conductivity of polycrystalline chemical vapor deposited β-SiC at low temperatures, Journal of applied physics 68(12) (1990) 6510-6512.

[95] L.L. Snead, T. Nozawa, Y. Katoh, T.-S. Byun, S. Kondo, D.A. Petti, Handbook of SiC properties for fuel performance modeling, Journal of nuclear materials 371(1-3) (2007) 329-377.

[96] H.-S. Yang, G.-R. Bai, L. Thompson, J. Eastman, Interfacial thermal resistance in nanocrystalline yttria-stabilized zirconia, Acta Materialia 50(9) (2002) 2309-2317.

[97] M. Maldovan, Thermal energy transport model for macro-to-nanograin polycrystalline semiconductors, Journal of Applied Physics 110(11) (2011) 114310.

[98] C. Wan, W. Pan, Q. Xu, Y. Qin, J. Wang, Z. Qu, M. Fang, Effect of point defects on the thermal transport properties of $(La_xGd_{1-x})_2Zr_2O_7$: Experiment and theoretical model, Physical Review B 74(14) (2006) 144109.

[99] R. Munro, Material properties of a sintered α-SiC, Journal of Physical and Chemical Reference Data 26(5) (1997) 1195-1203.

[100] T. Klitsner, R. Pohl, Phonon scattering at silicon crystal surfaces, Physical Review B 36(12) (1987) 6551.

[101] J.-P. Crocombette, L. Gelebart, Multiscale modeling of the thermal conductivity of polycrystalline silicon carbide, Journal of Applied Physics 106(8) (2009) 083520.

[102] N. Goel, E. Webb III, A. Oztekin, J. Rickman, S. Neti, Kapitza resistance at segregated boundaries in β-SiC, Journal of Applied Physics 118(11) (2015) 115101.

[103] C.B. Carter, M.G. Norton, Ceramic materials: science and engineering, Springer (2007).

[104] P. Klemens, The scattering of low-frequency lattice waves by static imperfections, Proceedings of the Physical Society. Section A 68(12) (1955) 1113.

[105] J. Li, L. Porter, S. Yip, Atomistic modeling of finite-temperature properties of crystalline β-SiC: II. Thermal conductivity and effects of point defects, Journal of Nuclear Materials 255(2-3) (1998) 139-152.

[106] Y. Zhou, K. Hirao, Y. Yamauchi, S. Kanzaki, Effects of rare-earth oxide and alumina additives on thermal conductivity of liquid-phase-sintered silicon carbide, Journal of materials research 18(8) (2003) 1854-1862.

[107] T. Kinoshita, S. Munekawa, Effect of grain boundary segregation on thermal conductivity of hot-pressed silicon carbide, Acta materialia 45(5) (1997) 2001-2012.

[108] R. Progelhof, J. Throne, R. Ruetsch, Methods for predicting the thermal conductivity of composite systems: a review, Polymer Engineering & Science 16(9) (1976) 615-625.

[109] K. Pietrak, T.S. Wiśniewski, A review of models for effective thermal conductivity of composite materials, Journal of Power Technologies 95(1) (2014) 14-24.

[110] J.C. Maxwell, A treatise on electricity and magnetism, Clarendon press (1873).

[111] V.D. Bruggeman, Berechnung verschiedener physikalischer Konstanten von heterogenen Substanzen. I. Dielektrizitätskonstanten und Leitfähigkeiten der Mischkörper aus isotropen Substanzen, Annalen der physik 416(7) (1935) 636-664.

[112] P. Cosenza, A. Ghorbani, C. Camerlynck, F. Rejiba, R. Guérin, A. Tabbagh, Effective medium theories for modelling the relationships between electromagnetic properties and hydrological variables in geomaterials: a review, Near Surface Geophysics 7(5-6) (2009) 563-578.

[113] R. Landauer, The electrical resistance of binary metallic mixtures, Journal of Applied Physics 23(7) (1952) 779-784.

[114] L. Sigl, Thermal conductivity of liquid phase sintered silicon carbide, Journal of the European Ceramic Society 23(7) (2003) 1115-1122.

[115] C. Zhang, X. Yao, Y. Li, H. Liang, J. Chen, J. Zhang, J. Yang, X. Li, T. Qiu, Z. Chen, Effect of AlN addition on the thermal conductivity of pressureless sintered SiC ceramics, Ceramics International 41(7) (2015) 9107-9114.

[116] D. Hasselman, L.F. Johnson, Effective thermal conductivity of composites with interfacial thermal barrier resistance, Journal of composite materials 21(6) (1987) 508-515.

[117] F. Yang, X. Zhao, P. Xiao, Thermal conductivities of YSZ/Al_2O_3 composites, Journal of the European Ceramic Society 30(15) (2010) 3111-3116.

[118] E.T. Swartz, R.O. Pohl, Thermal boundary resistance, Reviews of modern physics 61(3) (1989) 605.

[119] Y. Zhang, H. Zhang, J. Wu, X. Wang, Enhanced thermal conductivity in copper matrix composites reinforced with titanium-coated diamond particles, Scripta Materialia 65(12) (2011) 1097-1100.

[120] X. Dong, Y.C. Shin, Multiscale genome modeling for predicting the thermal conductivity of silicon carbide ceramics, Journal of the American Ceramic Society 99(12) (2016) 4073-4082.

[121] Y.-K. Seo, Y.-W. Kim, K.J. Kim, W.-S. Seo, Electrically conductive SiC-BN composites, Journal of the European Ceramic Society 36(16) (2016) 3879-3887.

[122] S.H. Jang, Y.W. Kim, K.J. Kim, S.J. Lee, K.Y. Lim, Effects of Y_2O_3–RE_2O_3 (RE= Sm, Gd, Lu) Additives on Electrical and Thermal Properties of Silicon Carbide Ceramics, Journal of the American Ceramic Society 99(1) (2016) 265-272.

[123] K.A. Terrani, B.A. Pint, C.M. Parish, C.M. Silva, L.L. Snead, Y. Katoh, Silicon carbide oxidation in steam up to 2 MPa, Journal of the American Ceramic Society 97(8) (2014) 2331-2352.

[124] G. Was, J. Busby, T. Allen, E. Kenik, A. Jensson, S. Bruemmer, J. Gan, A. Edwards, P. Scott, P. Andreson, Emulation of neutron irradiation effects with protons: validation of principle, Journal of nuclear materials 300(2-3) (2002) 198-216.

[125] P. Wady, A. Draude, S. Shubeita, A. Smith, N. Mason, S. Pimblott, E. Jimenez-Melero, Accelerated radiation damage test facility using a 5 MV tandem ion accelerator, Nuclear Instruments and Methods in Physics Research Section A: Accelerators, Spectrometers, Detectors and Associated Equipment 806 (2016) 109-116.

[126] X. Wang, H. Zhang, T. Baba, H. Jiang, C. Liu, Y. Guan, O. Elleuch, T. Kuech, D. Morgan, J.-C. Idrobo, Radiation-induced segregation in a ceramic, Nature Materials (2020) 1-7.

[127] M. Khafizov, C. Yablinsky, T.R. Allen, D.H. Hurley, Measurement of thermal conductivity in proton irradiated silicon, Nuclear Instruments and Methods in Physics Research Section B: Beam Interactions with Materials and Atoms 325 (2014) 11-14.

[128] A. Aitkaliyeva, L. He, H. Wen, B. Miller, X.-M. Bai, T. Allen, Irradiation effects in Generation IV nuclear reactor materials, Structural Materials for Generation IV Nuclear Reactors, Elsevier (2017), 253-283.

[129] Y. Katoh, N. Hashimoto, S. Kondo, L. Snead, A. Kohyama, Microstructural development in cubic silicon carbide during irradiation at elevated temperatures, Journal of nuclear materials 351(1-3) (2006) 228-240.

[130] M. Khafizov, J. Pakarinen, L. He, D.H. Hurley, Impact of irradiation induced dislocation loops on thermal conductivity in ceramics, Journal of the American Ceramic Society 102(12) (2019) 7533-7542.

[131] W.J. Weber, W. Jiang, S. Thevuthasan, Accumulation, dynamic annealing and thermal recovery of ion-beam-induced disorder in silicon carbide, Nuclear Instruments and Methods in Physics Research Section B: Beam Interactions with Materials and Atoms 175 (2001) 26-30.

[132] F. Gao, W.J. Weber, M. Posselt, V. Belko, Atomistic study of intrinsic defect migration in 3C-SiC, Physical Review B 69(24) (2004) 245205.

[133] S. Kondo, Y. Katoh, L.L. Snead, Microstructural defects in SiC neutron irradiated at very high temperatures, Journal of Nuclear Materials 382(2-3) (2008) 160-169.

[134] L.L. Snead, Y. Katoh, S. Connery, Swelling of SiC at intermediate and high irradiation temperatures, Journal of nuclear materials 367 (2007) 677-684.

[135] J.B. Malherbe, Diffusion of fission products and radiation damage in SiC, Journal of Physics D: Applied Physics 46(47) (2013) 473001.

[136] A. Debelle, A. Boulle, A. Chartier, F. Gao, W.J. Weber, Interplay between atomic disorder, lattice swelling, and defect energy in ion-irradiation-induced amorphization of SiC, Physical Review B 90(17) (2014) 174112.

[137] M. Hernández-Mayoral, M. Caturla, Microstructure evolution of irradiated structural materials in nuclear power plants, Understanding and Mitigating Ageing in Nuclear Power Plants, Elsevier (2010), 189-235.

[138] A. Kawasuso, H. Itoh, N. Morishita, M. Yoshikawa, T. Ohshima, I. Nashiyama, S. Okada, H. Okumura, S. Yoshida, Silicon vacancies in 3C-SiC observed by positron lifetime and electron spin resonance, Applied physics A 67(2) (1998) 209-212.

[139] L. Snead, S. Zinkle, D. White, Thermal conductivity degradation of ceramic materials due to low temperature, low dose neutron irradiation, Journal of nuclear materials 340(2-3) (2005) 187-202.

[140] Y. Katoh, L.L. Snead, T. Nozawa, S. Kondo, J.T. Busby, Thermophysical and mechanical properties of near-stoichiometric fiber CVI SiC/SiC composites after neutron irradiation at elevated temperatures, Journal of Nuclear Materials 403(1-3) (2010) 48-61.

[141] N. Swaminathan, D. Morgan, I. Szlufarska, Role of recombination kinetics and grain size in radiation-induced amorphization, Physical Review B 86(21) (2012) 214110.

[142] G. Samolyuk, S. Golubov, Y. Osetsky, R. Stoller, Molecular dynamics study of influence of vacancy types defects on thermal conductivity of β-SiC, Journal of nuclear materials 418(1-3) (2011) 174-181.

Chapter 3 Articles

3.1 Overview of Articles

The following articles are aimed at studying effects of sintering additive, microstructure, and proton irradiation on thermal conductivity of spark plasma sintered SiC ceramics.

Article I investigates effects of the sintering additive (Al_2O_3-Y_2O_3) on thermal conductivity of SiC ceramics. Continuous network of sintering additive formed as the holding time was prolonged, as verified by HAADF and STEM-EDS results. Such distribution change was correlated with thermal conductivity reduction. Furthermore, importance of grain size and sintering additive content in affecting thermal conductivity was figured out by combing experimental data with a macroscopic heat conduction model.

Article II focuses on the grain growth and thermal conductivity dependence on grain growth. The sintering additive Al_2O_3-Y_2O_3 was substituted with Y_2O_3-Sc_2O_3 to avoid Al doping into SiC lattice which reduces thermal conductivity of SiC ceramics. Grain growth mechanism in the SiC ceramics with Y_2O_3-Sc_2O_3 and its dependence on sintering temperature were discussed. Moreover, STEM-EDS analysis was carried out and combined with a macroscopic model to give a comprehensive understanding about correlations between grain growth and thermal conductivity.

Because SiC ceramics are one of the most promising candidates as cladding materials in nuclear reactors, another focus of the project was the response of SiC ceramics to irradiation damage. Up to the authors' knowledge, Article III adopts protons for the first time to irradiate spark plasma sintered SiC ceramics without sintering additives. Sintering additives were not adopted because they distract the understanding of irradiation effect on SiC and produce high radioactivity after proton irradiation, which significantly increases difficulty of handling materials for experimental work. X-ray diffraction showed the unit cell volume expansion and laser flash technique demonstrated significant thermal conductivity reduction after proton irradiation. Underlying mechanism about volume expansion and thermal conductivity reduction was also discussed. It is mentioned that references of each article will be introduced in the end of each article.

3.2 Article I: Thermal conductivity of spark plasma sintered SiC ceramics with Alumina and Yttria

Contributions:

Zhenfei Chai conducted majority of the experimental work, analyzed experimental results and wrote the article. **Dr. Zhaohe Gao** helped with HADDF-STEM images on SiC ceramics sintered for different holding times (Figure 3.3 and 3.4) . **Dr. Han Liu** and **Dr Xun Zhang** gave some suggestions on the structure of the article. **Dr. Gyorgyi Glodan** helped with the spark plasma sintering experiments. **Prof. Ping Xiao** provided funding for the experimental work, guided the work and gave useful advice on describing experimental results effectively. All authors made efforts on reviewing the article.

The Article I has been published by the Journal of the European Ceramic Society (Volume 41, Issue 6, 2021, Page 3264-3273).

Thermal conductivity of spark plasma sintered SiC ceramics with Alumina and Yttria

Zhenfei Chai[1], Zhaohe Gao[1], Han Liu[1], Xun Zhang[1], Gyorgyi Glodan[2], Ping Xiao[1,*]

[1] *Department of Materials, University of Manchester, Manchester UK, M13 9PL, UK*

[2] *Dalton Cumbrian Facility, University of Manchester, Westlakes Science & Technology Park, Moor Row, Cumbria CA24 3HA, UK*

Abstract: In this study, dense SiC ceramics were fabricated at 1650-1750 °C for 10-60 min by spark plasma sintering (SPS) using 3-10 wt.% Al_2O_3-Y_2O_3 as sintering additives. Effects of sintering temperature, sintering additive content and holding time on microstructure as well as correlations between microstructure and thermal conductivity were investigated. An increase in the sintering temperature promotes grain growth. Extending holding time has little influence on grain size but results in formation of continuous network of sintering additive, which increases interfacial thermal resistance and thus decreases thermal conductivity. For SiC ceramics composed of continuous SiC matrix and discrete secondary phase (yttrium aluminum garnet, YAG), an increase in the sintering additive content results in smaller grain size and lower thermal conductivity. The lower thermal conductivity of the SiC ceramic with higher sintering additive content is mainly due to the smaller grain size rather than the low intrinsic thermal conductivity of YAG.

Key words: SiC; SPS; interfacial thermal resistance; grain size; thermal conductivity.

3.2.1 Introduction

SiC ceramics have very wide applications, such as heat exchangers, nozzles, mechanical seals and protective coating for nuclear fuels due to high thermal conductivity (490 W/(m•K) for single crystal α-SiC), high oxidation resistance, corrosion resistance, low activation under radiation, excellent high temperature mechanical performance and so on [1-6]. Previously reported thermal conductivities of SiC ceramics obtained under different fabrication conditions ranged from 32 W/(m•K) to 490 W/(m•K), suggesting multiple factors can affect heat conduction mechanism and it is necessary to understand the dominant factor(s) controlling heat conduction for specific SiC ceramics [1, 7-9].

Because covalent SiC ceramic has very limited free mobile electrons/holes, phonon is believed to dominate heat conduction. As phonon propagates through SiC ceramics, it can be scattered by different sources (e.g. grain boundaries, point defects, and other phonons), resulting in smaller phonon mean free path and lower thermal conductivity. For example, as grain size of the cubic SiC fabricated by chemical vapor deposition (CVD) technique reduced from 17.2 μm to 6.8 μm, thermal conductivity at 0 °C decreased from 175 W/(m•K) to 90 W/(m•K) [10]. At measurement temperature higher than 300 K, thermal conductivity of SiC ceramics decreased with increasing temperature because more phonons involved in heat conduction at high temperature and phonon-phonon scattering (Umklapp scattering) process became more prominent [11].

It is very difficult to achieve densification of SiC ceramics without using extremely high sintering temperature (over 2100 °C) or pressure because of its high degree of covalence (~88%) and extremely low self-diffusion coefficient [12]. To fabricate dense SiC ceramics at less severe conditions, sintering additives have been extensively developed and could be divided into 2 types in terms of sintering mechanism: liquid phase sintering additive with low melting point (e.g. Al_2O_3-based sintering additive and rare-earth oxide based sintering additive) [13-15] and solid state sintering additive (e.g. B_4C-C and B-C) [16, 17]. Liquid phase sintering additive is more favorable in fabricating dense SiC ceramics due to much higher diffusion rate of atoms in liquid than counterpart in solid. The most popular liquid phase sintering additive system is Al_2O_3-Y_2O_3 for it has not only relatively low eutectic temperature (~1780 °C) but also the capability of obtaining in-situ toughened microstructure [13, 18]. Advanced sintering techniques have also been adopted to sinter dense SiC ceramics [12]. Among those sintering techniques, SPS possessed unique advantages, such as lower sintering temperature, higher heating rate and shorter holding time compared with conventional sintering methods [19-22]. However, there were very limited number of studies which combine SPS and liquid phase sintering additives to densify SiC ceramics [23-25].

The addition of sintering additive not only improves densification of SiC ceramics, but also shows significant effects on thermal conductivity of SiC ceramics via introducing and/or changing scattering sources (e.g. variation of point defects concentration inside SiC grains and introduction of new

interface between sintering additive and SiC). It was shown that during liquid phase sintering process of SiC ceramics with Al_2O_3-based sintering additive, Al_2O_3 could dope into SiC lattice via solution-reprecipitation process and thus lead to formation of point defects (e.g. Si vacancy and substitutional atoms of Al and O) which are effective in scattering high-frequency phonons [26]. As a result, SiC ceramics sintered with Al_2O_3-based sintering additive possess thermal conductivities lower than 120 W/(m•K) [26, 27].

Generally, SiC ceramics with sintering additive show lower thermal conductivity than that of pure SiC ceramics, which can be partially ascribed to low intrinsic thermal conductivity of the sintering additive and formation of new interfaces between SiC and sintering additive [28]. The new interface scatters phonon and thus leads to a temperature discontinuity. Such phonon-interface scattering is described as interfacial thermal resistance (also called as Kapitza resistance) [29]. Malik et al. investigated dependence of thermal conductivity of pressureless sintered SiC ceramics on the content of the sintering additive (Al_2O_3-Y_2O_3-CaO) [30]. It was found that thermal conductivity gradually decreased with increasing sintering additive content, which was attributed to the increased content of the intergranular phase with low thermal conductivity, decreased grain size and the increased phonon scattering by the interface between SiC and the intergranular phase. Also, sintering additive distribution could affect thermal conductivity [31]. The upper limit for the thermal conductivity of a sintered ceramic is obtained when matrix and sintering additive are arranged in a parallel configuration relative to same heat flux due to smallest interface resistance to heat flux. Similarly, the lower limit of the thermal conductivity is achieved when matrix and sintering additive are arranged in a serial configuration.

Although effects of grain size, point defect and sintering additive content/type on thermal conductivity of sintered SiC ceramics have been discussed in previous articles [9, 14, 26, 28], effects of sintering additive distribution and interface between SiC and sintering additive on thermal conductivity are rarely studied. In this study, SiC ceramics with variable grain size, sintering additive distribution and sintering additive contents have been designed and fabricated at 1650-1750 °C by SPS with 3-10 wt.% Al_2O_3-Y_2O_3 as a sintering additive. Furthermore, dependence of thermal conductivity of sintered

SiC ceramic on sintering additive distribution, content and resultant microstructure will be discussed. Our results will further improve the understanding of the heat conduction mechanism for complex sintered ceramics system.

3.2.2 Experimental Methods

3.2.2.1 Sample preparation

The process to fabricate SiC ceramics is described as below: Firstly, the starting powder β-SiC (0.8-1.2 μm, 99%, H. C. Starck) was mixed with different contents of mixture of Al_2O_3 (0.837 μm, α-Al_2O_3, 99.9%, Alfa Aesar) and Y_2O_3 (99.99%, Sigma-Aldrich) for 8 h by wet-milling methods in which ethanol and SiC balls were used as solvent and milling balls respectively. Molar ratio of Al_2O_3 and Y_2O_3 was chosen as 4:1 at which lowest eutectic temperature of ~1780 °C could be reached according to the phase diagram of Al_2O_3 and Y_2O_3 [18].

Then the as-obtained slurries were dried at 90 °C for 24 h followed by manual grinding using agate mortar and pestle. Finally, the powder mixture was loaded into a graphite die with diameter of 12.7 mm and compressed using corresponding graphite punches in an SPS machine (DCS 10-4, Thermal Technology, GT Advanced Technology) with pulsed current (maximum values of voltage and current are 10 V and 4000 A respectively). Graphite foils were adopted in all contact areas of graphite pieces and powders for easy removal of the sintered pellet. Thermopyrometer was used to monitor temperature of a pre-drilled hole of the graphite die which is about 3.15 mm away from the boundary between SiC pellet and graphite die.

Heating/cooling rate, sintering temperature and holding time were selected as 100 °C/min, 1650-1750 °C and 10-60 min respectively. Vacuum atmosphere (around 5 Pa) was used during sintering. Initial uniaxial pressure of 20 MPa was applied to the powder mixture before 600 °C to ensure good electrical contact between electrode and graphite pieces. The pressure was then gradually increased to 60 MPa during which the temperature was increased from 600 °C to 1550 °C, and released to 20 MPa in the end of isothermal period.

3.2.2.2 Characterization

3.2.2.2.1 Density, composition and microstructure

Densities of SiC specimens were measured by Archimedes principle in an analytical balance with the accuracy of 1 mg. Theoretical density was calculated by mixing rules, which is shown in equation 3.1. Two assumptions were made to calculate theoretical density: (1) Al_2O_3 reacts with Y_2O_3 to produce fully crystallized YAG and none of them reacts with SiC during sintering process; (2) there is no evaporation during SPS process. Thus, the theoretical density of SiC using 3-10 wt.% Al_2O_3-Y_2O_3 as a sintering additive is between 3.235 g/cm^3 and 3.294 g/cm^3.

$$\rho = \sum x_i * \rho_i \tag{3.1}$$

Where ρ_i refers to density of phase i and x_i is volume fraction of phase i.

Composition of as-sintered specimens was characterized by XRD using Rigaku D/Max-γB X-ray diffractometer, with Cu Kα radiation (λ = 0.154178 nm). Specimens were firstly cut into two equal parts. Cross sections of specimens were ground by diamond pad with grit size of 35 μm and then successively polished by diamond paste with grit size of 6 μm, 1 μm, and 0.25 μm and silica suspension of 60 nm in diameter. Microstructures of specimens were investigated by Field Emission Gun Scanning Electron Microscopy (FEG-SEM, FEI Quanta 250). The accelerated voltage and spot size were chosen as 15 kV and 3 respectively. SEM images were used to get average intercept size via the line intercept method which was then converted into average grain size based on an assumption that grains have tetrakaidekahedral shape and their sizes follow log-normal distribution [32]. More than 200 grains were measured to get average grain size of sintered SiC ceramics.

Focused ion beam (FIB, FEI Quanta 3D FIB) was used to cut a thin lamella from cross section of sintered SiC ceramics. That lamella was characterized by transmission electron microscopy (TEM, FEI Talos, F200A) equipped with Super-X Energy dispersive X-ray spectroscopy (EDS) system and High angle annular dark field (HAADF) detector. EDS-mapping was carried out in several positions where both grain boundaries and triple junctions were detected. Composition variation across a grain boundary was further shown as a line spectrum via data processing in software Velox.

3.2.2.2.2 Thermal conductivity

Laser flash technique (LFA 427 on 18-414/4, NETZSCH GmbH) was used to measure thermal diffusivity ranging from room temperature to 1000 °C under 1 bar Argon atmosphere. Bottom and top surfaces of as-sintered disk specimens with diameter of 12.7 mm and thickness around 2 mm were ground by diamond pad with grit size of 35 µm to get parallel surfaces. Prior to measurement by LFA, thin graphite coating was sprayed on sample surfaces to maximize heat absorption of bottom surface and thermal radiation of top surface. Laser pulses were applied to the bottom surface of sample and an InSb detector was used to record temperature rise of the top surface. Thermal diffusivity (α) could be calculated according to equation 3.2 [33].

$$\alpha = \frac{0.138 K_1 K_2 d^2}{t_{1/2}} \tag{3.2}$$

Where d is the thickness of the sample, $t_{1/2}$ stands for the time required for the top sample surface to reach half of the maximum temperature rise, K_1 and K_2 refer to coefficient for finite pulse time correction and heat loss correction respectively.

Specific heat (C_p) from 50 °C to 1000 °C under Argon atmosphere was measured by differential scanning calorimetry (DSC-STA449C, NETZSCH GmbH). Finally, thermal conductivities (k) were calculated according to equation 3.3.

$$k = \alpha * C_p * \rho \tag{3.3}$$

Where α is thermal diffusivity, C_ρ and ρ stand for the specific heat and specimen density respectively.

3.2.3 Results

3.2.3.1 Phase composition and microstructure

Table 3. 1 provides information about fabrication conditions and corresponding relative densities/grain size of sintered SiC ceramics using mixture of Al_2O_3-Y_2O_3 as a sintering additive. In Table 3. 1, sintered SiC ceramics are labelled based on fabrication conditions: MI3 and MI10 stand for sintering additive content of 3 wt.% and 10 wt.% respectively; AlY16 and AlY17 stand for the sintering additive (mixture of Al_2O_3-Y_2O_3 with molar ratio of 4:1) at 1650 ºC and 1750 ºC respectively; 10 min and 60 min mean holding time at corresponding target temperatures.

Table 3. 1 Fabrication parameters and relative densities/grain size of spark plasma sintered SiC ceramics using 3-10 wt.% mixture of Al_2O_3-Y_2O_3 (molar ratio of 4:1) as a sintering additive at sintering temperature of 1650-1750 ºC for 10-60 min.

Specimen ID	Sintering additive content (wt.%)	Sintering temperature (ºC)	Holding time (min)	Relative density* (%)	Grain size (μm)
MI3AlY17-10min	3	1750	10	99.8 ± 0.11	1.40 ± 0.20
MI3AlY17-60min	3	1750	60	99.7 ± 0.11	1.51 ± 0.32
MI3AlY16-60min	3	1650	60	99.6 ± 0.39	0.60 ± 0.04
MI10AlY17-10min	10	1750	10	98.5 ± 0.08	0.75 ± 0.31

Notes: (1) * relative density is obtained by dividing measured density over the theoretical density of SiC ceramics and theoretical density is calculated by mixing rule (equation 3.1); (2) SiC ceramics sintered with 3 wt.% mixture of Al_2O_3-Y_2O_3 at 1650 ºC for 10 min is not included in this table due to low relative density (~92.1%).

According to Table 3. 1, when sintering temperature is fixed at 1750 °C, long holding time (60 min) and/or high sintering additive content (10 wt.%) do not significantly change relative density. In contrast, when sintering temperature is 1650 °C, long holding time of 60 min results in high relative density of 99.6% while short holding time of 10 min leads to low relative density (~92.1%). Such difference is suggested to be caused by higher atomic diffusion rate in liquid phase sintering additive and lower viscosity of liquid phase sintering additive at higher sintering temperature [34]. It is also noted that dense SiC ceramics can be obtained at sintering temperature of 1650 °C, which is about 130 °C lower than eutectic temperature (~1780 °C) of the sintering additive (mixture of Al_2O_3-Y_2O_3 with molar ratio of 4:1), which could be attributed to presence of silica on the surface of starting SiC powders. It was reported that the melting point of SiO_2-Al_2O_3-Y_2O_3 could be as low as 1350 °C [9, 35]. Furthermore, higher heating rate of SPS technique (100 °C/min) compared with counterpart of conventional sintering process (<50 °C/min) inhibits possible weight loss of the liquid phase sintering additive [36]. Such low content of sintering additive (3 wt.%) and short holding time (10 min) at 1750 °C are significant for obtaining excellent comprehensive performance of SiC based composites.

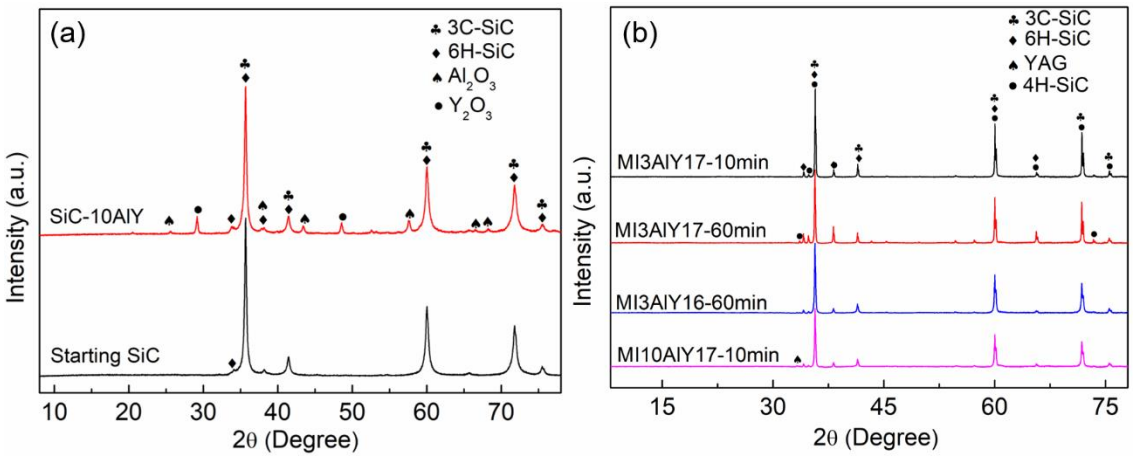

Figure 3. 1 XRD spectra of SiC: (a) starting SiC powders and ball milled SiC powders with 10 wt.% mixture of Al_2O_3-Y_2O_3 (b) spark plasma sintered SiC ceramics. Note MI3 and MI10 mean sintering additive content of 3 wt.% and 10 wt.% respectively; AlY16 and AlY17 stand for the sintering additive of Al_2O_3-Y_2O_3 (molar ratio of 4:1) at sintering temperature 1650 ºC and 1750 ºC respectively; 10 min and 60 min mean holding time at corresponding target temperatures.

Figure 3. 1(a) shows XRD spectra of starting SiC powder and ball-milled SiC powder with 10 wt.% Al_2O_3-Y_2O_3. According to Figure 3. 1(a), there is small amount of 6H-SiC in addition to main phase 3C-SiC (also called as β-SiC) in starting SiC powder. The peak intensity ratio of 3C-SiC and 6H-SiC does not change after ball milling process using SiC balls, implying negligible contamination from ball-milling process.

Figure 3. 1(b) shows XRD spectra of sintered SiC ceramics under different sintering conditions. According to Figure 3. 1(b), YAG is only detected in the SiC ceramic sintered with 10 wt.% Al_2O_3-Y_2O_3 at 1750 ºC for 10 min (labelled as MI10AlY17-10 min) because sintering additive content (3 wt.%) of other SiC ceramics is lower than detectability limit of the XRD. Both β-SiC (3C-SiC) and α-SiC (referred as all SiC polytypes except 3C-SiC) are observed in all SiC ceramics. Moreover, for a fixed sintering temperature and sintering additive content, extending holding time results in more α-SiC (especially more 4H-SiC) and less β-SiC according to the evolution of peak intensity ratio of β-SiC and α-SiC. For a fixed holding time and sintering additive content, increasing sintering temperature promotes the phase transformation from β-SiC to α-SiC. The phase transformation is attributed to thermal stability of SiC. It was reported that β-SiC (3C-SiC) was stable between 1400-1600 °C while some α-SiC (e.g. 4H-SiC, 6H-SiC and 15R-SiC) can co-exist at temperature region of 1600-2600 °C [37]. Also, impurity originating from the fabrication process could affect thermal stability of SiC. It was reported that Al inside SiC lattice was found to stabilize 4H-SiC while N inside SiC lattice was able to stabilize 3C-SiC [38]. Hence, α-SiC is generally more preferred at higher temperature for longer holding time due to higher thermal stability. Furthermore, formation of 4H-SiC in sintered SiC ceramics suggests that Al/Al_2O_3 probably has doped into SiC lattice during sintering process.

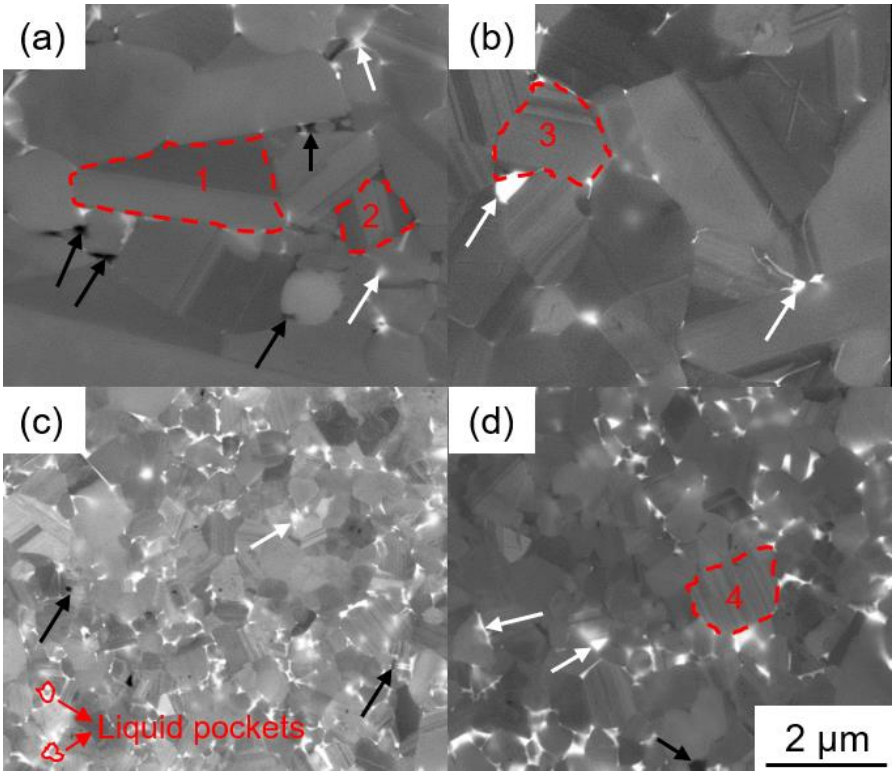

Figure 3. 2 Backscattered Electron (BSE) images of spark plasma sintered SiC ceramics under different sintering additive contents, sintering temperature and holding times: (a) 3 wt.% Al_2O_3-Y_2O_3, 1750 ºC and 10 min, MI3AlY17-10min; (b) 3 wt.% Al_2O_3-Y_2O_3, 1750 ºC and 60 min, MI3AlY17-60min; (c) 3 wt.% Al_2O_3-Y_2O_3, 1650 ºC and 60 min, MI3AlY16-60min; (d) 10 wt.% Al_2O_3-Y_2O_3, 1750 ºC and 10 min, MI10AlY17-10min. All images have the same scale bar. Black and white arrows indicate pores and sintering additive containing large atom (Y) respectively. The red dashed line indicates a grain boundary.

Figure 3. 2 are BSE images of polished cross section of SiC ceramics under different sintering conditions. Black contrast marked by a black arrow and white contrast marked by a white arrow correspond to a pore and sintering additive containing large atoms (Y) respectively. Grey contrast surrounded by a red dashed line is a SiC grain. Grain 1 and 2 are typical composite grains consisting of elongated α-SiC (grey contrast) and β-SiC cap with random shapes (dark grey contrast) [39, 40]. Grain 3 and 4 contain several parallel lines with grey/dark grey contrast. The lines are possibly correlated with twin bands (also called as growth fault) whose largest width locates next to the grain boundaries of the recrystallized β-SiC envelopes and smallest width locates at the coherent β/α interface [39]. These twin bands in β-SiC grains were believed to be nucleation sites for α-SiC [39].

The twins were suggested to form during the rapid recrystallization of β-SiC and also the growth of recrystallized β-SiC envelope. The recrystallization of β-SiC was achieved by epitaxial growth on the {111} crystal planes, which is driven by the reduction of free energy because the interfacial energy of the interface between $\{111\}_{\beta\text{-SiC}}$ and $\{0001\}_{\alpha\text{-SiC}}$ is much lower than counterparts of other random β/α-SiC interface. During the growth of recrystallized β-SiC envelope, twinning is achieved by the glide of Shockley partial dislocations so that the stacking sequence of cubic SiC changes from ABCABC… to ACBACB… [39]. High-resolution transmission electron microscopy (HRTEM) has verified that the twin boundary was mainly composed of a pile up of different Shockley partial dislocations [41]. Driving force for the twinning process originates from the thermal stability difference between β-SiC and α-SiC [42]. The elongated morphology of α-SiC is also attributed to much lower interfacial energy of the coherent interface between α-SiC and β-SiC [43]. Presence of the composite grains further verifies that phase transformation from β-SiC to α-SiC takes place during liquid phase sintering process. Pores mainly distributes in multi-grain junctions, which could be caused by evaporation of liquid sintering additive at high temperature (pores with rounded/faceted interface) or insufficient sintering (irregular pores with significantly different curvature) [44]. These pores are detrimental to heat conduction due to its intrinsically low thermal conductivity. Sintering additive containing large atom (Y) mainly locates in triple junctions although some relative thin sintering additive film can be found in grain boundaries. In addition, liquid phase sintering of SiC ceramics using 3 wt.% Al_2O_3-Y_2O_3 as a sintering additive is achieved even at 1650 °C (130 °C lower than the eutectic temperature), which is verified by the impregnation of small grains in liquid phase pockets marked by the solid line in Figure 3. 2.

Grain sizes of all sintered SiC ceramics were obtained based on their respective BSE images (Figure 3. 2) and summarized in Table 3. 1. According to Table 3. 1, as sintering temperature and sintering additive content are constant (comparison between sample MI3AlY17-10min and MI3AlY17-60min), extending holding time from 10 min to 60 min results in slight grain growth (from 1.40 $\pm$ 0.20 μm to 1.51 $\pm$ 0.32 μm). In contrast, as sintering additive content and holding time keep constant (comparison between sample MI3AlY17-60min and MI3AlY16-60min), increasing sintering temperature from 1650 °C to 1750 °C results in obvious grain growth (from 0.60 $\pm$ 0.04 μm to 1.51

± 0.32 μm). The results indicate that increasing sintering temperature promotes grain growth more effectively than extending holding time. In addition, as sintering temperature and holding time are constant (comparison between sample MI3AlY17-10min and MI10AlY17-10min), increasing sintering additive content from 3 wt.% to 10 wt.% inhibits grain growth significantly (from 1.40 ± 0.20 μm to 0.75 ± 0.31 μm).

In general, grain growth during liquid phase sintering process is mainly achieved via dissolution-reprecipitation mechanism: firstly, small grains preferably dissolve into the liquid due to higher solubility than that of large grains; secondly, the resultant local chemical potential gradient drives the diffusion of dissolved atom to neighboring sites of large grains; thirdly, matrix atoms in the liquid precipitates on large grains [44]. Hence, grain growth is controlled by either diffusion process or dissolution/reprecipitation process. Despite which process controls grain growth, higher sintering temperature is expected to increase atomic diffusion rate, decrease liquid viscosity and perhaps enhance dissolution/reprecipitation process. As a result, increasing sintering temperature promotes grain growth, which is consistent with our result when comparing MI3AlY17-60min with MI3AlY16-60min. In addition, it is still necessary to figure out rate-controlling process for grain growth. Given that the average diffusion length is shorter when lower content of sintering additive is used, larger grain size is expected for samples with lower content of sintering additive, which is consistent with comparison result between sample MI10AlY17-10min and MI3AlY17-10min. Therefore, it could be speculated that the atom diffusion process dominates grain growth at the sintering temperature of 1750 °C, which is consistent with previous study [45].

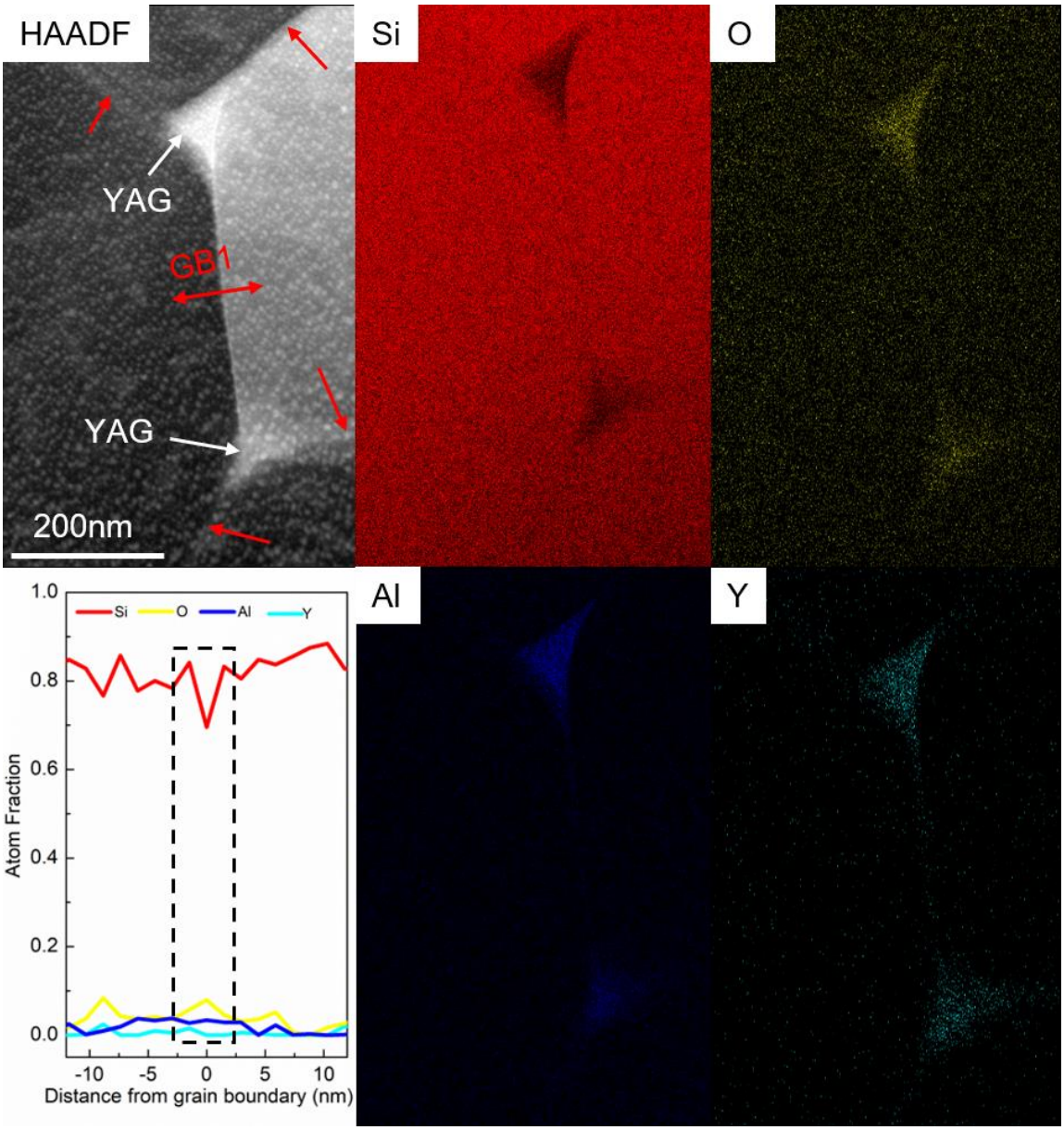

Figure 3. 3 HAADF images and EDS analysis of sample MI3AlY17-10min sintered by SPS under below condition: 3 wt.% mixture of Al_2O_3-Y_2O_3, sintering temperature of 1750 ºC and holding time of 10 min. Red and white arrows are grain boundary and secondary phase of YAG respectively. Composition variation along the red double arrow crossing grain boundary 1 (GB1) is determined by EDS and shown in the bottom left spectrum. Step size is 0.7 nm.

To examine the sintering additive distribution in sintered SiC ceramics, HAADF and STEM-EDS were used to characterize sample MI3AlY17-10min and MI3AlY17-60min. Contrast in HAADF images is determined by the amount of Rutherford scattered electrons with very high scattering angles.

Elements with higher atomic numbers can scatter more electrons at higher angles and thus appear brighter in HAADF images. Figure 3. 3 demonstrates HAADF image (the top left image) of the SiC ceramic sintered with 3 wt.% Al_2O_3-Y_2O_3 at 1750 ºC for 10 min (labelled as MI3AlY17-10min). White contrast marked by a white arrow corresponds to sintering additive containing large atom (Y). A red arrow indicates a grain boundary. No white contrast in grain boundaries can be observed in this HAADF image. EDS-mapping results (the right images) show that Y, Al and O are segregated in the triple junction. Moreover, EDS-line spectrum (the bottom left image) along grain boundary 1 (GB1) marked with a red double arrow in HAADF image shows there is not any element segregation in this grain boundary. Other 10 grain boundaries in different positions of sample MI3AlY17-10min have also been examined and similar phenomena have been confirmed. Overall, as short holding time of 10 min is used, neither element segregation nor secondary phase in grain boundaries can be detected. In other words, the sintered SiC ceramic is composed of continuous SiC matrix and discrete secondary phase when short holding time of 10 min is used.

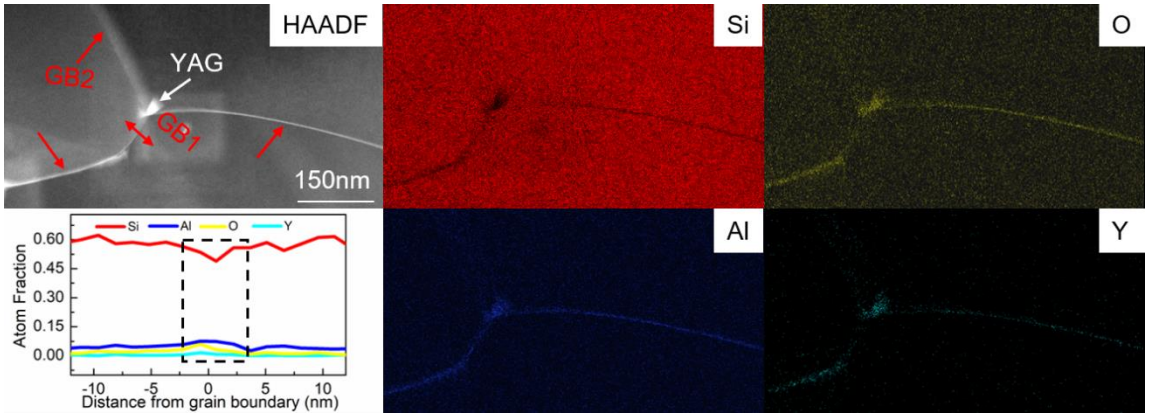

Figure 3. 4 HAADF images and EDS analysis of sample MI3AlY17-60min sintered by SPS under below condition: 3 wt.% mixture of Al_2O_3-Y_2O_3, sintering temperature of 1750 ºC and holding time of 60 min. Red arrow and white arrow are grain boundary and secondary phase of YAG respectively. White contrast in grain boundary indicates presence of sintering additives. Composition variation along the red double arrow line crossing grain boundary 1 (GB1) is determined by EDS and shown in the bottom left spectrum. Step size is 0.7 nm.

Figure 3. 4 shows the HAADF image (the top left image) of the SiC ceramic sintered with 3 wt.% Al_2O_3-Y_2O_3 at 1750 ºC for 60 min (labelled as MI3AlY17-60min). According to the HAADF image,

sintering additive containing Y distributes not only in the triple junction but also in grain boundaries marked by red arrow line. EDS-mapping results (the right images) also verify the sintering additive distribution. EDS-line spectrum (the bottom left) across this grain boundary (GB1) clearly indicates that the atom fraction of Si in this grain boundary is lower than the counterpart inside SiC grains while atom fractions of O, Al and Y show opposite trend. 6 more grain boundaries in different positions have also been examined and similar phenomena have been confirmed. Overall, as holding time is increased to 60 min, sintering additive distributes in both grain boundary and triple junctions, suggesting that a continuous network of sintering additive has formed.

3.2.3.2 Thermal conductivity

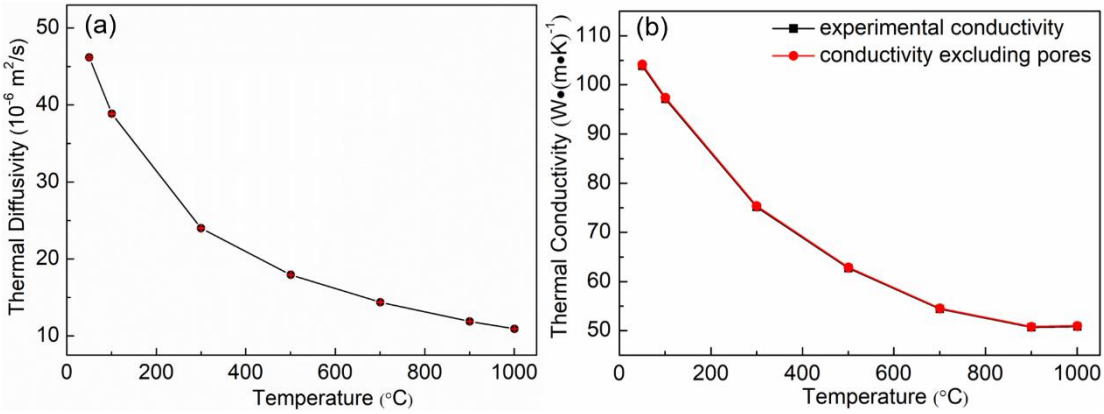

Figure 3. 5 Thermal properties of the SiC ceramic sintered with 3 wt.% Al_2O_3-Y_2O_3 at 1750 ºC for 10 min (MI3AlY17-10min) versus measurement temperature: (a) thermal diffusivity; (b) thermal conductivity. Red line in Figure 3. 5(b) are thermal conductivities of 'fully dense' SiC ceramics calculated according to experimentally measured thermal conductivity and equation 3.4. Error bar of conductivity is smaller than the symbol size if they are not shown.

Figure 3. 5(a) shows effects of measurement temperature on thermal diffusivity of the SiC ceramic sintered with 3 wt.% Al_2O_3-Y_2O_3 at 1750 ºC for 10 min (labeled as MI3AlY17-10min). Thermal diffusivity decreases monotonically with increasing measurement temperature. Thermal conductivity of the SiC ceramic was obtained according to equation 3.3 and shown in Figure 3. 5(b). The black line demonstrates experimental thermal conductivity of MI3AlY17-10min while the red line gives derived thermal conductivity of 'fully dense' MI3AlY17-10min. The thermal conductivity of fully dense

ceramics is calculated via Maxwell model and experimental thermal conductivity. The Maxwell model describes thermal conductivity of the composite consisting of a continuous matrix and diluted secondary phase, which is suitable for sintered ceramics in this study which have small amount of isolated pores (secondary phase) randomly distributed in continuous SiC matrix (Figure 3. 2). Equation 3.4 is specially derived from the Maxwell model in which thermal conductivity of pore is assumed to be 0 [29, 46].

$$k_s = k_f \frac{1-V_p}{1+0.5V_p} \quad (3.4)$$

Where k_f and k_s are thermal conductivity of a fully dense ceramic and a sintered ceramic respectively, while V_p stands for porosity of sintered ceramics.

According to Figure 3. 5(b), experimental thermal conductivity is very close to calculated thermal conductivity of fully dense SiC ceramic, suggesting that pores have negligible effects on heat conduction in this study. Also, thermal conductivity decreases with increasing measurement temperature, indicating phonon-phonon scattering (i.e. Umklapp scattering) process is main mechanism controlling heat conduction [11]. Highest thermal conductivity of 104 $\pm$ 0.36 W/(m•K) is obtained at measurement temperature of 50 °C, which is higher than counterpart (71 W/(m•K)) of the SiC ceramic sintered with higher content of Al_2O_3-Y_2O_3 [26].

Table 3. 2 shows thermal properties at 50 °C of SiC ceramics fabricated under different sintering conditions. The above mentioned Maxwell model was also used to derive thermal conductivity of 'fully dense' ceramics. The small difference between experimentally measured thermal conductivity and derived thermal conductivity again indicates that pores have negligible effects on heat conduction in this study. To exclude porosity effects, thermal conductivity of fully dense SiC ceramics are correlated with microstructure, sintering additive content and distribution in the following discussion. According to Table 3. 2, thermal conductivity at 50 °C of fully dense SiC ceramics in this study varies from 68.6 $\pm$ 0.17 W/(m•K) to 104 $\pm$ 0.54 W/(m•K), which is similar to other reports [26, 47]. When comparing 3AlY17-60min with 3AlY16-60min, the former sample has larger grain size (1.51 $\pm$ 0.32 μm versus 0.60 $\pm$ 0.04 μm, Table 3. 1) and higher thermal conductivity (96.6 $\pm$ 0.42 W/(m•K) versus 74.8 $\pm$ 0.21 W/(m•K), Table 3. 2), suggesting positive role of grain growth in

enhancing thermal conductivity. More interestingly, when comparing 3AlY17-10min with 3AlY17-60min, the former sample has slightly smaller grain size (1.40 ± 0.20 μm versus 1.51 ± 0.32 μm, Table 3. 1) but higher thermal conductivity (104 ± 0.54 W/(m•K) versus 96.6 ± 0.42 W/(m•K), Table 3. 2). In addition, the lowest thermal conductivity of 68.6 ± 0.17 W/(m•K) is observed in the SiC ceramic sintered with 10 wt.% Al_2O_3-Y_2O_3 at 1750 °C for 10 min (MI10AlY17-10min), implying an effective role of sintering additive in decreasing thermal conductivity.

Table 3. 2 Specific heat, thermal diffusivity and thermal conductivity of spark plasma sintered SiC ceramics at the measurement temperature of 50 °C.

Specimen ID	Thermal diffusivity (10^{-6} m^2/s)	Specific heat (J/(g•K))	Conductivity of sintered SiC* (W/(m•K))	Conductivity of fully dense SiC** (W/(m•K))
MI3AlY17-10min	46.2 ± 0.15	0.697	104 ± 0.36	104 ± 0.54
MI3AlY17-60min	42.2 ± 0.12	0.707	96.2 ± 0.28	96.6 ± 0.42
MI3AlY16-60min	34.1 ± 0.04	0.677	74.3 ± 0.31	74.8 ± 0.21
MI10AlY17-10min	30.9 ± 0.05	0.668	67.1 ± 0.12	68.6 ± 0.17

Note: (1) * Thermal conductivities of sintered SiC ceramics were measured at 50 °C; (2) ** Conductivity of fully dense SiC ceramics is calculated using equation 3.4 and the experimentally measured thermal conductivity at 50 °C.

3.2.4 Discussion

The results outlined above indicate that increasing sintering additive content from 3 wt.% to 10 wt.% (comparison between MI3AlY17-10min and MI10AlY17-10min) leads to decreasing grain size and lower thermal conductivity. Furthermore, extending holding time from 10 min to 60 min (comparison between MI3AlY17-10min and MI3AlY17-60min) results in formation of continuous network of sintering additive and lower thermal conductivity, suggesting non-negligible contribution of the

interface between sintering additive and SiC to thermal conductivity of sintered SiC ceramics. The following discussion aims to clarify possible contribution of above mentioned factors (grain size, sintering additive content and distribution) to thermal conductivity.

3.2.4.1 Evolution of sintering additive distribution

As shown in Figure 3. 3 and Figure 3. 4, sintering additive is mainly found in triple junctions in the SiC ceramic sintered for short holding time of 10 min (MI3AlY17-10min) while sintering additive is detected in triple junctions and grain boundaries of the SiC ceramic sintered for long holding time of 60 min (MI3AlY17-60min). Sintering additive distributing in grain boundary of SiC ceramics is also called as intergranular film and has been reported by multiple researchers [48, 49]. Volz et al. have fabricated SiC ceramics at 1800 °C and 1950 °C for 30 min with 10 vol.% Al_2O_3-Y_2O_3 as a sintering additive and only detected amorphous intergranular film in SiC sintered at 1800 °C [48]. Absence of intergranular film at high sintering temperature (1950 °C) was attributed to reduced impurity content in liquid phase and accelerated decomposition reaction between SiC and SiO_2 [48]. However, such explanation is not applicable to sintered SiC ceramics in this study due to lower sintering temperature (1750 °C). Intergranular film was also found in the SiC ceramic sintered with same type sintering additive (mixture of Al_2O_3-Y_2O_3) at 1850 °C for 30 min [49]. Presence of the intergranular film in SiC ceramics sintered with mixture of Al_2O_3-Y_2O_3 at sintering temperature lower than 1850 °C for long holding time ($\geq$ 30 min) indicates that the grain boundary energy is higher than the energy of the interface between the intergranular film and SiC. In terms of reducing the total energy of sintered SiC ceramics, it is inevitable that the liquid sintering additive (mixture of Al_2O_3-Y_2O_3) penetrates the grain boundary to form continuous network of sintering additive.

The rate of liquid sintering additive penetrating the grain boundary was previously reported to be determined by contact angle, viscosity, and reactivity of the liquid [50]. Both high contact angle and high viscosity lead to lower penetration rate. It was reported that contact angle and viscosity of the liquid sintering additive (mixture of Al_2O_3-Y_2O_3) in SiC substrate increased with decreasing temperature [18]. Thus, it is expected that penetration rate is lower in the sintered SiC ceramics (MI3AlY17-10min and MI3AlY17-60min) due to lower sintering temperature (1750 °C) in this study

compared with counterparts previously reported by other researchers [48, 49]. Kinetics of liquid penetrating grain boundary is further reduced due to the high heating rate (100 °C/min) adopted in the SPS process. Hence, the variation of sintering additive distribution with holding time is suggested to be caused by low sintering temperature and high heating rate adopted in this study.

3.2.4.2 Effects of sintering additive distribution

The lower thermal conductivity of the SiC ceramic sintered for 60 min (MI3AlY17-60min) compared with that of the SiC ceramic sintered for 10 min (MI3AlY17-10min) is suggested to be caused by their difference in sintering additive distribution. Firstly, these 2 SiC ceramics have the same sintering additive content and similar grain size (Table 3. 1). Secondly, increasing holding time promotes phase transformation from β-SiC to α-SiC (Figure 3. 1(b)), which should result in higher thermal conductivity because thermal conductivity (490 W/(m•K)) of single crystal α-SiC is higher than that (320 W/(m•K)) of single crystal β-SiC [1, 11]. However, thermal conductivity of MI3AlY17-60min with higher fraction of α-SiC is lower than that of MI3AlY17-10min. Most importantly, MI3AlY17-60min possess continuous network of sintering additive while MI3AlY17-10min has continuous SiC matrix (Figure 3. 3 and Figure 3. 4). In other words, the grains of the SiC matrix in MI3AlY17-60min is wetted by the very thin intergranular film containing Al, Y, O, Si and C (Figure 3. 4).

Both the grain boundary and the interface between the intergranular film and SiC can scatter phonons and lead to a temperature discontinuity on the grain boundary/interface [51, 52]. Phonon-grain boundary scattering and phonon-interface scattering are described by grain boundary thermal resistance and interfacial thermal resistance respectively. It was reported that thermal resistance of the interface between SiC and the glass phase containing Al, Y, O, Si and C was around 8.87×10^{-9} $W^{-1}•m^2•K$ [51], which is higher than the reported grain boundary thermal resistance (4.88×10^{-10} $W^{-1}•m^2•K$) of polycrystalline SiC without any sintering additive [52]. In conclusion, formation of continuous network of sintering additives leads to increase of interfacial thermal resistance and thus decreases thermal conductivity from 104 ± 0.54 W/(m•K) for MI3AlY17-10min to 96.6 ± 0.42 W/(m•K) for MI3AlY17-60min.

3.2.4.3 Effects of sintering additive content

In this study, the sintering additive (mixture of Al_2O_3-Y_2O_3) is mainly present as discrete secondary phase (YAG) located in triple junctions of the SiC ceramics (Figure 3. 1(b) and Figure 3. 3) sintered for short holding time. In the following discussion, SiC ceramics sintered for short holding time of 10 min (i.e. MI3AlY17-10min and MI10AlY17-10min) are simply regarded to be composed of continuous SiC matrix and discrete YAG. To evaluate effects of YAG content on thermal conductivity of those 2 sintered SiC ceramics, a macroscopic model determining thermal conductivity of the composite consisting of continuous matrix and diluted secondary phase is adopted. Equation 3.5 gives the mathematical form of the model [53]. It is noted that interfacial thermal resistance is included in the model because the interface between YAG and SiC can scatter phonons and leads to thermal conductivity reduction.

$$k_e = k_1 \frac{[2(\frac{k_2}{k_1}-\frac{k_2}{ah_c}-1)v_2+\frac{k_2}{k_1}+\frac{2k_2}{ah_c}+2]}{\left[\left(1-\frac{k_2}{k_1}+\frac{k_2}{ah_c}\right)v_2+\frac{k_2}{k_1}+\frac{2k_2}{ah_c}+2\right]} \quad (3.5)$$

Where h_c is interfacial thermal conductance (reciprocal of interfacial thermal resistance), v_2 and a are volume fraction and radius of discrete secondary phase respectively. k_e is the effective thermal conductivity of the composite. k_1 and k_2 stand for thermal conductivity of continuous phase and discrete secondary phase respectively.

When using the macroscopic model (equation 3.5), one firstly needs to know the thermal conductance (reciprocal of thermal resistance) of the interface between SiC and YAG. Interfacial thermal resistance has 2 sources: One source of interfacial thermal resistance, thermal contact resistance, may be caused by poor mechanical/chemical bonding or cracks resulting from mismatch between thermal expansion coefficient of the ceramic matrix and the secondary phase [54]. Thermal contact resistance is negligible for those 2 sintered SiC ceramics in this study due to the absence of cracks in the interface between SiC and YAG and the small difference of linear thermal expansion coefficient (4.7 X 10^{-6} K^{-1} versus 8.9 X 10^{-6} K^{-1}) [55, 56]. The other source of interfacial thermal resistance, thermal boundary resistance, is caused by the mismatch of the acoustic impedance (product of mass density and phonon group velocity) according to the Acoustic Mismatch Model

(AMM) [57]. In the AMM model, phonons which are considered as plane waves propagate through materials that are regarded as continua without lattice and then incident on an interface. It is also assumed that phonons are not scattered on the interface. Instead, phonons incident on the interface can specularly reflect, refract, or convert from longitudinal to transverse (or from transverse to longitudinal) mode [57]. Thus, incidence of phonons on an interface complies with Snell's law and transmission probability is determined by the incident angle and the mismatch between the acoustic impedances of 2 materials. Based on these assumptions, equation 3.6-3.9 were proposed to calculate thermal boundary conductance (reciprocal of thermal boundary resistance) [57, 58].

$$h_c = \frac{1}{4} * v_1 * C_{\rho 1} * \rho_1 * \Gamma_1 \tag{3.6}$$

$$\Gamma_1 = \int_0^{\theta c} \alpha_1 * cos\theta * sin\theta d\theta = \frac{1}{2} * \alpha_1 * (sin\theta_c)^2 \tag{3.7}$$

$$\alpha_1 = \frac{4Z_1 * Z_2}{(Z_1 + Z_2)^2} \tag{3.8}$$

$$sin\theta_c = \frac{v_1}{v_2} \tag{3.9}$$

Where phonons were assumed to incident from material 1 with lower phonon group velocity, h_c is thermal boundary conductance (reciprocal of thermal boundary resistance), Γ_1 is defined as averaged transmission probability of phonons from material 1 and v_2 is defined as phonon group velocity of material 2. In addition, $C_{\rho 1}$, v_1, and ρ_1 are specific heat, phonon group velocity, and mass density of material 1 respectively. Z_1 and Z_2 are acoustic impedances ($Z = \rho * v$) of material 1 and material 2 separated by an interface respectively.

The phonon group velocity was calculated based on Debye approximation in which phonon dispersion was neglected and only acoustic phonons have been considered due to their larger velocity compared with counterpart of optical phonons [59]. Under that assumption, phonon group velocity v is equivalent to the average sound velocity (velocity of acoustic phonon) and can be calculated using equation 3.10 [60].

$$v = 3^{\frac{1}{3}} \left(\frac{1}{v_l^3} + \frac{2}{v_t^3} \right)^{-\frac{1}{3}} \tag{3.10}$$

Where v_l and v_t are the velocity of longitudinal acoustic phonon and transverse acoustic phonon respectively. In this study, 11820 m/s (v_l) and 7520 m/s (v_t) are selected to calculate the phonon

group velocity of SiC based on equation 3.10 [61]. Similarly, 8615 m/s (v_l) and 5000 m/s (v_t) are selected to calculate the phonon group velocity of YAG based on equation 3.10 [62]. The calculated phonon group velocities of YAG and SiC and other parameters required for calculating thermal boundary conductance based on AMM model are listed in Table 3. 3.

Table 3. 3 Parameters for calculating thermal boundary conductance (reciprocal of thermal boundary resistance) of the interface between SiC and YAG based on AMM model.

Specimens	Phonon group velocity* (m/s)	Specific heat** (J/(g•K))	Density (g/cm^3)	Thermal boundary conductance ($W•m^{-2}•K^{-1}$)
YAG	5548	0.59	4.55	8.38×10^8 (AMM)
SiC	8268	0.677	3.21	

Note: (1) * Phonon group velocity is equivalent to average sound velocity and calculated using equation 3.10. Sound velocities of SiC and YAG are obtained from reference [61] and [62] respectively. (2) ** Specific heats for YAG and SiC are obtained from reference [63] and [11] respectively.

Except interfacial thermal conductance, one needs to know thermal conductivity and radius of discrete YAG located in triple junctions of the sintered SiC ceramics when using equation 3.5. The thermal conductivity of YAG is chosen as 8 W/(m•K) [64]. The radius of YAG in sintered SiC ceramics was obtained from corresponding SEM images, which is 165 $\pm$ 80 nm for SiC with 3 wt.% sintering additive (MI3AlY17-10min) and 100 $\pm$ 29 nm for SiC with 10 wt.% sintering additive (MI10AlY17-10min). With these values and equation 3.5, thermal conductivity of continuous SiC matrix could be obtained and is shown in Table 3. 4.

Table 3. 4 Comparison between thermal conductivities of continuous SiC matrix and SiC ceramics containing different contents of discrete secondary phase (YAG).

Specimen ID	Content of YAG (wt.%)*	Conductivity of SiC ceramics** (W/(m•K))	Derived Conductivity of SiC matrix*** (W/(m•K))	Grain size of SiC (μm)
MI3AlY17-10min	3	104	107	1.40
MI10AlY17-10min	10	68.6	75.9	0.75

Note: (1) * Considering the sintering additive (mixture of Al_2O_3-Y_2O_3) is present as discrete phase of YAG in these 2 sintered SiC ceramics, content of YAG is assumed to equal to the sintering additive content. (2) ** Conductivity of SiC ceramics is the thermal conductivity of 'fully dense' SiC ceramics calculated using equation 3.4 to remove the effect of porosity on the experimentally measured thermal conductivity. (3) *** Thermal conductivity of SiC matrix is derived according to equation 3.5 in which h_c is 8.38 X 10^8 W•m^{-2}•K^{-1} calculated by AMM model, radius of YAG is obtained from SEM images and thermal conductivity of YAG (k_2) is obtained from reference [64].

It should be noted that the continuum approximation adopted in the AMM model might be strictly accurate at low temperature (below 30 K) at which the wavelength of dominant phonons is much larger than interatomic distances [57]. The assumption about the ignorance of scattering process might not be appropriate for heat conduction at high temperature at which both phonon-phonon scattering and the phonon scattering by atomic disorders on the interface becomes pronounced. Thus, thermal boundary conductance calculated by the AMM model is overestimated at the currently investigated measurement temperature (323 K). However, such overestimation is suggested to have

negligible effects on following discussion about grain size effects on thermal conductivity because the overestimation is expected very small.

Table 3. 4 shows that the thermal conductivity of the SiC ceramic with 10 wt.% YAG is about 34% lower than that of the SiC ceramic with 3 wt.% YAG, which is due to combination of smaller grain size and higher content of YAG with low intrinsic thermal conductivity (8 W/(m•K)). Firstly, when comparing the experimentally measured grain size and the derived thermal conductivity of SiC matrix listed in Table 3. 4, it can be found that decreasing grain size from 1.40 ± 0.20 μm to 0.75 ± 0.31 μm results in around 29% decrease of thermal conductivity from 107 W/(m•K) to 75.9 W/(m•K), which accounts for 85% of total thermal conductivity decrease extent (34%). Secondly, when comparing thermal conductivity of SiC ceramics with that of corresponding SiC matrix, it can be found that 3 wt.% YAG leads to 2.80% decrease of thermal conductivity (from 107 W/(m•K) to 104 W/(m•K)) and 10 wt.% YAG leads to 9.62% decrease of thermal conductivity (from 75.9 W/(m•K) to 68.6 W/(m•K)). Thirdly, the sintering additive (Al_2O_3) could dope into SiC lattice during liquid phase sintering process (as shown in the EDS line spectrum of Figure 3. 3 and Figure 3. 4), resulting in formation of point defects (e.g. Si vacancy and substitutional atoms of Al and O) inside SiC lattice [26]. It is suggested that the same saturated doping of Al_2O_3 into SiC lattice is achieved in all sintered SiC ceramics in this study because more than 1.92 wt.% Al_2O_3 is adopted as raw sintering additive, which is much higher than the solubility limit (0.4 wt.%) of Al_2O_3 in SiC lattice [27]. Hence, the effects of point defects on thermal conductivity are equivalent for the sintered SiC ceramics with different grain size and YAG content.

In conclusion, lower thermal conductivity of the SiC with higher sintering additive content (MI10AlY17-10min) is mainly caused by the smaller grain size rather than the low intrinsic thermal conductivity of YAG. More specifically, decreasing grain size from 1.40 ± 0.20 μm to 0.75 ± 0.31 μm is responsible for 85% of total thermal conductivity decrease while the remaining 15% of total thermal conductivity decrease is caused by the additional 7 wt.% sintering additive.

3.2.5 Conclusions

Highly dense SiC ceramics were fabricated at 1650-1750 °C for 10-60 min by SPS using 3-10 wt.% Al_2O_3-Y_2O_3 as a sintering additive. Thermal conductivity varied from 68.6 ± 0.17 W/(m•K) to 104 ± 0.54 W/(m•K). Effects of sintering temperature, sintering additive content and holding time on microstructure as well as correlations between microstructure and thermal conductivity have been investigated and conclusion can be achieved as follows:

(1) Increasing sintering temperature promotes grain growth while increasing sintering additive content inhibits grain growth. Extending holding time from 10 min to 60 min has little influence on grain size but results in formation of continuous network of sintering additive, as confirmed by HAADF and STEM-EDS results. Presence of the continuous network of sintering additive is suggested to increase the interfacial thermal resistance and decreases thermal conductivity from 104 ± 0.54 W/(m•K) to 96.6 ± 0.42 W/(m•K).

(2) For SiC ceramics composed of continuous SiC matrix and discrete secondary phase (YAG), increasing sintering additive content from 3 wt.% to 10 wt.% results in 34% decrease of thermal conductivity (from 104 ± 0.54 W/(m•K) to 68.6 ± 0.17 W/(m•K)). Lower thermal conductivity of the SiC ceramic with higher sintering additive content is due to combination of smaller grain size and low intrinsic thermal conductivity of YAG. Hasselman and Johnson model were combined with experimental data to evaluate the importance of sintering additive content and grain size in influencing thermal conductivity. Results showed that grain size reduction is responsible for 85% of total thermal conductivity decrease while the remaining 15% of the total thermal conductivity decrease is caused by the additional 7 wt.% sintering additive with low intrinsic thermal conductivity. The results suggest that grain size is an important factor controlling thermal conductivity.

Acknowledgement

The authors would like to thank Dr. John Warren and Mr. Gary Harrison for their kind assistance on XRD experiments. Prof. Ping Xiao would like to acknowledge support from Royal Academy of Engineering and Rolls-Royce for appointment of Rolls-Royce/Royal Academy of Engineering Research Chair in Advanced Coating Technology. Zhenfei Chai is grateful for the funding provided

by the China Scholarship Council. The authors acknowledge the infrastructural support of the Electron Microscopy Centre in the University of Manchester.

References

[1] G.A. Slack, Nonmetallic crystals with high thermal conductivity, Journal of Physics and Chemistry of Solids 34(2) (1973) 321-335.

[2] P.A. Mouche, K.A. Terrani, Steam pressure and velocity effects on high temperature silicon carbide oxidation, Journal of the American Ceramic Society 103(3) (2020) 2062-2075.

[3] K.A. Terrani, Accident tolerant fuel cladding development: Promise, status, and challenges, Journal of Nuclear Materials 501 (2018) 13-30.

[4] R. Krishnarao, M.Z. Alam, D. Das, In-situ formation of SiC, ZrB_2-SiC and ZrB_2-SiC-B_4C-YAG coatings for high temperature oxidation protection of C/C composites, Corrosion Science 141 (2018) 72-80.

[5] Y.-W. Kim, S.H. Jang, T. Nishimura, S.-Y. Choi, S.-D. Kim, Microstructure and high-temperature strength of silicon carbide with 2000 ppm yttria, Journal of the European Ceramic Society 37(15) (2017) 4449-4455.

[6] X. Duan, H. Zheng, Y. Chen, F. Qian, G. Liu, X. Wang, Y. Si, Study on the corrosion resistance of cordierite-mullite and SiC refractories to Li-ion ternary cathode materials, Ceramics International 46(3) (2020) 2829-2835.

[7] K. Watari, H. Nakano, K. Sato, K. Urabe, K. Ishizaki, S. Cao, K. Mori, Effect of grain boundaries on thermal conductivity of silicon carbide ceramic at 5 to 1300 K, Journal of the American Ceramic Society 86(10) (2003) 1812-1814.

[8] T. Sakai, T. Aikawa, Phase Transformation and Thermal Conductivity of Hot-Pressed Silicon Carbide Containing Alumina and Carbon, Journal of the American Ceramic Society 71(1) (1988) C-7-C-9.

[9] J.H. Eom, Y.K. Seo, Y.W. Kim, Mechanical and thermal properties of pressureless sintered silicon carbide ceramics with alumina–yttria–calcia, Journal of the American Ceramic Society 99(5) (2016) 1735-1741.

[10] A. Collins, M.A. Pickering, R.L. Taylor, Grain size dependence of the thermal conductivity of polycrystalline chemical vapor deposited β-SiC at low temperatures, Journal of applied physics 68(12) (1990) 6510-6512.

[11] L.L. Snead, T. Nozawa, Y. Katoh, T.-S. Byun, S. Kondo, D.A. Petti, Handbook of SiC properties for fuel performance modeling, Journal of nuclear materials 371(1-3) (2007) 329-377.

[12] K. Raju, D.-H. Yoon, Sintering additives for SiC based on the reactivity: a review, Ceramics International 42(16) (2016) 17947-17962.

[13] N.P. Padture, In situ-toughened silicon carbide, Journal of the American Ceramic Society 77(2) (1994) 519-523.

[14] S.H. Jang, Y.W. Kim, K.J. Kim, S.J. Lee, K.Y. Lim, Effects of Y_2O_3–RE_2O_3 (RE= Sm, Gd, Lu) Additives on Electrical and Thermal Properties of Silicon Carbide Ceramics, Journal of the American Ceramic Society 99(1) (2016) 265-272.

[15] T.-Y. Cho, Y.-W. Kim, Effect of grain growth on the thermal conductivity of liquid-phase sintered silicon carbide ceramics, Journal of the European Ceramic Society 37(11) (2017) 3475-3481.

[16] G. Magnani, G. Sico, A. Brentari, P. Fabbri, Solid-state pressureless sintering of silicon carbide below 2000° C, Journal of the European Ceramic Society 34(15) (2014) 4095-4098.

[17] G. Magnani, A. Brentari, E. Burresi, G. Raiteri, Pressureless sintered silicon carbide with enhanced mechanical properties obtained by the two-step sintering method, Ceramics International 40(1) (2014) 1759-1763.

[18] S. Taguchi, F. Motta, R. Balestra, S. Ribeiro, Wetting behaviour of SiC ceramics: part II—Y_2O_3/Al_2O_3 and Sm_2O_3/Al_2O_3, Materials Letters 58(22-23) (2004) 2810-2814.

[19] T. Yamamoto, H. Kitaura, Y. Kodera, T. Ishii, M. Ohyanagi, Z.A. Munir, Consolidation of nanostructured β-SiC by spark plasma sintering, Journal of the American ceramic Society 87(8) (2004) 1436-1441.

[20] A. Lara, A.L. Ortiz, A. Muñoz, A. Domínguez-Rodríguez, Densification of additive-free polycrystalline β-SiC by spark-plasma sintering, Ceramics International 38(1) (2012) 45-53.

[21] A. Lara, R. Poyato, A. Munoz, A. Ortiz, A. Domínguez-Rodríguez, Spark plasma sintering and microstructural characterization of additive-free polycrystalline β-SiC, Key Engineering Materials, Trans Tech Publ, (2010), 67-72.

[22] J.S. Lee, Y.S. Ahn, T. Nishimura, H. Tanaka, S.H. Lee, Ultra-Low-Temperature Sintering of Nanostructured β-SiC, Journal of the American Ceramic Society 94(2) (2011) 324-327.

[23] L. Liu, L. Zhong, G. Geng, F. Ye, Y. Zhou, Effects of passing a direct current on densification of SiC ceramics with 10 wt.% Al_2O_3–Y_2O_3 as an additive, Materials Chemistry and Physics 165 (2015) 8-13.

[24] Y. Zhou, K. Hirao, M. Toriyama, H. Tanaka, Silicon carbide ceramics prepared by pulse electric current sintering of β–SiC and α–SiC powders with oxide and nonoxide additives, Journal of Materials Research 14(8) (1999) 3363-3369.

[25] Y.K. Seo, Y.W. Kim, T. Nishimura, W.S. Seo, High thermal conductivity of spark plasma sintered silicon carbide ceramics with yttria and scandia, Journal of the American Ceramic Society 100(4) (2017) 1290-1294.

[26] Y. Zhou, K. Hirao, Y. Yamauchi, S. Kanzaki, Effects of rare-earth oxide and alumina additives on thermal conductivity of liquid-phase-sintered silicon carbide, Journal of materials research 18(8) (2003) 1854-1862.

[27] T. Kinoshita, S. Munekawa, Effect of grain boundary segregation on thermal conductivity of hot-pressed silicon carbide, Acta materialia 45(5) (1997) 2001-2012.

[28] L. Sigl, Thermal conductivity of liquid phase sintered silicon carbide, Journal of the European Ceramic Society 23(7) (2003) 1115-1122.

[29] K. Pietrak, T.S. Wiśniewski, A review of models for effective thermal conductivity of composite materials, Journal of Power Technologies 95(1) (2014) 14-24.

[30] R. Malik, Y.-H. Kim, Y.-W. Kim, Effect of additive content on the mechanical and thermal properties of pressureless liquid-phase sintered SiC, Journal of Asian Ceramic Societies 8(2) (2020) 448-459.

[31] R. Progelhof, J. Throne, R. Ruetsch, Methods for predicting the thermal conductivity of composite systems: a review, Polymer Engineering & Science 16(9) (1976) 615-625.

[32] M.I. Mendelson, Average grain size in polycrystalline ceramics, Journal of the American Ceramic society 52(8) (1969) 443-446.

[33] W. Parker, R. Jenkins, C. Butler, G. Abbott, Flash method of determining thermal diffusivity, heat capacity, and thermal conductivity, Journal of applied physics 32(9) (1961) 1679-1684.

[34] R. German, Sintering: from empirical observations to scientific principles, Butterworth-Heinemann (2014).

[35] U. Kolitsch, H. Seifert, T. Ludwig, F. Aldinger, Phase equilibria and crystal chemistry in the Y_2O_3-Al_2O_3–SiO_2 system, Journal of materials research 14(2) (1999) 447-455.

[36] T. Grande, H. Sommerset, E. Hagen, K. Wiik, M.A. Einarsrud, Effect of weight loss on liquid-phase-sintered silicon carbide, Journal of the American Ceramic Society 80(4) (1997) 1047-1052.

[37] H. Tanaka, Silicon carbide powder and sintered materials, Journal of the ceramic society of Japan 119(1387) (2011) 218-233.

[38] N. Jepps, T. Page, Polytypic transformations in silicon carbide, Progress in crystal growth and characterization 7(1-4) (1983) 259-307.

[39] L. Ogbuji, T. Mitchell, A. Heuer, The β→αTransformation in poly crystalline SiC: III, the thickening of α plates, Journal of the American Ceramic Society 64(2) (1981) 91-99.

[40] S.A. Deshpande, T. Bhatia, H. Xu, N.P. Padture, A.L. Ortiz, F.L. Cumbrera, Microstructural Evolution in Liquid-Phase-Sintered SiC: Part II, Effects of Planar Defects and Seeds in the Starting Powder, Journal of the American Ceramic Society 84(7) (2001) 1585-1590.

[41] M. Lancin, C. Ragaru, C. Godon, Atomic structure and core composition of partial dislocations and dislocation fronts in β-SiC by high-resolution transmission electron microscopy, Philosophical Magazine B 81(11) (2001) 1633-1647.

[42] C. Ragaru, M. Lancin, C. Marhic, β⇒ α Phase transformation in SiC: Link between polytypism, dihedral angle and nucleation mechanism of α twins, Journal of the European Ceramic Society 19(15) (1999) 2701-2709.

[43] A. Heuer, G. Fryburg, L. Ogbuji, T. Mitchell, S. Shinozaki, β→α transformation in polycrystalline SiC: I, microstructural aspects, Journal of the American Ceramic Society 61(9-10) (1978) 406-412.

[44] S.-J.L. Kang, Sintering: densification, grain growth and microstructure, Elsevier (2004).

[45] Y.-W. Kim, M. Mitomo, G.-D. Zhan, Mechanism of grain growth in liquid-phase-sintered β–SiC, Journal of materials research 14(11) (1999) 4291-4293.

[46] J.C. Maxwell, A treatise on electricity and magnetism, Clarendon press (1881).

[47] G.-D. Zhan, M. Mitomo, A.K. Mukherjee, Effects of heat treatment and sintering additives on thermal conductivity and electrical resistivity in fine-grained SiC ceramics, Journal of materials research 17(9) (2002) 2327-2333.

[48] E. Volz, A. Roosen, S.-C. Wang, W.-C. Wei, Formation of intergranular amorphous films during the microstructural development of liquid phase sintered silicon carbide ceramics, Journal of materials science 39(13) (2004) 4095-4101.

[49] R. Huang, H. Gu, J. Zhang, D. Jiang, Effect of Y_2O_3–Al_2O_3 ratio on inter-granular phases and films in tape-casting α-SiC with high toughness, Acta materialia 53(8) (2005) 2521-2529.

[50] R.M. German, P. Suri, S.J. Park, Review: liquid phase sintering, J. Mater. Sci 44(1) (2009) 1-39.

[51] X. Dong, Y.C. Shin, Multiscale genome modeling for predicting the thermal conductivity of silicon carbide ceramics, Journal of the American Ceramic Society 99(12) (2016) 4073-4082.

[52] J.-P. Crocombette, L. Gelebart, Multiscale modeling of the thermal conductivity of polycrystalline silicon carbide, Journal of Applied Physics 106(8) (2009) 083520.

[53] D. Hasselman, L.F. Johnson, Effective thermal conductivity of composites with interfacial thermal barrier resistance, Journal of composite materials 21(6) (1987) 508-515.

[54] F. Yang, X. Zhao, P. Xiao, Thermal conductivities of YSZ/Al_2O_3 composites, Journal of the European Ceramic Society 30(15) (2010) 3111-3116.

[55] R. Riedel, Handbook of ceramic hard materials, (2000).

[56] T. Gupta, J. Valentich, Thermal expansion of yttrium aluminum garnet, Journal of the American Ceramic Society 54(7) (1971) 355-356.

[57] E.T. Swartz, R.O. Pohl, Thermal boundary resistance, Reviews of modern physics 61(3) (1989) 605.

[58] Y. Zhang, H. Zhang, J. Wu, X. Wang, Enhanced thermal conductivity in copper matrix composites reinforced with titanium-coated diamond particles, Scripta Materialia 65(12) (2011) 1097-1100.

[59] T.M. Tritt, Thermal conductivity: theory, properties, and applications, Springer Science & Business Media (2005).

[60] C. Wan, W. Pan, Q. Xu, Y. Qin, J. Wang, Z. Qu, M. Fang, Effect of point defects on the thermal transport properties of $(La_xGd_{1-x})_2Zr_2O_7$: Experiment and theoretical model, Physical Review B 74(14) (2006) 144109.

[61] R. Munro, Material properties of a sintered α-SiC, Journal of Physical and Chemical Reference Data 26(5) (1997) 1195-1203.

[62] W. Alton, A. Barlow, Temperature dependence of the elastic constants of yttrium aluminum garnet, Journal of Applied Physics 38(7) (1967) 3023-3024.

[63] F. Tang, W. Wang, X. Yuan, C. Zhu, J. Huang, C. Ma, F. Wang, Y. Lin, Y. Cao, Dependence of optical and thermal properties on concentration and temperature for Yb: YAG laser ceramics, Journal of alloys and compounds 593 (2014) 123-127.

[64] N.P. Padture, P.G. Klemens, Low thermal conductivity in garnets, Journal of the American Ceramic Society 80(4) (1997) 1018-1020.

3.3 Article II: Effects of grain growth on thermal conductivity of spark-plasma sintered SiC ceramics with Yttria and Scandia

Contributions:

Zhenfei Chai conceived the idea and methodology, carried out all of the experimental analysis and wrote the article. The article was internally discussed and reviewed by **Dr. Han Liu, Dr Zhaohe Gao** and **Prof. Ping Xiao**. **Dr. Han Liu** provided useful advice on presenting STEM-EDS results (table 3.6). **Dr. Gyorgyi Glodan** assisted in the spark plasma sintering experiments. **Prof. Ping Xiao** funded and supervised the work.

Effects of grain growth on thermal conductivity of spark-plasma sintered SiC ceramics with Yttria and Scandia

Zhenfei Chai[1], Han Liu[1], Zhaohe Gao[1], Gyorgyi Glodan[2], Ping Xiao[1,*]

[1] *Department of Materials, University of Manchester, Manchester UK, M13 9PL, UK*

[2] *Dalton Cumbrian Facility, University of Manchester, Westlakes Science & Technology Park, Moor Row, Cumbria CA24 3HA, UK*

Abstract: In this study, dense SiC ceramics were fabricated by spark plasma sintering (SPS) at final sintering temperature of 1750-1850 ºC for 5-240 min with 3 wt.% Y_2O_3-Sc_2O_3 as a sintering additive. Effects of final sintering temperature and holding time on densification, grain growth and microstructure as well as correlation between microstructure and thermal conductivity have been investigated. Increasing final sintering temperature and extending holding time have little influence on densification but change grain growth mechanism. At final sintering temperature of 1850 ºC, rapid grain growth from 0.71 ± 0.06 μm to 1.39 ± 0.31 μm (dynamic Ostwald ripening) takes place in initial 5 min followed by moderate grain growth from 1.39 ± 0.29 μm to 2.00 ± 0.54 μm (static Ostwald ripening) in rest 110 min of isothermal periods. At final sintering temperature of 1750 ºC, only static ripening is observed. Dominant grain growth mechanism during static ripening process changes from interface reaction at 1750 ºC to atom diffusion at 1850 ºC. Moreover, grain growth of the SiC ceramics not only reduces number of grain boundary per unit volume but also results in lattice purification, which is suggested to be responsible for higher thermal conductivity at larger grain size.

Key words: SiC; Y_2O_3-Sc_2O_3; SPS; grain growth; dynamic Ostwald ripening; thermal conductivity.

3.3.1 Introduction

SiC ceramics have attracted great attention due to its excellent properties including high thermal conductivity (490 W/(m•K) for single crystal 6H-SiC), excellent high temperature strength, good oxidation resistance to air and steam, and high radiation resistance [1-5]. They have been used in many fields, such as heat exchangers, substrate materials for high power electronics, cladding material for nuclear reactors, nozzles and so on [6-8]. High thermal conductivity of SiC ceramics is

one basic requirement for those applications. To the authors' knowledge, highest thermal conductivity of sintered SiC ceramics was 270 W/(m•K), which was achieved with BeO as a sintering additive [9]. Lower thermal conductivity (270 W/(m•K)) in the sintered SiC ceramic compared with counterpart (490 W/(m•K)) of single crystal SiC was attributed to additional phonon scattering by grain boundary of SiC, point defects formed via doping of BeO into SiC lattice and excess secondary phase of BeO [9]. The SiC ceramic sintered with BeO has not been widely studied and used due to high toxicity of BeO. It is thus necessary to explore new non-toxic sintering additives for obtaining dense SiC ceramics with high thermal conductivity.

Sintering additive is always necessary for fabricating dense SiC ceramics due to extremely low self-diffusion coefficient and high fraction (~88%) of covalent bond in SiC crystal [10]. Both solid state sintering additive and liquid phase sintering additive were extensively developed for fabricating dense SiC ceramics and resulted in different microstructures [11-14]. Al_2O_3-cotaining oxide mixtures were the most frequently used sintering additives because they not only have relative low liquid formation temperature but also could obtain microstructure with high fracture toughness [11, 15, 16]. But the SiC ceramics sintered with Al_2O_3-containing sintering additive generally possessed low thermal conductivity (<120 W/(m•K)) [17-19], which was attributed to doping of Al_2O_3 into SiC lattice via solution-reprecipitation mechanism (also called as Ostwald ripening) [20]. Such doping generated one-dimensional lattice defects (i.e. Si vacancy and substitutional atoms of Al and O) which could effectively scatter high-frequency phonons [20]. To obtain SiC ceramics with high thermal conductivity, mixture of rare-earth oxides has been developed as sintering additive [14, 20-23]. Mixture of Y_2O_3-Sc_2O_3 has been selected to fabricate dense SiC ceramic (called as SPS0.79) at 2050 °C for 6 h [21]. It was reported that the thermal conductivity was 262 W/(m•K), which is higher than counterparts of any other sintered SiC ceramics with sintering additives (except for SiC ceramics with BeO) [9, 21]. Kim et al. investigated thermal conductivity of the additive-free SiC ceramic (called as RHP0) and the SiC ceramic (called as RHP79) sintered with Y_2O_3-Sc_2O_3 at 2000 °C for 30 min [24]. Results showed that thermal conductivity (164 W/(m•K)) of RHP0 was higher than that (117 W/(m•K)) of RHP79, which was attributed to the almost clean grain boundaries, a relatively pure SiC lattice and absence of secondary phases with low thermal conductivity in RHP0 [24, 25]. Also, it

should be noted that thermal conductivity of the SiC ceramic (SPS0.79) containing secondary phases was higher than that of RHP0 without sintering additive [21, 24], which might be caused by the larger grain size (10.7 μm for SPS0.79 versus 7.2 μm for RHP0) and effective role of Y_2O_3-Sc_2O_3 in purifying SiC lattice. But detailed experimental evidence is required to verify above speculation.

Besides, the advanced sintering technique (SPS) has been applied to fabricate SiC ceramics and showed unique advantages (e.g. low sintering temperature and short sintering time). It was reported that nano SiC ceramics with relative density of 98% was obtained at 1700 °C for 10 min under 40 MPa even without sintering additive [26]. Up to now, it has been rarely to combine SPS and liquid sintering additive for fabricating SiC ceramics and undelying mechanism about densification and grain growth of spark-plasma sintered SiC ceramics in the presence of liquid phase sintering additive remains unclear [21, 25, 27].

In this study, SiC ceramics with variable grain size are designed and fabricated at 1750-1850 °C by SPS with 3 wt.% Y_2O_3-Sc_2O_3 as a sintering additive. Objectives of this study are to figure out not only mechanism of densification and grain growth during SPS process in the presence of liquid phase sintering additive but also dependence of thermal conductivity on grain growth. Results from this study may provide insight to fabricate SiC ceramics with high thermal conductivity.

3.3.2 Experimental Methods

3.3.2.1 Sample preparation

Raw powders used for fabrication of SiC ceramics by SPS are 97 wt.% β-SiC (0.8-1.2 μm, 99%, H. C. Starck), and 3 wt.% mixture of Y_2O_3 (99.99%, Sigma-Aldrich), and Sc_2O_3 (99.995%, Stanford Advanced Materials). Figure 3. 6 shows the binary phase diagram of Y_2O_3-Sc_2O_3 [28]. According to Figure 3. 6, when the molar ratio of Y_2O_3 and Sc_2O_3 is around 1:1.2, the lowest eutectic temperature is approximately 2100 °C. At the eutectic composition, $ScYO_3$ and a solid solution of $(Sc_xY_{1-x})_2O_3$ would be expected when the liquid mixture of Y_2O_3-Sc_2O_3 is cooled down to room temperature [28]. In this study, the molar ratio of Y_2O_3 and Sc_2O_3 is chosen as 2:1 at which the high thermal conductivity

of 262 W/(m•K) was reported for the sintered SiC ceramic [21]. Figure 3. 6 demonstrates that at the selected molar ratio of 2:1, a solid solution of $(Sc_{0.33}Y_{0.67})_2O_3$ would be generated.

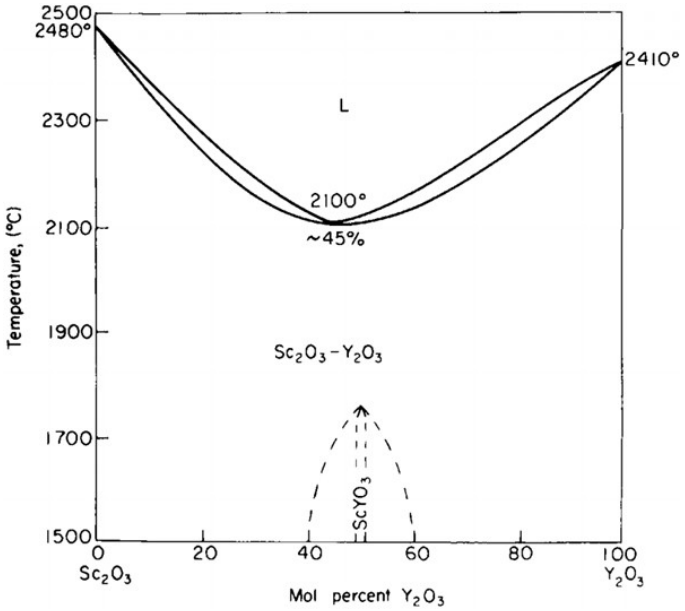

Figure 3. 6 Phase diagram of Y_2O_3-Sc_2O_3 system [28].

The raw powders were mixed for 8 h via the ball-milling method in which SiC balls and ethanol were adopted as milling media and solvent respectively. Then the as-obtained slurries were dried at 90 °C to eliminate the moisture followed by manual grinding using agate mortar and pestle. Finally, the ball-milled powders were poured into graphite die with inner diameter of 12.7 mm and sintered in the SPS machine (DCS 10-4, Thermal Technology, GT Advanced Technology) with pulsed direct current (maximum voltage and current are 10 V and 4000 A respectively). Thin graphite foils were inserted in the contact areas among graphite pieces and powders to easily remove the sintered pellet. To minimize the measurement error of sintering temperature, a hole locating at ~3.15 mm away from the boundary between SiC pellet and graphite die was produced inside the graphite die and monitored by a thermopyrometer.

Two types of heating protocols were adopted: for first heating protocol, green compacts were directly heated to 1850 °C and held at 1850 °C for 5-120 min, followed by cooling down to 600 °C; for second heating protocol, green compacts were firstly heated to 1850 °C, then immediately decreased to 1750 °C and held at 1750 °C for 30-240 min, finally cooled down to 600 °C. The second heating

protocol was developed to ensure full densification because final sintering temperature (1750 °C) in the protocol is about 300 °C lower than reported temperature (2050 °C) for fabricating dense SiC ceramics with same type of sintering additives [21]. Difference between these 2 protocols could be simplified as difference between final sintering temperature. Despite final sintering temperature used, heating/cooling rate and vacuum pressure were chosen as 100 °C/min and 5 Pa respectively. The uniaxial pressure of 20 MPa was initially applied to the ball-milled powders prior to 600 °C to minimize electrical contact resistance. Then the pressure of 60 MPa was progressively increased from 600 °C, achieved at about 1850 °C, and reduced to 20 MPa in the end of isothermal period.

3.3.2.2 Characterization

3.3.2.2.1 Density, composition and microstructure

Densities of sintered SiC samples were measured according to the Archimedes principle in an analytical balance with high accuracy (0.001 g). The theoretical density of SiC ceramics sintered with 3 wt.% Y_2O_3-Sc_2O_3 is 3.2397 g/cm^3, which was obtained by mixing rules whose mathematical form is shown in equation 3.1.

XRD technique (Rigaku D/Max-γB X-ray diffractometer, with Cu Kα radiation (λ = 0.154178 nm)) was used to characterize the cross section composition of sintered SiC ceramics. Prior to the measurement, the cross sections were ground, polished and cleaned by acetone subsequently. Microstructures of polished samples were investigated by Field Emission Scanning Electron Microscopy (FEG-SEM, FEI Quanta 250). BSE images were utilized to get mean grain size via the line intercept method whose details are described elsewhere [29]. Over 200 grains were measured to obtain average grain size of sintered samples.

Focused ion beam (FIB, FEI Quanta 3D FIB) was selected to prepare thin lamellas from cross section of sintered SiC ceramics. The lamellas were then examined by transmission electron microscopy (TEM, FEI Talos, F200A) equipped with Super-X Energy dispersive X-ray spectroscopy (EDS)

system and high angle annular dark field (HAADF) detector. To figure out element distribution, EDS-mapping was conducted in several positions containing grain boundaries and triple points of a lamella.

3.3.2.2.2 Thermal conductivity

Thermal diffusivity from room temperature to 1000 °C was obtained by laser flash technique (LFA 427 on 18-414/4, NETZSCH GmbH) in Ar atmosphere. To ensure the bottom surface is parallel to the top surface, surfaces of the sintered disk samples with diameter of 12.7 mm and thickness of ~2 mm were ground and cleaned by acetone subsequently. Thin graphite coating was sprayed on sintered SiC samples to maximize heat absorption of bottom surface and thermal radiation of top surface. Specific heat (C_p) ranging from 50 °C to 1000 °C in Ar atmosphere was measured by differential scanning calorimetry (DSC-STA449C, NETZSCH GmbH). Finally, thermal conductivities (k) could be calculated according to equation 3.3.

3.3.3 Results

3.3.3.1 Phase composition and microstructure

Table 3. 5 shows fabrication conditions and corresponding densities/grain sizes of spark plasma sintered SiC ceramics using 3 wt.% mixture of Y_2O_3-Sc_2O_3 (molar ratio of 2:1) as a sintering additive. Concerning specimen ID in Table 3. 5, 3YSc is abbreviation of the 3 wt.% sintering additive of Y_2O_3-Sc_2O_3. The number of 18 and 18-17 after 3YSc mean final sintering temperature of 1850 ºC and 1750 ºC respectively. For instance, 3YSc18-17 means 3 wt.% mixture of Y_2O_3-Sc_2O_3 and final sintering temperature of 1750 ºC are used. 3YSc18 means that 3 wt.% mixture of Y_2O_3-Sc_2O_3 and final sintering temperature of 1850 ºC are used. For the case of YSc18-17, green compacts of SiC are firstly heated to 1850 ºC and then immediately decreased to final sintering temperature of 1750 °C. For the case of YSc18, green compacts of SiC are directly heated to final sintering temperature of 1850 °C. 5 min, 10min, 30 min, 60min, 120 min and 240 min mean holding time at respective final sintering temperature.

According to Table 3. 5, high relative densities (>99%) are achieved in all spark plasma sintered SiC ceramics. For spark plasma sintered SiC ceramics with Y_2O_3-Sc_2O_3, variation of final sintering temperature and holding time do not show obvious effects on relative density. Furthermore, final sintering temperature required for full densification of the SiC ceramic (labelled as MI3YSc18-17-30min) is as low as 1750 °C (Table 3. 5), which is 350 °C lower than the lowest liquid formation temperature (2100 °C) of Y_2O_3-Sc_2O_3 system [28]. Such low final sintering temperature of 1750 °C in this study might be attributed to presence of SiO_2 on surface of starting SiC powders. It was reported that the reaction between SiO_2 and Sc_2O_3/Y_2O_3 could reduce liquid formation temperature to around 1660 °C [28, 30, 31]. In addition, higher heating rate of SPS process (100 °C/min) compared with conventional sintering process (<50 °C/min) inhibited possible weight loss of liquid phase sintering additive [32]. Details of densification mechanism in SPS will be discussed below. Overall, such low content of sintering additive and short holding time at 1750 °C are of great significance for obtaining excellent comprehensive performance of SiC based composites.

Table 3. 5 Fabrication parameters and relative densities/grain sizes of spark plasma sintered SiC ceramics with 3 wt.% mixture of Y_2O_3-Sc_2O_3 (molar ratio of 2:1) as a sintering additive at final sintering temperature of 1750-1850 ºC for 5-240 min.

Specimen ID*	Sintering additive composition	Sintering temperature ** (ºC)	Holding time (min)	Relative density*** (%)	Grain size (μm)
MI3YSc18-5min	Y_2O_3-Sc_2O_3 (molar ratio of 2:1)	1850	5	99.6 ± 0.59	1.39 ± 0.31
MI3YSc18-10min		1850	10	99.8 ± 0.14	1.39 ± 0.29
MI3YSc18-30min		1850	30	99.6 ± 0.23	1.59 ± 0.34
MI3YSc18-120min		1850	120	99.6 ± 0.03	2.00 ± 0.54
MI3YSc18-17-30min		1750	30	99.7 ± 0.27	0.71 ± 0.06
MI3YSc18-17-60min		1750	60	99.2 ± 0.70	0.78 ± 0.11
MI3YSc18-17-240min		1750	240	99.7 ± 0.19	1.25 ± 0.21

Note: (1) * YSc18 means green compacts of SiC with Y_2O_3-Sc_2O_3 were directly heated to final sintering temperature of 1850 ºC, and YSc18-17 means green compacts of SiC with Y_2O_3-Sc_2O_3 were firstly heated to 1850 ºC and then immediately decreased to final sintering temperature of 1750 °C; (2) ** sintering temperature means final sintering temperature; (3) *** relative density is obtained by dividing measured density over theoretical density of SiC ceramics and theoretical density is calculated by mixing rule (equation 3.1).

Figure 3. 7(a) shows XRD spectra of starting SiC powder and ball-milled SiC powder with 3 wt.% Y_2O_3-Sc_2O_3. It can be seen that there is small amount of 6H-SiC apart from the main phase 3C-SiC (also called as β-SiC) in starting SiC powder, which is accordance with data analysis result (content of 6H-SiC lower than 5.6 wt.%) provided by H. C. Starck. 3C-SiC, 6H-SiC and cubic Y_2O_3 were detected in ball-milled powder. In addition, the diffraction peak with maximum intensity for Sc_2O_3 locates around 31.5º, which is not visible in the XRD spectrum of the ball-milled starting powder. Absence of Sc_2O_3 is suggested to be caused by its low content (0.7026 wt.%) that is beyond detectability limit of the XRD equipment. Furthermore, there is no difference between the peak

intensity ratio of 3C-SiC and 6H-SiC in starting SiC powder and ball-milled SiC powder, implying that negligible contamination from ball-milling process.

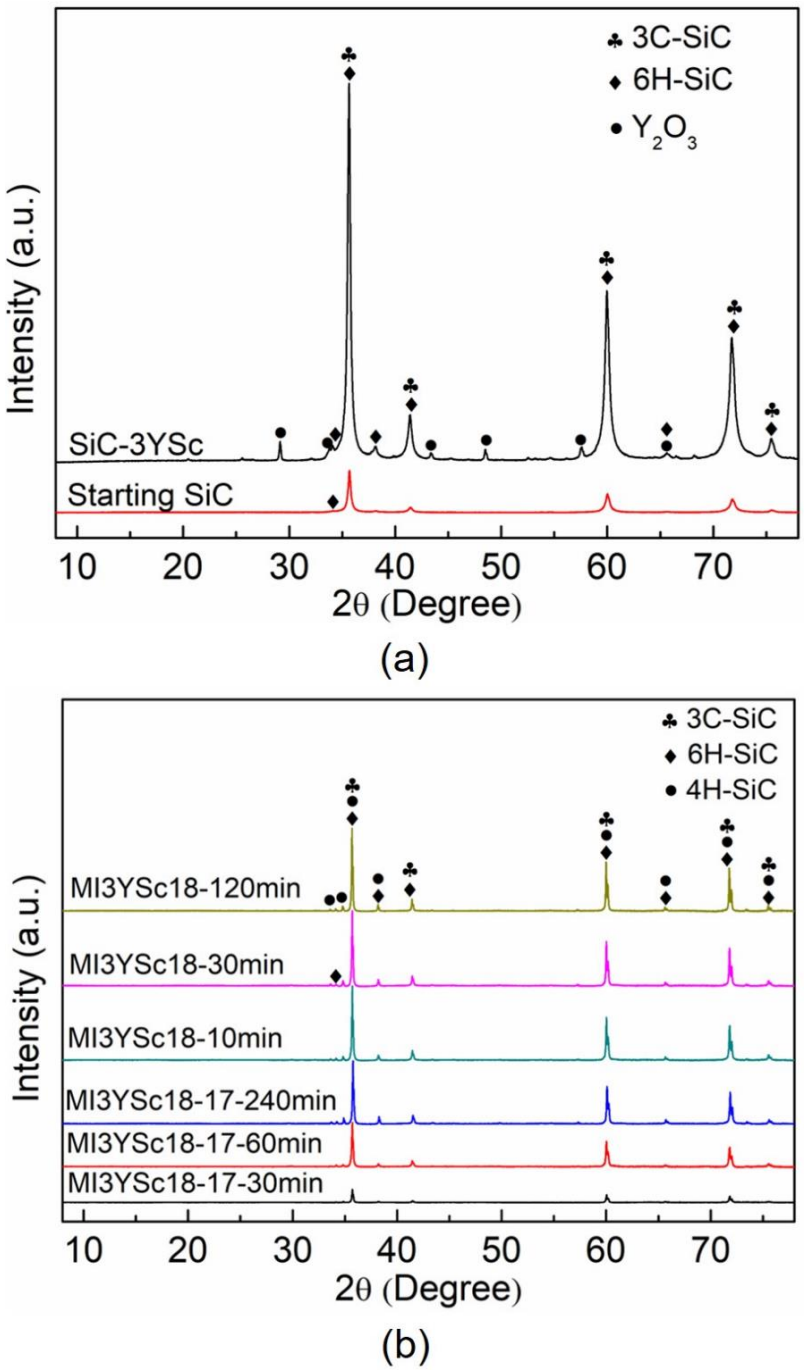

Figure 3. 7 XRD spectra of SiC: (a) starting SiC powders and (b) spark plasma sintered SiC ceramics under different conditions. 3YSc is abbreviation of the 3 wt.% sintering additive of Y_2O_3-Sc_2O_3. The number of 18 and 18-17 after 3YSc mean final sintering temperature of 1850 ºC and 1750 ºC respectively. 10 min-240 min mean holding time at corresponding final sintering temperatures.

Figure 3. 7(b) shows XRD spectra of spark plasma sintered SiC ceramics under different final sintering temperatures and holding times. According to Figure 3. 7(b), only β-SiC (3C-SiC) and α-SiC (referred as all SiC polytypes except 3C-SiC) are observed in all sintered samples. The main peaks corresponding to Y_2O_3 and Sc_2O_3 locate at 29.2° and 31.5° respectively, which however are not visible in the XRD spectra of sintered SiC ceramics. As mentioned above, the sintering additive could react with silica impurity of starting SiC powder and form the melt containing Y, Sc, Si, O and C. Depending on the sintering conditions (e.g. cooling rate, sintering additive content, molar ratio between Y_2O_3 and Sc_2O_3), other secondary phase including $Y_2Si_2O_7$, $Y_3Si_2C_2$, solid solution $(Sc, Y)_2Si_2O_7$ and glass phase Y-Sc-Si-O-C could generate in sintered SiC ceramics [21, 23]. The absence of secondary phase containing sintering additive in the XRD spectra of sintered SiC ceramics is suggested to be caused by the low content of abovementioned secondary phase especially considering that the content of Y_2O_3-Sc_2O_3 was only 3 wt.%. For the SiC ceramics sintered with Y_2O_3-Sc_2O_3, at constant final sintering temperature, extending holding time results in more α-SiC (especially more 4H-SiC) and less β-SiC according to peak intensity ratio of β-SiC and α-SiC. The phase transformation is related to thermal stability of SiC polytype. It was found that β-SiC (3C-SiC) was stable below 1600 °C while some α-SiC (e.g. 4H-SiC, 6H-SiC and 15R-SiC) was stable at temperature higher than 1600 °C [33]. Hence, α-SiC is generally more preferred in SiC ceramics sintered for longer holding time due to higher thermal stability. Furthermore, more 4H-SiC in the SiC ceramics sintered for longer holding time at the elevated temperature (1750 °C and 1850 °C) implies that 4H-SiC has higher thermal stability than that of 6H-SiC.

Figure 3. 8 are BSE images of polished cross section of spark plasma sintered SiC ceramics under different sintering conditions. Black contrast marked by a black arrow and white contrast marked by a white arrow correspond to a pore and sintering additive containing large atoms (Y and Sc) respectively. Grey contrast surrounded by a dotted line is a SiC grain. Grain 1 and 2 have elongated shape which is typical for α-SiC. The elongated morphology of α-SiC is attributed to its anisotropic interface energy [34]. Grain 3 and 4 have equiaxed shape which is typical for β-SiC. Simultaneous occurrence of β-SiC and α-SiC indicates phase transformation from β-SiC to α-SiC is not finished under current sintering conditions. Pores mainly locates in multi-grain junctions. Some pores with

rounded/faceted interface could be caused by evaporation of liquid sintering additive at high sintering temperature. Other irregular pores with significantly different curvature may be attributed to absence of liquid filling [35]. Sintering additive containing Y and Sc mainly locates in triple points although some relative thin sintering additive film can be found in grain boundaries. Besides, it is stressed that liquid phase sintering of SiC ceramics using 3 wt.% mixture of Y_2O_3-Sc_2O_3 as a sintering additive is achieved even at 1750 °C (350 °C lower than eutectic temperature of Y_2O_3-Sc_2O_3 system) in this study, which is verified by the impregnation of small grains in liquid phase pockets marked by the solid line in the bottom left of Figure 3. 8. In summary, according to SEM images of SiC ceramics sintered with 3 wt.% Y_2O_3-Sc_2O_3, distribution of pore and sintering additive do not change with holding time and final sintering temperature.

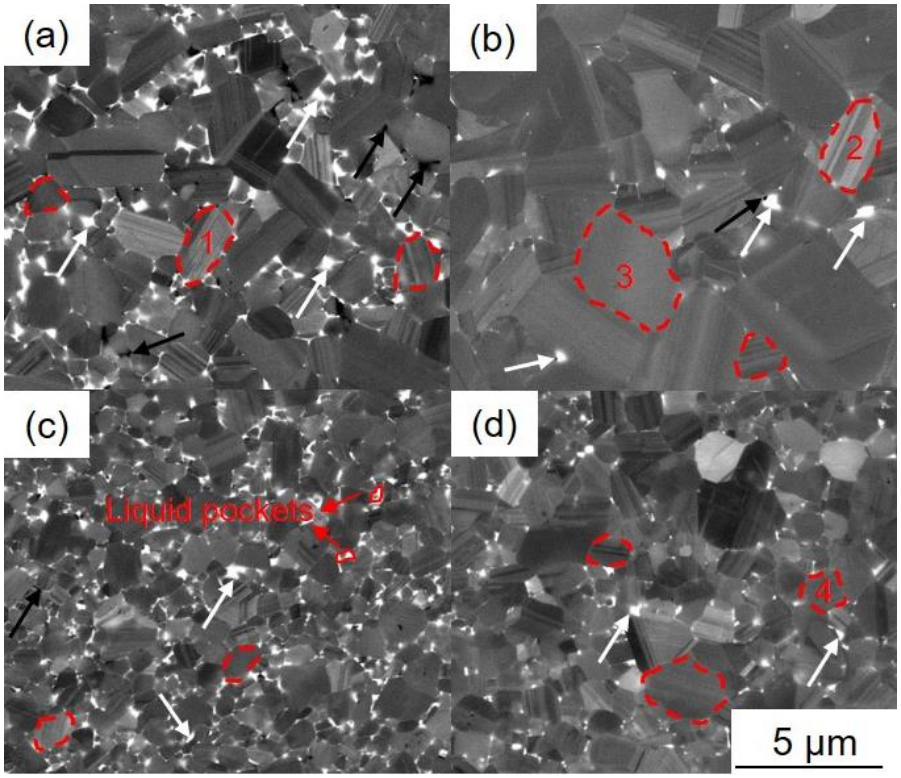

Figure 3. 8 Polished cross section images of SiC ceramics sintered with 3 wt.% Y_2O_3-Sc_2O_3 under different sintering conditions: (a) final sintering temperature of 1850 ºC and 10 min, MI3YSc18-10min; (b) final sintering temperature of 1850 ºC and 120 min, MI3YSc18-120min; (c) final sintering temperature of 1750 ºC and 30 min, MI3YSc18-17-30min; (d) final sintering temperature of 1750 ºC and 240 min, MI3YSc18-17-240min. Four images have same scale bar. Black arrow and white arrow indicate pores and sintering additive containing large atom (Y and Sc) respectively. Red dotted line indicates a grain boundary.

Grain sizes of all spark plasma sintered SiC ceramics were measured by line intercept method based on their respective BSE images and summarized in Table 3. 5. According to Table 3. 5, when final sintering temperature is 1850 ºC, extending holding time from 5 min to 10min (comparison between MI3YSc18-5min and MI3YSc18-10min) does not result in grain growth. When holding time increases from 10 min to 120 min (comparison between MI3YSc18-10min and MI3YSc18-120min), moderate grain growth from 1.39 ± 0.29 μm to 2.00 ± 0.54 μm is observed. Also, grain size (0.71 ± 0.06 μm) of the SiC ceramic sintered at final sintering temperature of 1750 ºC for 30 min (labelled as MI3YSc18-17-30min) is much smaller than counterpart (1.39 ± 0.29 μm) of the SiC ceramic sintered at final sintering temperature of 1850 ºC for 5 min (labelled as MI3YSc18-5min) even though former SiC (MI3YSc18-17-30min) was firstly heated to 1850 ºC and then immediately reduced to final sintering temperature of 1750 ºC. The result implies that at final sintering temperature of 1850 ºC, grain growth rate (grain growth mechanism) changes with holding time: rapid grain growth in initial 5 min, negligible grain growth from 5 min to 10 min and moderate grain growth from 10 min to 120 min, which has never been reported in SiC ceramics sintered by SPS. In addition, when final sintering temperature is 1750 ºC, extending holding time from 30 min to 240 min (comparison between MI3YSc18-17-30min and MI3YSc18-17-240min) result in moderate grain growth from 0.71 ± 0.06 μm to 1.25 ± 0.21 μm. Details of grain growth mechanism in spark plasma sintered SiC with 3 wt.% Y_2O_3-Sc_2O_3 will be discussed below.

To study sintering additive distribution in spark plasma sintered SiC ceramics, HAADF and STEM-EDS were used to characterize sample MI3YSc18-10min, MI3YSc18-120min and MI3YSc18-17-240min. Contrast in HAADF images is determined by amount of Rutherford scattered electrons with very high scattering angles. Elements with higher atomic numbers can scatter more electrons at higher angles and thus appear as brighter in HAADF images. Figure 3. 9 demonstrates HAADF image (top left) of the SiC ceramic sintered with 3 wt.% Y_2O_3-Sc_2O_3 at 1850 °C for 10 min (labelled as MI3YSc18-10min). White contrast marked by a white arrow corresponds to sintering additive containing Y and Sc. A red arrow indicates grain boundary. White contrast can be found in grain boundaries and triple points in this HAADF image, although white contrast in some grain boundaries is not obvious (e.g. grain boundary 1 (GB1) marked with a red double arrow). The EDS-line spectrum

(in the bottom left of Figure 3. 9) along GB1 in HAADF image shows there is segregation of Y, Sc and O in this grain boundary. EDS-mapping results (in the right of Figure 3. 9) further demonstrate that sintering additive containing Y, Sc and O segregates in triple points and grain boundaries. Other 9 grain boundaries in different positions have also been examined and similar phenomena have been confirmed. Overall, as short holding time of 10 min was used, sintering additive distributed in both grain boundaries and triple points.

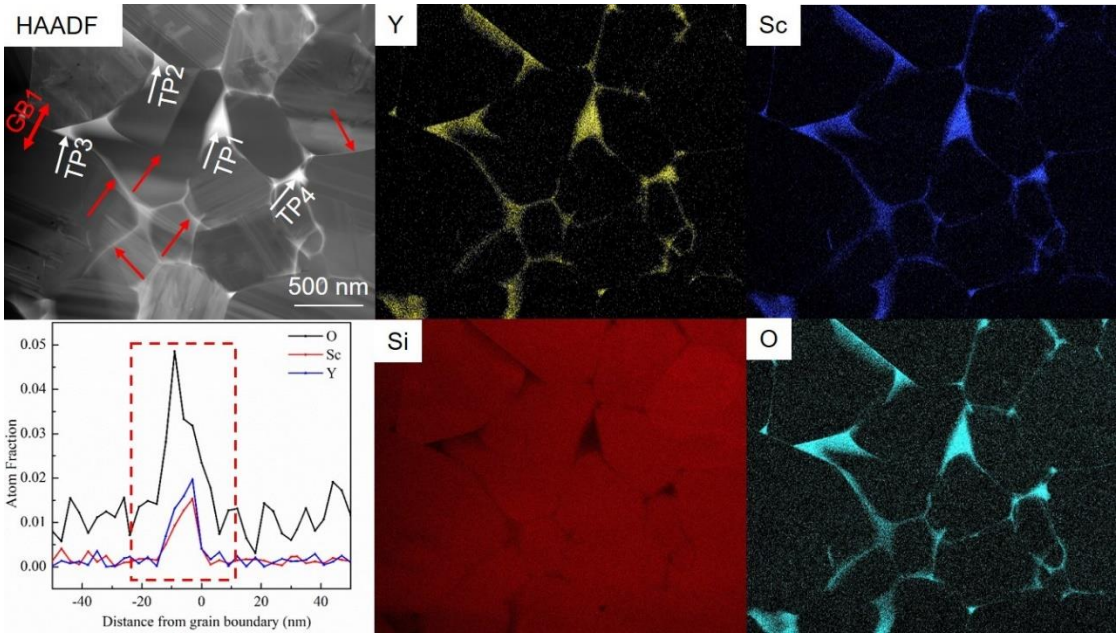

Figure 3. 9 HAADF images and EDS analysis of SiC ceramics sintered by SPS with 3 wt.% Y_2O_3-Sc_2O_3 at final sintering temperature of 1850 ºC for 10 min (labelled as MI3YSc18-10min). Red arrow and white arrow are grain boundary and the sintering additive containing large atoms (Y and Sc) respectively. White contrast in grain boundary indicates presence of sintering additive. Composition variation along the red double arrow crossing grain boundary 1 (GB1) is determined by EDS and shown in the bottom left spectrum.

Table 3. 6 shows EDS results on triple points of the SiC ceramic sintered with 3 wt.% Y_2O_3-Sc_2O_3 at 1850 °C for 10 min (labelled as MI3YSc18-10min). According to Table 3. 6, secondary phase distributing in triple points contains O, Si, Sc, Y and C, suggesting small SiC grain including SiO_2 present on its surface dissolves into liquid phase sintering additive during sintering process. The atom ratio of (Y+Sc)/O in the triple points (marked as TP1, TP2, TP3 and TP4 in Figure 3. 9) of MI3YSc18-10min was quantitatively determined by STEM-EDS and then compared with counterpart

of raw sintering additive powders. Table 3. 6 shows that atom ratio of the triple points ranges between 0.203 and 0.302, which is much smaller than counterpart (0.67) of raw sintering additive powders (Y_2O_3-Sc_2O_3). The lower atom ratio in triple points of the sintered SiC ceramic (MI3YSc18-10min) is suggested to be caused by the increased oxygen originating from the silica impurity of starting SiC powder because both Y and Sc have very low solubility limit in SiC lattice [36, 37].

Table 3. 6 EDS results on triple points of the SiC ceramic sintered with 3 wt.% Y_2O_3-Sc_2O_3 at 1850 ºC for 10 min (labelled as MI3YSc18-10min). Triple points are marked by white arrows in Figure 3. 9.

Position number	Atom fraction (at.%)					Ratio of (Y+Sc)/O
	O	Si	Sc	Y	C	
TP1	62.66	19.62	5.350	12.37	N/A	0.283
TP2	43.83	25.37	3.309	8.071	19.42	0.260
TP3	64.35	10.44	3.297	9.783	12.13	0.203
TP4	63.26	17.66	5.600	13.48	N/A	0.302

Figure 3. 10 demonstrates HAADF image and EDS results of the SiC ceramic sintered with 3 wt.% Y_2O_3-Sc_2O_3 at 1850 °C for 120 min (labelled as MI3YSc18-120min). According to HAADF image and EDS-mapping results (in the right of Figure 3. 10), sintering additives containing Y, Sc and O distribute in triple points and grain boundaries. The EDS-line spectrum (in the bottom left of Figure 3. 10) across the grain boundary (GB1) marked with a red double arrow clearly shows that atom fractions of O, Sc and Y in this grain boundary are higher than counterparts inside SiC grains. Other 9 grain boundaries in different positions have also been examined and similar phenomena have been confirmed. Overall, as long holding time of 120 min is used, sintering additive also distributes in both grain boundaries and triple points. In other words, for SiC ceramics sintered with 3 wt.% Y_2O_3-Sc_2O_3 at final sintering temperature of 1850 °C, a continuous network of sintering additive has formed and independent of holding time.

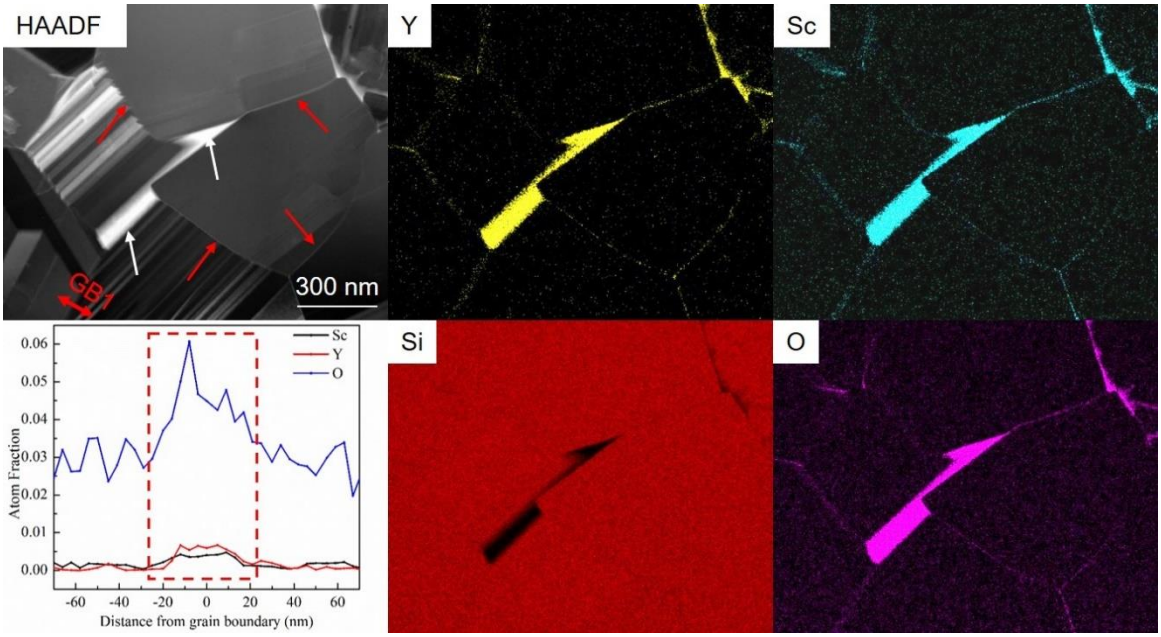

Figure 3. 10 HAADF images and EDS analysis of SiC ceramics sintered by SPS with 3 wt.% mixture of Y_2O_3-Sc_2O_3 at final sintering temperature of 1850 ºC for 120 min (labelled as MI3YSc18-120min). Red arrow and white arrow are grain boundary and the sintering additive containing large atoms (Y and Sc) respectively. White contrast in grain boundary indicates presence of sintering additive. Composition variation along the red double arrow crossing grain boundary 1 (GB1) is determined by EDS and shown in the bottom left spectrum.

Figure 3. 11 shows HAADF image and EDS results of the SiC ceramic sintered with 3 wt.% Y_2O_3-Sc_2O_3 at final sintering temperature of 1750 °C for 240 min (labelled as MI3YSc18-17-240min). Based on EDS mapping results (in the right of Figure 3. 11), it can be clearly seen that sintering additive locates in triple points and grain boundaries. The EDS-line spectrum (in the bottom left of Figure 3. 11) across the grain boundary 1 (GB1) marked with a red double arrow in the HAADF image (in the top left of Figure 3. 11) further confirms segregation of Y, Sc and O. Other 9 grain boundaries in different positions have also been examined and similar phenomena have been confirmed. In summary, for SiC ceramics sintered with 3 wt.% Y_2O_3-Sc_2O_3, despite final sintering temperature and holding time employed, a continuous network of sintering additive has formed.

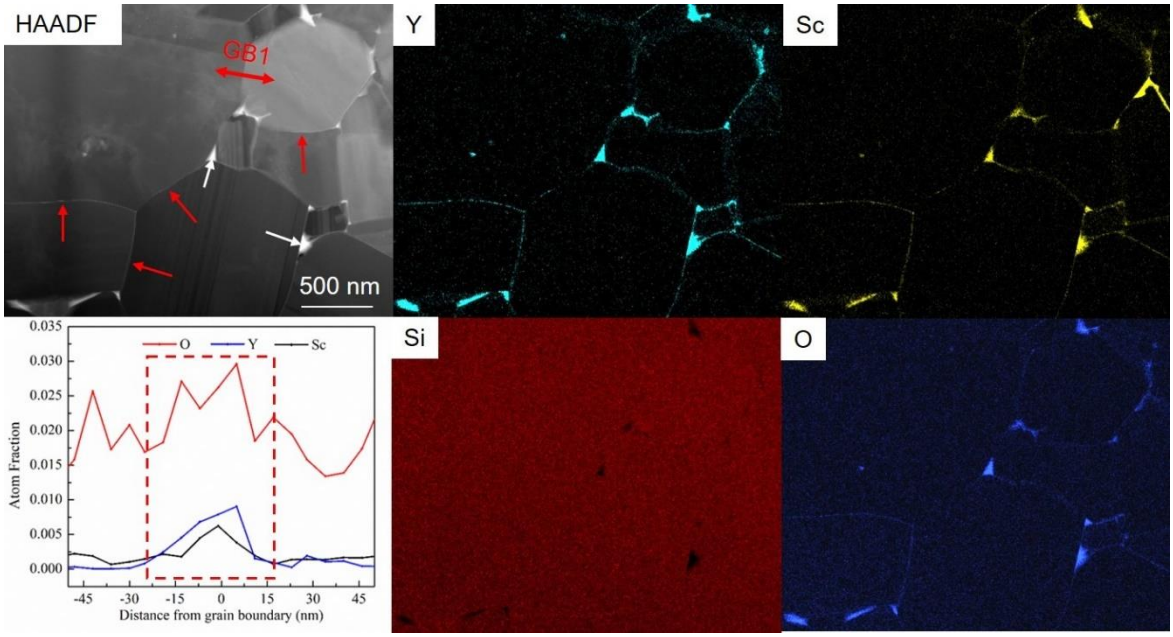

Figure 3. 11 HAADF images and EDS analysis of SiC ceramics sintered by SPS with 3 wt.% mixture of Y_2O_3-Sc_2O_3 at final sintering temperature of 1750 ºC for 240 min (labelled as MI3YSc18-17-240min). Red arrow and white arrow are grain boundary and the sintering additive containing large atoms (Y and Sc) respectively. White contrast in grain boundary indicates presence of sintering additive. Composition variation along the red double arrow crossing grain boundary 1 (GB1) is determined by EDS and shown in the bottom left spectrum.

3.3.3.2 Thermal conductivity

Figure 3. 12(a) shows influence of measurement temperature on thermal conductivity of the SiC ceramic sintered with 3 wt.% Y_2O_3-Sc_2O_3 at 1850 ºC for 120 min (labelled as MI3YSc18-120min). The black line demonstrates experimental thermal conductivity of MI3YSc18-120min while the red line gives derived thermal conductivity of 'fully dense' MI3YSc18-120min. Thermal conductivity of fully dense ceramics is calculated via the derived Maxwell model and experimental thermal conductivity. More details about the derived Maxwell model have been described in section 3.2.3.2 of article I. Equation 3.4 shows the mathematical form of the derived Maxwell model.

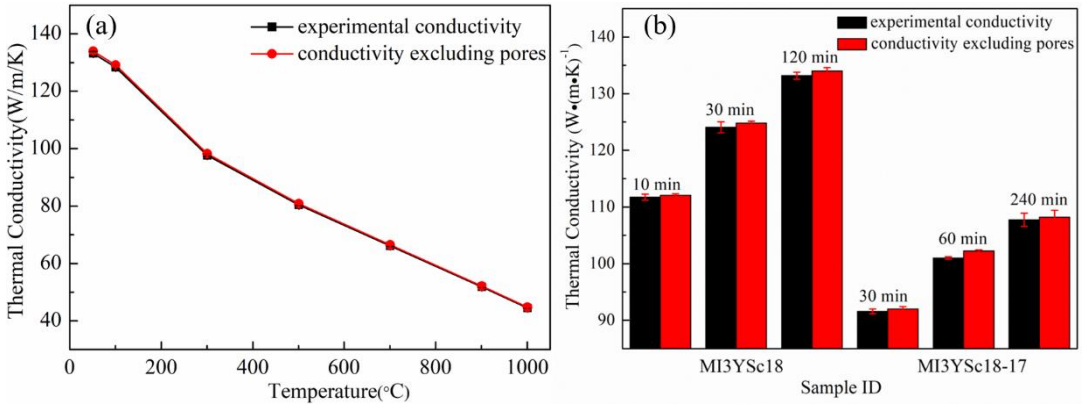

Figure 3. 12 Thermal conductivities of sintered SiC ceramics: (a) the SiC ceramic sintered with 3 wt.% mixture of Y_2O_3-Sc_2O_3 at 1850 ºC for 120 min (labelled as MI3YSc18-120min) at different measurement temperature; (b) sintered SiC ceramics fabricated under different conditions at measurement temperature of 50 °C. Fabrication conditions for each sample can be found in Table 3. 5. Note red line (left picture) and red columns (right picture) are thermal conductivities of 'fully dense' SiC ceramics derived according to experimental conductivity (black line and black columns) and equation 3.4. Error bar of conductivity is smaller than the symbol size if they are not shown.

According to Figure 3. 12(a), experimental thermal conductivity of MI3YSc18-120min is very close to derived thermal conductivity of fully dense SiC ceramics, suggesting that pores have negligible effects on heat conduction in this study. Also, thermal conductivity decreases with measurement temperature, implying phonon-phonon Umklapp process is main mechanism controlling heat conduction [38]. Highest thermal conductivity of 133 ± 0.63 W/(m•K) of MI3YSc18-120min is obtained at measurement temperature of 50 °C, which is higher than reported counterpart (117 W/(m•K) at room temperature) of the SiC ceramic sintered with 1.11 wt.% Y_2O_3-Sc_2O_3 at 2000 °C for 30 min (labelled as RHP0.79) [24]. Grain size (2.00 ± 0.54 μm) of MI3YSc18-120min is larger than that (1.5 μm) of RHP0.79. Besides, nitrogen atmosphere (N_2) was used in fabricating RHP0.79 while vacuum atmosphere was selected in fabricating MI3YSc18-120min. It was reported that N originating from sintering atmosphere could dope into SiC lattice via solution-reprecipitation mechanism during liquid phase sintering process and create point defects/defect cluster (e.g. substitutional atoms of N at C site (N_C) and vacancy complex ((N_C)$_4$-V_{Si}) which could scatter high frequency phonons [23, 39, 40]. Hence, it is suggested that larger grain size and absence of N doping in SiC lattice are

responsible for higher thermal conductivity of MI3YSc18-120min compared with counterparts of RHP0.79.

Figure 3. 12(b) demonstrates thermal conductivity at 50 °C of SiC ceramics fabricated under different sintering conditions. Black column and red column give experimental thermal conductivity of sintered ceramics and derived thermal conductivity of 'fully dense' ceramics respectively. Above mentioned Maxwell model is also used to derive thermal conductivity of 'fully dense' ceramics. The small difference between experimental thermal conductivity and derived thermal conductivity again indicates that pores have negligible effects on heat conduction in this study.

According to Figure 3. 12(b), measured thermal conductivity at 50 °C of SiC ceramics sintered with 3 wt.% Y_2O_3-Sc_2O_3 varies from 92 ± 0.49 W/(m•K) to 133 ± 0.63 W/(m•K). When comparing SiC ceramics sintered at same final sintering temperature of 1850 °C but different holding times (comparison between MI3YSc18-10min and MI3YSc18-120min), it can be found that extending holding time from 10 min to 120 min results in grain growth from 1.39 ± 0.29 μm to 2.00 ± 0.54 μm (Table 3. 5). Meanwhile, thermal conductivity increases from 112 ± 0.55 W/(m•K) to 133 ± 0.63 W/(m•K). Similar grain size effect on thermal conductivity is also observed in the SiC ceramics sintered at final sintering temperature of 1750 °C (comparison between MI3YSc18-17-30min and MI3YSc18-17-240min). In summary, despite final sintering temperature and holding time, for SiC ceramics sintered with 3 wt.% Y_2O_3-Sc_2O_3 in this study, larger grain size generally results in higher thermal conductivity, implying positive role of grain growth in increasing thermal conductivity.

3.3.4 Discussion

The above mentioned results demonstrate that full densification of SiC ceramics sintered by SPS with 3 wt.% Y_2O_3-Sc_2O_3 could be achieved at low sintering temperature 1750 °C for short sintering time, implying unique advantages of SPS. However, densification mechanism during SPS process in the presence of liquid phase sintering additive remains unclear. In addition, at final sintering temperature of 1850 ºC, grain growth rate (grain growth mechanism) changes with holding time. But related grain growth mechanism is not known. Moreover, grain growth results in higher thermal

conductivity for SiC sintered with 3 wt.% Y_2O_3-Sc_2O_3. Following discussion will focus on mechanism of densification and grain growth during SPS in the presence of liquid phase sintering additive as well as effects of grain growth on thermal conductivity.

3.3.4.1 Densification and grain growth mechanism during SPS

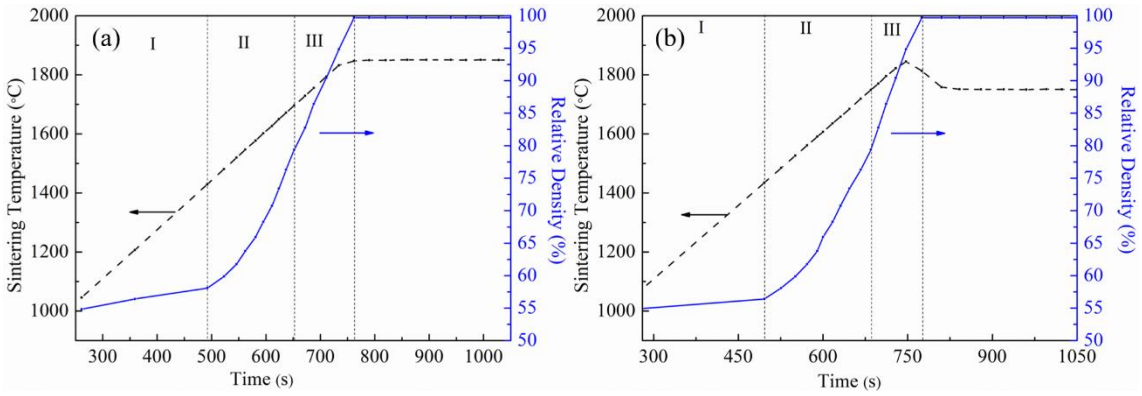

Figure 3. 13 Densification curves of SiC ceramics sintered by SPS with 3 wt.% Y_2O_3-Sc_2O_3 under different final sintering temperatures: (a) the SiC compacts were directly heated to final sintering temperature of 1850 °C and held at 1850 °C for different times (a series of samples labelled as MI3YSc18-Xmin, X = 5, 10, 30, 120); (b) the SiC compacts were firstly heated to 1850 °C then immediately decreased to final sintering temperature of 1750 °C and held at 1750 °C for different times (a series of samples labelled as MI3YSc18-17-Ymin, Y= 30, 60, 240). Only beginning part of whole isothermal period is shown in these figures for relative density keeps constant in rest part.

Figure 3. 13 shows densification curves of spark plasma sintered SiC ceramics 3 wt.% Y_2O_3-Sc_2O_3 under different final sintering temperatures. These densification curves were obtained by converting height change of SiC compacts to relative density evolution during sintering process. Figure 3. 13(a) corresponds to the densification curve of SiC ceramics (a series of samples labelled as MI3YSc18-Xmin, X = 5, 10, 30, 120) which are directly heated to final sintering temperature of 1850 °C and held at 1850 °C for different times. Full densification could be achieved as sintering temperature is held at 1850 °C for around 30 s. Long holding time does not influence relative density. Figure 3. 13(b) is the densification curve of SiC ceramics (a series of samples labelled as MI3YSc18-17-Ymin, Y= 30, 60, 240) which are firstly heated to 1850 °C then immediately decreased to final sintering temperature

of 1750 °C and held at 1750 °C for different times. Full densification can be achieved during short transition stage from 1850 °C to 1750 °C. Furthermore, in view of densification rate determined by slope of relative density-time curves, densification process of SiC ceramics sintered by SPS in the presence of 3 wt.% Y_2O_3-Sc_2O_3 could be divided into 3 different stages which are marked as I, II and III in Figure 3. 13.

In Figure 3. 13(a) and (b), stage I ends at around 1430 °C and is achieved by initial particle arrangement induced by capillary force resulting from particle surface tension and external force [41, 42]. Stage II starts from the sintering temperature of ~1430 °C and ends at 1700 °C, which is achieved by extensive particle arrangement. At temperature between 1430 °C and 1700 °C, slope of relative density-time curves (densification rate) is much higher than counterpart below 1430 °C, suggesting densification process is significantly accelerated. The accelerated densification is attributed to following reasons: firstly, liquid phase containing Y, Sc, O and Si with low melting point of ~1660 °C generates because SiO_2 present in surface of starting SiC powder reacts with sintering additive of Y_2O_3-Sc_2O_3 [28, 30, 31]. Secondly, the pulsed electrical field (~25 V/cm in this study calculated by dividing voltage into thickness of SiC compacts) in SPS was suggested to be able to enhance ion mobility and thus reduce viscosity of liquid phase sintering additive [43-45]. It was reported that the liquid phase exposed to the pulse electrical field could promote grain boundary sliding and result in extensive particle arrangement [43]. Even though high pulsed direct current of ~650 A at 1850 °C was adopted during SPS in this study, current mainly goes through graphite punches/dies rather than SiC compacts because SiC compacts have much higher electrical resistivity (~10^{-4} ohm•m) than that (~10^{-6} ohm•m) of graphite pieces used in SPS [14, 46]. As current goes through graphite pieces, Joule heat is generated and conducted to SiC compacts to achieve target sintering conditions. In other words, the sintering process is controlled by Joule heating and heat conduction from the graphite die to the powder compact. Given that slope of relative density-time curves (densification rate) during state II is independent of sintering temperature, it could be speculated that it is the formation of liquid phase with low melting point and positive role of electrical field in reducing viscosity of liquid phase that result in extensive particle arrangement in stage II. Stage III starts from around 1700 °C and ends at 1850 °C, which is achieved by contact-flattening

process. At sintering temperature of 1700 °C, slope of relative density-time curves (densification rate) begins to decrease and relative density is around 80%. During contact-flattening process, contact points/area between grains are exposed to large compressive stress originating from large capillary force and thus possess higher solubility in liquid phase than other areas without compressive stress. Consequently, these areas/points preferably dissolve into liquid phase followed by diffusion of dissolved solid atoms (e.g. Si and C) in liquid phase and final precipitation of solid atoms in regions away from contact points/areas. That process mainly causes densification via reducing distance between grain centers [41].

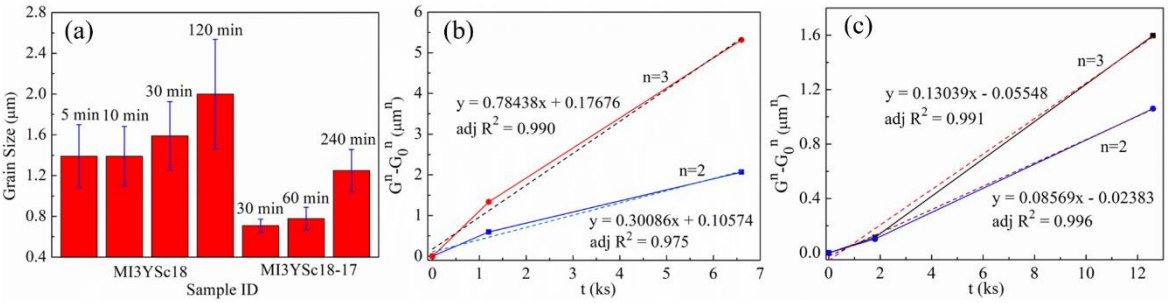

Figure 3. 14 Grain size of SiC ceramics sintered by SPS with 3 wt.% Y_2O_3-Sc_2O_3 as a function of holding time: (a) grain size of all SiC ceramics, left 4 columns correspond to final sintering temperature of 1850 °C and right 3 columns stands for final sintering temperature of 1750 °C; (b) fitting of grain size of the SiC ceramics sintered at final sintering temperature of 1850 °C; (c) fitting of grain size of the SiC ceramics sintered at final sintering temperature of 1750 °C. Solid lines are evolution of measured grain sizes as a function of holding time while dotted lines are fitting results according to measured grain size and equation 3.11. n=2 and n=3 means grain growth is interface-reaction controlling process and atom diffusion controlling process respectively.

Figure 3. 14 gives grain size evolution of spark plasma sintered SiC ceramics in isothermal period at different final sintering temperatures. A typical grain growth model in liquid phase sintering was used to evaluate grain growth mechanism, which is shown equation 3.11:

$$G^n - {G_0}^n = Kt \tag{3.11}$$

Here G, G_0, n, K, and t are grain size during isothermal period, initial grain size, value indicative of grain growth mechanism, grain growth rate constant and holding time respectively. As n is selected as 3, grain growth is controlled by process of atom diffusion in liquid phase. In contrast, as n is

selected as 2, grain growth is controlled by interface reaction process consisting of dissolution of small grains and reprecipitation on large grains [41].

Figure 3. 14(a) gives grain sizes of all SiC ceramics sintered for different holding times. Left 4 columns correspond to SiC ceramics sintered at final sintering temperature of 1850 °C for 5-120 min and right 3 columns stand for SiC ceramics sintered at final sintering temperature of 1750 °C for 30-240 min. Given that the SiC ceramic sintered at final sintering temperature of 1750 °C for 30min (labelled as MI3YSc18-17-30min) was firstly heated to 1850 °C and then decreased to 1750 °C, grain size (0.71 ± 0.06 μm) of this sample was chosen as initial value of the SiC ceramic sintered at final temperature of 1850 °C for zero holding time. It could be seen that at final sintering temperature of 1850 °C, grain growth can be distinguished by 3 stages: first stage (initial 5 min) corresponds to rapid grain growth from 0.71 ± 0.06 μm to 1.39 ± 0.31 μm; second stage (from 5 min to 10 min) corresponds to negligible grain growth and final stage (from 10 min to 120 min) corresponds to moderate grain growth from 1.39 ± 0.29 μm to 2.00 ± 0.54 μm. Such quick grain growth within initial 5 min of isothermal period at 1850 °C cannot be attributed to static Ostwald ripening process during which grain growth in liquid phase sintering process is slow, as reported by other researchers [47]. Similar rapid grain growth in initial few minutes of isothermal period during spark plasma sintering process was also reported by other researchers and was described as dynamic Ostwald ripening process [48, 49]. In the case of dynamic Ostwald ripening, liquid phase formed during heating process was far away from its thermodynamic equilibrium due to fast heating rate (100 °C/min in this study). Driving force originating from pushing non-thermodynamic equilibrium to thermodynamic equilibrium process leads to very rapid dissolution of small grains and generate momentary supersaturated liquid. The supersaturated liquid provides sufficient solid atoms for reprecipitation on large grain [48]. After rapid grain growth in initial few minutes, liquid phase approaches its thermodynamic equilibrium and static Ostwald ripening process dominates grain growth, which matches well with grain size evolution of the SiC ceramics sintered by SPS at final sintering temperature of 1850 °C (Figure 3. 14(a)). Overall, grain growth at final sintering temperature of 1850 °C is suggested to be achieved by dynamic ripening and subsequent static ripening while grain growth at final sintering temperature of 1750 °C is suggested to be achieved by static ripening.

Equation 3.11 is used to fit grain size data during static ripening process of spark plasma sintered SiC ceramics with 3 wt.% Y_2O_3-Sc_2O_3. Figure 3. 14(b) demonstrates fitting result on grain size data of the SiC ceramics sintered at final sintering temperature of 1850 °C. It is found that experimental data matches fitting result better as n is chosen as 3 (adjusted R^2: 0.990 versus 0.975), indicating grain growth in the SiC ceramics sintered at final sintering temperature of 1850 °C is controlled by atom diffusion process. Same approach is also used to fit grain size data during static ripening process of the SiC ceramics sintered at final sintering temperature of 1750 °C, as shown in Figure 3. 14(c). It is found that as n is chosen as 2, experimental data is better fitted (adjusted R^2: 0.996 versus 0.991) compared with the case where n is chosen as 3, suggesting that grain growth in the SiC ceramics sintered at final sintering temperature of 1750 °C is controlled by interface-reaction process [41]. Overall, grain growth mechanism during static ripening process is dependent on final sintering temperature.

3.3.4.2 Grain growth effects

It is well known that lower thermal conductivity of pure polycrystalline ceramics compared with counterpart of pure single crystal is attributed to additional phonon-grain boundary scattering [50]. Such scattering effect is reflected by a temperature discontinuity in grain boundary and described as grain boundary thermal resistance (a special type of interfacial thermal resistance) [51]. Furthermore, thermal conductivity dependence of pure polycrystalline ceramics on grain size could be quantitatively described by equation 2.5 in section 2.7.1 of chapter 2.

Grain boundary thermal resistance of pure polycrystalline SiC ceramics has been calculated by Molecular dynamic (MD) simulation and was found to range from 7 X 10^{-11} W^{-1}•m^2•K to 7 X 10^{-10} W^{-1}•m^2•K depending on misorientation angle of a grain boundary [52]. Furthermore, it was reported that grain boundary thermal resistance was affected by atomic configuration and element segregation in grain boundary [53-55]. For example, when a perfect grain boundary is replaced by a disordered grain boundary with same misorientation angle, grain boundary thermal resistance could be increased by at least 3 factors [53]. When a pure grain boundary is replaced by the interface (a glass phase containing Al, Y, O, Si and C), thermal resistance of the interface was around 8.87 X 10^{-9} W^{-}

^{1}•m^{2}•K [55]. For SiC ceramics sintered with 3 wt.% Y_2O_3-Sc_2O_3, HAADF and STEM-EDS results (Figure 3. 9, Figure 3. 10 and Figure 3. 11) has confirmed SiC grains are separated by the glass phase containing Y, Sc, Si and O which formed via dissolution of small SiC grains into liquid sintering additive. It could be speculated that thermal resistance of the sintering additive distributing in grain boundaries of SiC is in the order of 10^{-9} W^{-1}•m^{2}•K.

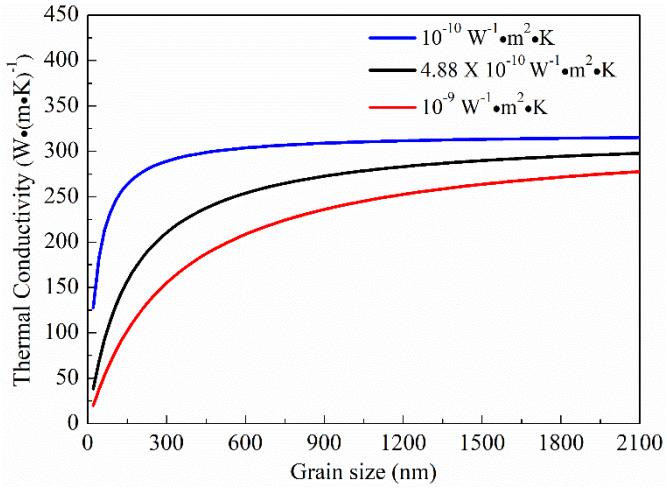

Figure 3. 15 Grain size effects on thermal conductivity of pure polycrystalline SiC ceramics based on equation 2.5. Thermal conductivity at room temperature of single crystal 3C-SiC in equation 2.5 is chosen as 320 W/(m•K) [38]. Lines with different colours stands for different grain boundary thermal resistance which are in same order as counterparts calculated by molecular dynamic simulation [52, 55].

Figure 3. 15 shows effects of grain size on thermal conductivity of pure polycrystalline SiC ceramics based on equation 2.5. The thermal conductivity of single crystal 3C-SiC at room temperature is chosen as 320 W/(m•K) and grain boundary thermal resistance is selected to be within the range of 10^{-10}~10^{-9} W^{-1}•m^{2}•K [38, 52, 55]. According to Figure 3. 15, thermal conductivity increases with grain size and increase rate depends on grain size and grain boundary thermal resistance. For a pure polycrystalline SiC ceramic, as grain boundary thermal resistance is 10^{-10} W^{-1}•m^{2}•K, increasing grain size from 1.39 ± 0.29 μm to 2.00 ± 0.54 μm results in 0.69% increase of thermal conductivity (from 313 W/(m•K) to 315 W/(m•K)). As grain boundary thermal resistance is selected as 10^{-9} W^{-1}•m^{2}•K, same increase of grain size (from 1.39 ± 0.29 μm to 2.00 ± 0.54 μm) results in 6.05% increase of thermal conductivity (from 260 W/(m•K) to 275 W/(m•K)). When comparing grain size and measured thermal conductivity of MI3YSc18-10min with counterparts of MI3YSc18-120min, same increase of

grain size (from 1.39 ± 0.29 μm to 2.00 ± 0.54 μm) results in 19.2% enhancement of thermal conductivity (from 112 ± 0.55 W/(m•K) to 133 ± 0.63 W/(m•K)). It can be found that same increase of grain size results in larger extent of thermal conductivity increase (19.2%) in those 2 sintered SiC ceramics than counterpart (6.05%) of pure polycrystalline SiC ceramics with grain boundary thermal resistance of 10^{-9} W^{-1}•m^2•K. Since the thermal conductivity increase of pure polycrystalline SiC ceramics obtained from Figure 3. 15 is only determined by larger grain size, other factors should make important contribution to the more obvious thermal conductivity increase in sintered SiC ceramics. In other words, reduced number of grain boundaries per unit volume is partially responsible for thermal conductivity increase of SiC ceramics sintered with Y_2O_3-Sc_2O_3.

It was reported that there was inborn oxygen dissolved in SiC lattice [56]. Presence of inborn oxygen in SiC lattice is accompanied by formation of Si vacancy and substitutional atom of O at C sites, as shown in the defect formation equation 3.12 [56].

$$SiO_2 \rightarrow Si_{Si} + 2O_C^{\bullet\bullet} + V_{Si}'''' \quad (3.12)$$

Where Si_{Si} means Si from dissolved SiO_2 inside SiC lattice occupies Si site in SiC lattice, $O_C^{\bullet\bullet}$ means that C site in SiC lattice is replaced by O and charge of this substitutional O is -2, and V_{Si}'''' means that Si vacancy with charge of +4 is formed due to electroneutrality inside SiC lattice doped with SiO_2.

The abovementioned point defects (V_{Si}'''' and $O_C^{\bullet\bullet}$) in SiC lattice could scatter high frequency phonons and lead to reduced thermal conductivity [57]. It is thus important to figure out lattice oxygen evolution during sintering process. It was found that as the rare-earth oxide (La_2O_3-Y_2O_3) was chosen as a sintering additive to fabricate dense SiC ceramics, lattice oxygen (1500 ppm) in the sintered SiC ceramic with La_2O_3-Y_2O_3 was lower than counterparts in starting SiC powders and acid-washed SiC powder [56]. Lower lattice oxygen content (5600 ppm) in the acid-washed SiC powder compared with that (9400 ppm) in starting SiC powder could be attributed to removal of SiO_2. The lowest lattice oxygen in the sintered SiC ceramic was attributed to effective role of rare-earth oxide in removing lattice oxygen of SiC. Removal of lattice oxygen in SiC during sintering process was proposed to be achieved by two steps: firstly, SiO_2 present on surface of starting SiC powder reacted with the

sintering additive (La_2O_3-Y_2O_3) and formed liquid phase containing Si, La, O and Y; secondly, inborn oxygen inside SiC lattice diffused outwards to the liquid phase and formed crystalline or amorphous silicates due to high thermodynamic affinity of rare-earth oxide [56]. Presence of crystalline phase La_2SiO_5 and $Y_2Si_2O_7$ verified above speculation.

In this study, the sintering additive (mixture of Y_2O_3-Sc_2O_3) could also remove lattice oxygen of SiC. Firstly, HAADF and STEM-EDS analysis (Figure 3. 9, Figure 3. 10 and Figure 3. 11) demonstrates that Si is detected in secondary phase distributing in triple points of sintered SiC ceramics, which suggests that SiO_2 reacts with Y_2O_3-Sc_2O_3 and thus form melt containing O, Si, Sc, and Y. It was reported that trivalent rare-earth cations (e.g. Y^{3+}, Sc^{3+} and La^{3+}) could occupy space in SiO_4^{4-} tetrahedra of the melt and act as a network modifier [36, 58-61]. Moreover, ability of rare-earth cations with regard to attracting O^{2-} in the melt is determined by the cation field strength (CFS) [62]. CFS is described in equation 3.13.

$$CFS = \frac{Z}{r^2} \tag{3.13}$$

Where Z and r stands for charge of rare-earth cation and distance between rare-earth cation and oxygen anion respectively. According to equation 3.13, lower charge and larger radius of rare-earth cation lead to lower CFS.

Considering La^{3+} has larger cation radius (117.2 pm) than counterparts of Sc^{3+} (88.5 pm) and Y^{3+} (104 pm) [36], the sintering additive (mixture of Y_2O_3-Sc_2O_3) adopted in this study possess higher CFS than counterpart of the sintering additive (mixture of La_2O_3-Y_2O_3) adopted in reference [56]. Hence, it is expected that Y_2O_3-Sc_2O_3 can attract more O^{2-} than that of La_2O_3-Y_2O_3 in melt and prevent reprecipitation of oxygen onto large grains.

Secondly, according to EDS results (Table 3. 6) carried out in triple points of the SiC ceramic sintered with Y_2O_3-Sc_2O_3 (labelled as MI3YSc18-10min), atom ratio of (Y+Sc)/O (between 0.203-0.302) is much smaller than counterpart (0.67) of raw sintering additive powders (mixture of Y_2O_3-Sc_2O_3 with molar ratio of 2:1). Given that Y cannot dissolve into SiC lattice due to significant radius difference between Y^{3+} (104 pm) and Si^{4+} (54 pm) and Sc has very small solubility limit (20-30 ppm at 1800-

2600 °C) in single crystal SiC [36, 37], evolution of the atom ratio of (Y+Sc)/O in triple points of sintered SiC ceramics is determined by variation of oxygen. Lower atom ratio in triple points of sintered SiC ceramics than counterparts in raw sintering additive powders (mixture of Y_2O_3-Sc_2O_3) further implies that oxygen originating from both silica present on surface of starting SiC powder and inborn oxygen in SiC lattice is restricted in triple points. Such restriction of oxygen by Y_2O_3-Sc_2O_3 and negligible doping of Y and Sc in SiC lattice mean that only Si and C atoms precipitate onto large grains. In other words, as mixture of Y_2O_3-Sc_2O_3 is adopted as a sintering additive, grain growth not only results in reduced number of grain boundary per unit volume but also results in lattice purification. Hence, it is suggested that reduced number of grain boundary per unit volume and lattice purification during grain growth are responsible for higher thermal conductivity of the SiC ceramic with larger grain size.

3.3.5 Conclusions

Dense SiC ceramics were fabricated by SPS at final sintering temperature of 1750-1850 ºC for 5-240 min with 3 wt.% mixture of Y_2O_3-Sc_2O_3 as a sintering additive. Thermal conductivity varies from 92 ± 0.49 W/(m•K) to 133 ± 0.63 W/(m•K). Effects of final sintering temperature and holding time on densification, grain growth and microstructure as well as correlations between microstructure and thermal conductivity have been discussed and conclusion can be achieved as follows:

(1) Increasing final sintering temperature and extending holding time have little influence on densification but change grain growth mechanism. At final sintering temperature of 1850 ºC, rapid grain growth from 0.71 ± 0.06 μm to 1.39 ± 0.31 μm (dynamic Ostwald ripening) takes place in initial 5 min followed by moderate grain growth from 1.39 ± 0.29 μm to 2.00 ± 0.54 μm (static Ostwald ripening) in rest 110 min of isothermal periods. At final sintering temperature of 1750 ºC, only static ripening is observed. Dominant grain growth mechanism during static ripening process changes from interface reaction at 1750 ºC to atom diffusion at 1850 ºC.

(2) Continuous sintering additive network is found in sintered SiC ceramics with Y_2O_3-Sc_2O_3 despite final sintering temperature and holding time employed.

(3) Eastman model was combined with experimental data to clarify correlation between grain growth and thermal conductivity. Results showed that grain growth of the SiC ceramics not only reduces

number of grain boundary per unit volume but also results in lattice purification (confirmed by STEM-EDS analysis), which is suggested to be responsible for higher thermal conductivity at larger grain size. The results indicate that the careful selection of sintering additives could further increase thermal conductivity of SiC ceramics.

References

[1] K.A. Terrani, Accident tolerant fuel cladding development: Promise, status, and challenges, Journal of Nuclear Materials 501 (2018) 13-30.

[2] R. Krishnarao, M.Z. Alam, D. Das, In-situ formation of SiC, ZrB_2-SiC and ZrB_2-SiC-B_4C-YAG coatings for high temperature oxidation protection of C/C composites, Corrosion Science 141 (2018) 72-80.

[3] Y.-W. Kim, S.H. Jang, T. Nishimura, S.-Y. Choi, S.-D. Kim, Microstructure and high-temperature strength of silicon carbide with 2000 ppm yttria, Journal of the European Ceramic Society 37(15) (2017) 4449-4455.

[4] P.A. Mouche, K.A. Terrani, Steam pressure and velocity effects on high temperature silicon carbide oxidation, Journal of the American Ceramic Society 103(3) (2020) 2062-2075.

[5] G.A. Slack, Thermal conductivity of pure and impure silicon, silicon carbide, and diamond, Journal of Applied physics 35(12) (1964) 3460-3466.

[6] M. Steen, L. Ranzani, Potential of SiC as a heat exchanger material in combined cycle plant, Ceramics international 26(8) (2000) 849-854.

[7] P. Tao, W. Liu, Y. Wang, Fabrication of two-layer SiC nanowire cladding tube with high thermal conductivity, Journal of the European Ceramic Society 40(9) (2020) 3399-3405.

[8] A. Marzoughi, R. Burgos, D. Boroyevich, Characterization and performance evaluation of the state-of-the-art 3.3 kV 30 A full-SiC MOSFETs, IEEE Transactions on Industry Applications 55(1) (2018) 575-583.

[9] K. Watari, H. Nakano, K. Sato, K. Urabe, K. Ishizaki, S. Cao, K. Mori, Effect of grain boundaries on thermal conductivity of silicon carbide ceramic at 5 to 1300 K, Journal of the American Ceramic Society 86(10) (2003) 1812-1814.

[10] K. Raju, D.-H. Yoon, Sintering additives for SiC based on the reactivity: a review, Ceramics International 42(16) (2016) 17947-17962.

[11] N.P. Padture, In situ-toughened silicon carbide, Journal of the American Ceramic Society 77(2) (1994) 519-523.

[12] G. Magnani, A. Brentari, E. Burresi, G. Raiteri, Pressureless sintered silicon carbide with enhanced mechanical properties obtained by the two-step sintering method, Ceramics International 40(1) (2014) 1759-1763.

[13] G. Magnani, G. Sico, A. Brentari, P. Fabbri, Solid-state pressureless sintering of silicon carbide below 2000° C, Journal of the European Ceramic Society 34(15) (2014) 4095-4098.

[14] S.H. Jang, Y.W. Kim, K.J. Kim, S.J. Lee, K.Y. Lim, Effects of Y_2O_3–RE_2O_3 (RE= Sm, Gd, Lu) Additives on Electrical and Thermal Properties of Silicon Carbide Ceramics, Journal of the American Ceramic Society 99(1) (2016) 265-272.

[15] S. Taguchi, F. Motta, R. Balestra, S. Ribeiro, Wetting behaviour of SiC ceramics: part II—Y_2O_3/Al_2O_3 and Sm_2O_3/Al_2O_3, Materials Letters 58(22-23) (2004) 2810-2814.

[16] K. Biswas, Liquid phase sintering of SiC-ceramics, Materials science Forum, Trans Tech Publ, (2009), 91-108.

[17] T. Kinoshita, S. Munekawa, Effect of grain boundary segregation on thermal conductivity of hot-pressed silicon carbide, Acta materialia 45(5) (1997) 2001-2012.

[18] D.-M. Liu, B.-W. Lin, Thermal conductivity in hot-pressed silicon carbide, Ceramics International 22(5) (1996) 407-414.

[19] G.-D. Zhan, M. Mitomo, A.K. Mukherjee, Effects of heat treatment and sintering additives on thermal conductivity and electrical resistivity in fine-grained SiC ceramics, Journal of materials research 17(9) (2002) 2327-2333.

[20] Y. Zhou, K. Hirao, Y. Yamauchi, S. Kanzaki, Effects of rare-earth oxide and alumina additives on thermal conductivity of liquid-phase-sintered silicon carbide, Journal of materials research 18(8) (2003) 1854-1862.

[21] Y.K. Seo, Y.W. Kim, T. Nishimura, W.S. Seo, High thermal conductivity of spark plasma sintered silicon carbide ceramics with yttria and scandia, Journal of the American Ceramic Society 100(4) (2017) 1290-1294.

[22] Y. Zhou, K. Hirao, K. Watari, Y. Yamauchi, S. Kanzaki, Thermal conductivity of silicon carbide densified with rare-earth oxide additives, Journal of the European Ceramic Society 24(2) (2004) 265-270.

[23] Y.W. Kim, K.Y. Lim, W.S. Seo, Microstructure and thermal conductivity of silicon carbide with yttria and scandia, Journal of the American Ceramic Society 97(3) (2014) 923-928.

[24] Y.-W. Kim, S. Kultayeva, J. Sedláček, O. Hanzel, P. Tatarko, Z. Lenčéš, P. Šajgalík, Thermal and electrical properties of additive-free rapidly hot-pressed SiC ceramics, Journal of the European Ceramic Society 40(2) (2020) 234-240.

[25] P. Šajgalík, J. Sedláček, Z. Lenčéš, J. Dusza, H.-T. Lin, Additive-free hot-pressed silicon carbide ceramics—A material with exceptional mechanical properties, Journal of the European Ceramic Society 36(6) (2016) 1333-1341.

[26] T. Yamamoto, H. Kitaura, Y. Kodera, T. Ishii, M. Ohyanagi, Z.A. Munir, Consolidation of nanostructured β-SiC by spark plasma sintering, Journal of the American ceramic Society 87(8) (2004) 1436-1441.

[27] S. Ge, X. Yao, Y. Liu, H. Duan, Z. Huang, X. Liu, Effect of Sintering Temperature on the Properties of Highly Electrical Resistive SiC Ceramics as a Function of Y_2O_3-Er_2O_3 Additions, Materials 13(21) (2020) 4768.

[28] C.T. Horovitz, Scandium its occurrence, chemistry physics, metallurgy, biology and technology, Elsevier (2012).

[29] M.I. Mendelson, Average grain size in polycrystalline ceramics, Journal of the American Ceramic society 52(8) (1969) 443-446.

[30] M. Hnatko, P. Šajgalík, Z. Lenčéš, D. Salamon, F. Monteverde, Carbon reduction reaction in the Y_2O_3–SiO_2 glass system at high temperature, Journal of the European Ceramic Society 21(16) (2001) 2797-2801.

[31] E.M. Levin, C.R. Robbins, H.F. McMurdie, PHASE DIAGRAMS FOR CERAMISTS: 1969 SUPPLEMENT, (1969).

[32] T. Grande, H. Sommerset, E. Hagen, K. Wiik, M.A. Einarsrud, Effect of weight loss on liquid-phase-sintered silicon carbide, Journal of the American Ceramic Society 80(4) (1997) 1047-1052.

[33] H. Tanaka, Silicon carbide powder and sintered materials, Journal of the ceramic society of Japan 119(1387) (2011) 218-233.

[34] H. Xu, T. Bhatia, S.A. Deshpande, N.P. Padture, A.L. Ortiz, F.L. Cumbrera, Microstructural evolution in liquid-phase-sintered SiC: part I, effect of starting powder, Journal of the American Ceramic Society 84(7) (2001) 1578-1584.

[35] S.-J.L. Kang, Sintering: densification, grain growth and microstructure, Elsevier (2004).

[36] R.D. Shannon, Revised effective ionic radii and systematic studies of interatomic distances in halides and chalcogenides, Acta crystallographica section A: crystal physics, diffraction, theoretical and general crystallography 32(5) (1976) 751-767.

[37] Y.M. Tairov, I. Khlebnikov, V. Tsvetkov, Investigation of silicon carbide single crystals doped with scandium, physica status solidi (a) 25(1) (1974) 349-357.

[38] L.L. Snead, T. Nozawa, Y. Katoh, T.-S. Byun, S. Kondo, D.A. Petti, Handbook of SiC properties for fuel performance modeling, Journal of nuclear materials 371(1-3) (2007) 329-377.

[39] M. Bockstedte, A. Mattausch, O. Pankratov, Solubility of nitrogen and phosphorus in 4 H-SiC: A theoretical study, Applied physics letters 85(1) (2004) 58-60.

[40] X. Qian, P. Jiang, R. Yang, Anisotropic thermal conductivity of 4H and 6H silicon carbide measured using time-domain thermoreflectance, Materials Today Physics 3 (2017) 70-75.

[41] R.M. German, P. Suri, S.J. Park, Review: liquid phase sintering, J. Mater. Sci 44(1) (2009) 1-39.

[42] W. Kingery, Densification during sintering in the presence of a liquid phase. I. Theory, Journal of Applied Physics 30(3) (1959) 301-306.

[43] H. Peng, D. Salamon, J. Bill, G. Rixecker, Z. Burghard, F. Aldinger, Z. Shen, Consolidating and deforming SiC nanoceramics via dynamic grain sliding, Advanced Engineering Materials 9(4) (2007) 303-306.

[44] Z. Shen, H. Peng, M. Nygren, Formidable increase in the superplasticity of ceramics in the presence of an electric field, Advanced materials 15(12) (2003) 1006-1009.

[45] J. Gonzalez-Julian, O. Guillon, Effect of electric field/current on liquid phase sintering, Journal of the American Ceramic Society 98(7) (2015) 2018-2027.

[46] Z. Munir, U. Anselmi-Tamburini, M. Ohyanagi, The effect of electric field and pressure on the synthesis and consolidation of materials: A review of the spark plasma sintering method, Journal of materials science 41(3) (2006) 763-777.

[47] T.-Y. Cho, Y.-W. Kim, Effect of grain growth on the thermal conductivity of liquid-phase sintered silicon carbide ceramics, Journal of the European Ceramic Society 37(11) (2017) 3475-3481.

[48] Z. Shen, Z. Zhao, H. Peng, M. Nygren, Formation of tough interlocking microstructures in silicon nitride ceramics by dynamic ripening, Nature 417(6886) (2002) 266-269.

[49] H. Peng, Z. Shen, M. Nygren, Formation of in situ reinforced microstructures in α-sialon ceramics: Part III. Static and dynamic ripening, Journal of materials research 19(8) (2004) 2402-2409.

[50] A. Collins, M.A. Pickering, R.L. Taylor, Grain size dependence of the thermal conductivity of polycrystalline chemical vapor deposited β‐SiC at low temperatures, Journal of applied physics 68(12) (1990) 6510-6512.

[51] H.-S. Yang, G.-R. Bai, L. Thompson, J. Eastman, Interfacial thermal resistance in nanocrystalline yttria-stabilized zirconia, Acta Materialia 50(9) (2002) 2309-2317.

[52] J.-P. Crocombette, L. Gelebart, Multiscale modeling of the thermal conductivity of polycrystalline silicon carbide, Journal of Applied Physics 106(8) (2009) 083520.

[53] D. Spiteri, J. Anaya, M. Kuball, The effects of grain size and grain boundary characteristics on the thermal conductivity of nanocrystalline diamond, Journal of Applied Physics 119(8) (2016) 085102.

[54] N. Goel, E. Webb III, A. Oztekin, J. Rickman, S. Neti, Kapitza resistance at segregated boundaries in β-SiC, Journal of Applied Physics 118(11) (2015) 115101.

[55] X. Dong, Y.C. Shin, Multiscale genome modeling for predicting the thermal conductivity of silicon carbide ceramics, Journal of the American Ceramic Society 99(12) (2016) 4073-4082.

[56] Y. Zhou, K. Hirao, Y. Yamauchi, S. Kanzaki, Effects of rare-earth oxide and alumina additives on thermal conductivity of liquid-phase-sintered silicon carbide, Journal of materials research 18(08) (2003) 1854-1862.

[57] P. Klemens, The scattering of low-frequency lattice waves by static imperfections, Proceedings of the Physical Society. Section A 68(12) (1955) 1113.

[58] A. Dietzel, The cation field strengths and their relation to devitrifying processes, to compound formation and to the melting points of silicates, Z. Elektrochem. Angew. Phys. Chemie 48 (1942) 9-23.

[59] X. Zhang, Y. Yue, H. Wu, Effects of cation field strength on structure and properties of boroaluminosilicate glasses, Materials Research Innovations 17(3) (2013) 212-217.

[60] E.I. Morin, J. Wu, J.F. Stebbins, Modifier cation (Ba, Ca, La, Y) field strength effects on aluminum and boron coordination in aluminoborosilicate glasses: the roles of fictive temperature and boron content, Applied Physics A 116(2) (2014) 479-490.

[61] A.S. Hakeem, Novel route of oxynitride glass synthesis and characterisation of glasses in the Ln-Si-ON and Ln-Si-Al-ON systems, Institutionen för fysikalisk kemi, oorganisk kemi och strukturkemi, (2007).

[62] M. Kitayama, K. Hirao, K. Watari, M. Toriyama, S. Kanzaki, Thermal conductivity of β-Si3N4: III, effect of rare-earth (RE= La, Nd, Gd, Y, Yb, and Sc) oxide additives, Journal of the American Ceramic Society 84(2) (2001) 353-58.

3.4 Article III: Effects of proton irradiation on thermal conductivity of spark plasma sintered SiC Ceramics

Contributions:

Zhenfei Chai conceived the idea and methodology, fabricated SiC ceramics, carried out most of the irradiation and characterization experiments. Moreover, **Zhenfei Chai** analyzed all of the experimental results and wrote the article. **Dr. Han Liu** provided the TEM image (figure 3.21) and useful advice on XRD analysis. **Dr. Gyorgyi Glodan** helped with spark plasma sintering experiments. **Prof. Ping Xiao** funded the work and gave useful suggestions on presenting experimental results. The article has been internally reviewed by **Dr. Han Liu** and **Prof. Ping Xiao.**

Effects of proton irradiation on thermal conductivity of spark plasma sintered SiC Ceramics

Zhenfei Chai[1], Han Liu[1], Gyorgyi Glodan[2], Ping Xiao[1,*]

[1] *Department of Materials, University of Manchester, Manchester UK, M13 9PL, UK*

[2] *Dalton Cumbrian Facility, University of Manchester, Westlakes Science & Technology Park, Moor Row, Cumbria CA24 3HA, UK*

Abstract: In this study, dense SiC ceramics (relative density of 93%) were fabricated by spark plasma sintering (SPS) and subsequently exposed to proton irradiation at irradiation temperature of 340 °C and damage level of 0.05, 0.10 and 0.25 displacements per atom (dpa). Evolution of microstructure and thermal conductivity after proton irradiation were investigated. The unit cell volume expansion (0.47%-1.41%) and significant thermal conductivity reduction (79.9%-95% lower than that of unirradiated SiC) after proton irradiation were verified by X-ray diffraction (XRD) and laser flash technique respectively. Such volume expansion and thermal conductivity degradation have been correlated with point defects (i.e. vacancy-type defects and interstitial-type defects) and interstitial clusters induced by proton irradiation. It is suggested that interstitial-type defects make dominant contribution to unit cell volume expansion while vacancy-type defects and interstitial clusters are responsible for significant thermal conductivity degradation. Furthermore, higher damage level led to higher volume expansion and lower thermal conductivity but the degree of variability of the volume expansion and thermal conductivity at high damage level of 0.10-0.25 dpa was smaller than counterparts at low damage level of 0.05-0.10 dpa, which is suggested to be caused by more contribution from interstitial clusters at high damage level.

Key words: SiC; SPS; proton irradiation; thermal conductivity degradation; unit cell volume expansion.

3.4.1 Introduction

Cubic SiC (3C-SiC) ceramic and SiC fiber-reinforced SiC matrix composites (SiC_f/SiC composites) have been regarded as very promising candidates to replace current Zr alloy as cladding materials in nuclear fusion and fission reactors because of low thermal neutron absorption cross section, high

thermal conductivity (320 W/(m•K) for 3C-SiC), excellent high temperature mechanical performance, good radiation resistance, and high oxidation resistance in air and steam [1-5]. When SiC was irradiated by high energy neutrons in nuclear reactors, large amount of point defects and/or defect clusters generated. Although some point defects were annihilated during irradiation process via recombination of interstitial and corresponding vacancy, accumulation of residual defects or defect clusters could still lead to severe microstructure evolution (e.g. crystalline to amorphous transformation and swelling) and performance degradation (e.g. degradation of thermal conductivity) [6-8]. Thermal conductivity of cladding materials is a critical factor determining heat transfer from nuclear fuel pellet to surrounding coolant in nuclear reactors. Hence, it is both theoretically and practically significant to figure out evolution of microstructure and thermal conductivity of SiC served in nuclear reactors.

Although special test reactors could provide similar neutron flux and energy spectrum to counterparts in commercial nuclear reactors and have been used to conduct irradiation research, limited number of test reactors, too long irradiation time and high activity of neutron-irradiated materials severely hindered meaningful and comprehensive study of irradiation damage on materials [9]. Alternatively, ion irradiation (e.g. proton, He ion and heavy ion) was developed to emulate neutron irradiation influence on material microstructure and properties from 1960s [10]. Compared with neutron irradiation, irradiation time required for achieving same damage level could be reduced by 2-4 orders of magnitude due to much higher damage rate of ion irradiation [9]. Also, activity of ion-irradiated materials is much lower compared with that of neutron-irradiated materials [9]. Furthermore, it is more feasible to adopt proton than heavy ion (e.g. silicon ion and carbon ion) for simulating neutron irradiation effects on microstructure and property evolution of SiC ceramics because a larger penetration depth and more uniform damage profile could be generated via proton irradiation [11-13].

During neutron or ion irradiation of SiC ceramics, different types of point defects (e.g. Si/C interstitial, Si/C vacancy and antisite defects) and defect clusters (e.g. black spot defects and dislocation loop) could form after cascade displacement damage [14-16]. Type, size and density of irradiation induced

defects in CVD-SiC are determined by irradiation temperature and damage level. High irradiation temperature and high damage level generally led to growth of lattice defects accompanied by amorphization and/or swelling of crystalline SiC [3]. Hu et al. investigated vacancy-type defects in neutron irradiated 3C-SiC using Positron annihilation spectroscopy. It was found that the neutral or negatively charged vacancy-type defects made very minor contribution to swelling (volume expansion) [17]. Sprouster et al. studied microstructure evolution of neutron irradiated 3C-SiC via the advanced synchrotron-based X-ray diffraction characterization. It was reported that SiC irradiated at damage level of 0.11 and 1.0 dpa had largest volume expansion caused by a high density of irradiation induced defects/defect clusters (i.e. black spots, vacancies, and small cluster defects) [18]. But the importance of these defects in swelling remains to be unsolved.

Thermal conductivity evolution of SiC ceramics after irradiation has also been investigated [6, 19, 20]. For instance, significant reduction of thermal conductivity at room temperature from 245 W/(m•K) to 30 W/(m•K) was observed after CVD-SiC was irradiated by neutron at low damage level of 0.01 dpa and low irradiation temperature of 60 °C, which was attributed to increased phonon-vacancy scattering [6]. However, role of interstitial clusters and antisite defects in thermal conductivity degradation remains unclear.

Currently, there are very limited reports about proton irradiation on sintered SiC ceramics. It is not clear whether proton irradiation is comparable to neutron irradiation in terms of microstructure and property evolution. Considering great difficulty to sinter dense SiC ceramic due to its extremely low self-diffusion coefficient and high degree of covalence (~88%), SPS has been adopted to fabricate dense SiC ceramics due to its advantages of lower sintering temperature, higher heating rate and shorter holding time compared with counterparts of conventional sintering techniques [21-23]. In this study, SiC ceramics were fabricated by SPS at 1850 °C with nano SiC powders and then exposed to proton irradiation at common service temperature (~340 °C) of pressurized water reactor and different damage levels. The main objectives of this study are to investigate evolution of microstructure and thermal conductivity of sintered SiC ceramics after proton irradiation and figure

out underlying mechanism for the evolution. Results from this study may provide useful information for comparing proton irradiation with neutron irradiation in SiC.

3.4.2 Experimental Methods

3.4.2.1 Sample fabrication and irradiation

3.4.2.1.1 SiC ceramics sintered by SPS

The β-SiC powders (45-55 nm, purity 97.5%, Nanostructured & Amorphous Materials, Inc.) were loaded into a graphite die with diameter of 12.7 mm and compressed using corresponding graphite punches. Graphite foils were used among all contact areas of graphite pieces and powders for easy removal of the sintered pellet. Thermopyrometer was used to monitor temperature of a pre-drilled hole of graphite die which is about 3.15 mm away from the boundary between SiC pellet and graphite die. It should be mentioned that the liquid phase sintering additive was not used to sinter SiC ceramics because of following reasons: (a) the sintering additive irradiated by high energy proton could generate unstable isotopes with long half-life, which significantly increases the time and difficulty to safely conduct subsequent characterization work. For the proton irradiated SiC ceramics containing Al_2O_2-Y_2O_3, more than 1 year are required to receive the irradiated SiC with sufficiently low radioactivity; (b) In terms of practical nuclear application, the liquid phase sintering additive could reduce irradiation resistance and weaken oxidation/corrosion resistance [24-27]; (c) Main objective of article III is to study proton irradiation on SiC and the adoption of liquid phase sintering additive may distract the focus of this article.

The SPS machine (DCS 10-4, Thermal Technology, GT Advanced Technology) with pulsed direct current (maximum voltage and current are 10 V and 4000 A respectively) was used to fabricate SiC ceramics. Heating/cooling rate, sintering temperature and holding time were chosen as 100 °C/min, 1850 °C and 10 min respectively. Besides, vacuum atmosphere (around 5 Pa) was used. Initial uniaxial pressure of 20 MPa was applied to powders before 600 °C to ensure good electrical contact between electrode and graphite pieces. The pressure was then gradually increased to 60 MPa during

which the temperature was increased from 600 °C to 1550 °C, and released to 20 MPa in the end of isothermal period.

3.4.2.1.2 Proton irradiation on SiC ceramics

Prior to proton irradiation, spark plasma sintered SiC ceramics with diameter of 12.7 mm and thickness of around 1.5 mm were ground by diamond pad with grit size of 35 μm and then successively polished by diamond paste with grit size of 6 μm, 1 μm, and 0.25 μm. Polished SiC ceramics were subsequently irradiated by 2.5 MeV proton at irradiation temperature of 340 °C in Dalton Cumbrian Facility (DCF), Cumbria, UK.

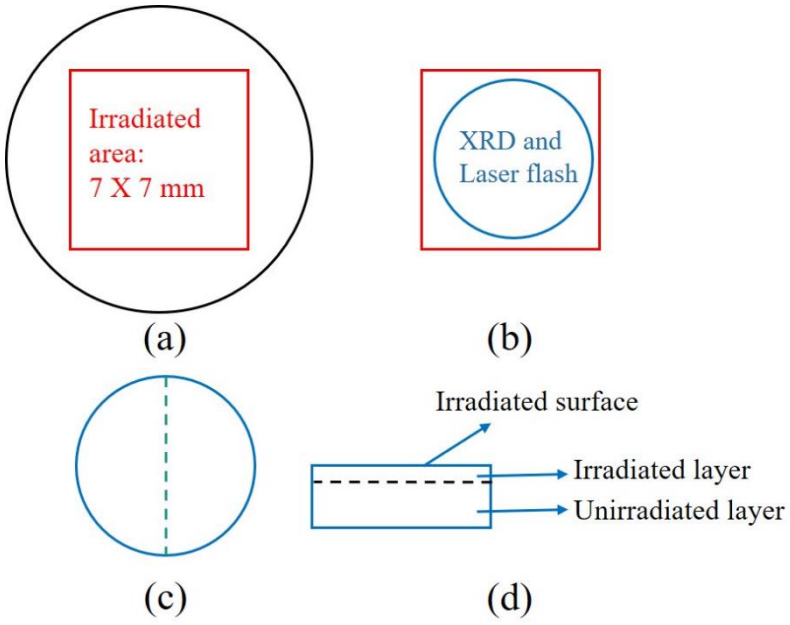

Figure 3. 16 A schematic diagram about preparation of irradiated SiC ceramics for different characterization: (a) selected irradiated area (7 X 7 mm) in a sintered SiC disk with diameter of 12.7 mm; (b) an irradiated SiC disk with diameter of 6 mm is cut from the irradiated SiC cuboid and characterized by XRD and laser flash technique to get lattice parameter and thermal conductivity respectively. (c) the irradiated SiC disk was cut into 2 pieces by laser cutting technique to get cross section; (d) cross section of irradiated SiC disk consisting of irradiated layer and unirradiated layer is used to prepare thin lamellas by focused ion beam (FIB).

Figure 3. 16(a) shows irradiated area (7 X 7 mm) in a sintered SiC disk with diameter of 12.7 mm. Beam current was chosen as 15 μA. Three damage levels of 0.05, 0.10 and 0.25 dpa were achieved in this study. Damage profile in proton-irradiated SiC ceramics along penetration direction was

calculated by Stopping and Range of Ions in Materials (SRIM) at selected current and beam energy [28]. Displacement threshold energy for Si and C during SRIM calculation was chosen as 35 eV and 20 eV respectively [29]. The SRIM output has the unit of displacements per Ångstrom-ion and been used to calculate damage rate with unit of dpa/s via equation 3.14 [10].

$$D = disp_{\text{Å}-ion}\frac{I*m*10^{8}}{A*e*\rho*N_{Av}} \tag{3.14}$$

Where D and $disp_{\text{Å}-ion}$ are the damage rate with unit of dpa/s and SRIM output with unit of displacements per Ångstrom-ion respectively. I, m, A, ρ, e and N_{Av} are beam current (1.5 X 10^{-5} A), mean mass number of 40 amu for SiC, irradiated area (0.49 cm^2) , mass density of 3.21 g/cm^3 for SiC, elementary charge of 1.6 X 10^{-19} C and Avogadro's number of 6.02 X 10^{23} mol^{-1} respectively.

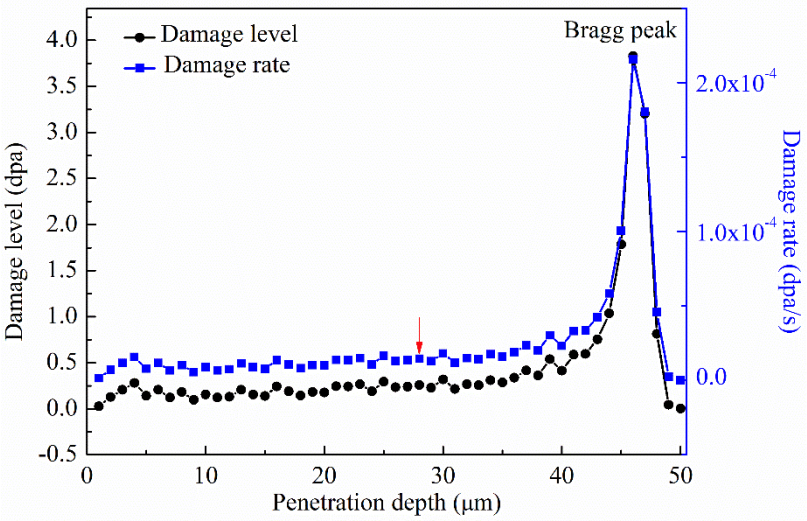

Figure 3. 17 The representative damage profile of pure SiC calculated by SRIM and equation 3.14 under below irradiation conditions: 2.5 MeV proton with current of 15 μA and target damage level of 0.25 dpa. Red arrow indicates the selected damage rate at which penetration depth is 60% of central position of Bragg peak. Total irradiation time for target damage levels are calculated based on the selected damage rate.

Figure 3. 17 shows the calculated damage profile of pure SiC irradiated by 2.5 MeV proton at target damage level of 0.25 dpa. Left vertical axis stands for damage level of the proton irradiated SiC. Horizontal axis and right vertical axis stand for penetration depth (μm) and damage rate (dpa/s) respectively. According to Figure 3. 17, damage profile consists of plateau part with nearly constant damage rate and shallow Bragg peak with much higher damage rate. Central position of Bragg peak in the damage profile is defined as the penetration depth at which highest damage rate is obtained

and total irradiation time for achieving target damage level is calculated based on the damage rate (marked by red arrow) at which the penetration depth is 60% of central position of Bragg peak [10].

3.4.2.2 Characterization

3.4.2.2.1 Density, composition and microstructure

Densities of sintered SiC ceramics prior to irradiation were measured by Archimedes principle in an analytical balance with the accuracy of 1 mg. Theoretical density of SiC is selected as 3.21 g/cm^3. The square irradiated areas (7 X 7 mm) in sintered SiC ceramics were cut into disks with diameter of ~6 mm by laser cutting machine (3D-Micromac‘s microPREPTM 1.1) for subsequent analysis by XRD and laser flash technique, as shown in Figure 3. 16(b).

Lattice parameter of the as-cut irradiated SiC disk (Figure 3. 16(b)) consisting of irradiated layer and unirradiated layer was characterized by grazing incidence X-ray diffractometer (GIXRD, Philips X’PERT) with Cu Kα radiation (λ = 0.15406 nm). Considering that thickness of irradiated layer is the penetration depth of ~46 μm in SiC ceramics exposed to current irradiated conditions (Figure 3. 17), incidence angle of 8° is selected and resultant penetration depth of X-ray could be around 23.5 μm in irradiated SiC disk according to equation 3.15.

$$t = \frac{3.45 * \sin \omega}{\frac{\mu}{\rho} * \rho_{bulk}} \quad (3.15)$$

Where t, ω, ρ_{bulk} and $\frac{\mu}{\rho}$ are penetration depth of X-ray in SiC (μm), incidence angle (º), density of bulk SiC ceramic and mass absorption coefficient of SiC that is dependent on sample composition and wavelength of used X-ray respectively.

Irradiated SiC disks were also cut into two parts by laser cutting machine (3D-Micromac‘s microPREPTM 1.1) to prevent spalling of thin irradiated layer, as shown in Figure 3. 16(c). As-cut cross section was cold mounted by resin to protect thin irradiated layer during subsequent grinding and polishing process. Grinding and polishing process were completed by above mentioned procedures. Focused ion beam (FIB, FEI Quanta 3D FIB) was used to prepare thin lamellas from cross section of irradiated SiC disks. The lamellas were characterized by transmission electron

microscopy (TEM, FEI Tecnai TF30). TEM images were used to get average intercept size via the line intercept method which was then converted into average grain size based on an assumption that grains have tetrakaidekahedral shape and their sizes follow log-normal distribution [30]. More than 200 grains are measured to get mean grain size of sintered SiC ceramics.

3.4.2.2.2 Thermal conductivity

Laser flash technique (LFA 427 on 18-414/4, NETZSCH GmbH) was used to measure thermal diffusivity at 30 °C of above mentioned sintered SiC disks with diameter of 12.7 mm and as-cut irradiated SiC disks with diameter of 6 mm under 1 bar Argon atmosphere. Thin graphite coating was sprayed on sample surfaces prior to thermal diffusivity measurement. Thermal diffusivity (α) can be calculated according to equation 3.2 [31].

Specific heat (C_p) of sintered SiC ceramic without any sintering aid is reported to be 0.683 J•(g•K)$^{-1}$ at 30 °C [32]. It is noted that specific heat showed negligible change (<2%) after irradiation [33]. Thus, specific heat of 0.683 J•(g•K)$^{-1}$ at 30 °C is adopted for irradiated SiC disks. Also, it was reported that density variation after neutron irradiation at 400 °C and damage level of 0.5 dpa is around 1.5% [3]. Such small density variation after irradiation is also verified in this study and has little influence thermal conductivity. Thermal conductivities (k) could be obtained according to equation 3.3.

To get thermal conductivity of irradiated layer in the as-cut irradiated SiC disk (Figure 3. 16(b)), a serial model was used. A serial model describes thermal conductivity of a composite consisting of 2 slabs in a serial configugation which are vertical to direction of heat flow. Two assumptions were made in a serial model: a. one dimensional heat flow from bottom surface to top surface takes place and no heat loss occurs in other directions; b. interfacial thermal resistance between unirradiated layer and irradiated layer is neligible [34]. Mathematic form of a serial model is shown in equation 3.16 in which volume fraction of irradiated layer is replaced by ratio between thickness of the irradiated layer and irradiated SiC disk because irradiated layer and corresponding irradiated SiC disk have same area [34]. Equation 3.16 can be converted to equation 3.17 by replacing thermal conducitivty with thermal diffusivitty due to negligible variation of specific heat and density after irradiation.

$$\frac{1}{K_d} = \frac{1}{K_u} + \frac{t_i}{t_d} * (\frac{1}{K_i} - \frac{1}{K_u}) \quad (3.16)$$

$$\frac{1}{\alpha_d} = \frac{1}{\alpha_u} + \frac{t_i}{t_d} * (\frac{1}{\alpha_i} - \frac{1}{\alpha_u}) \quad (3.17)$$

Where K_d, K_u, and K_i are thermal conductivity of irradiated SiC disk, the unirradiated SiC layer and irradiated SiC layer respectively; α_d, α_u, and α_i are thermal diffusivity of irradiated SiC disk, the unirradiated SiC layer and irradiated SiC layer respectively; t_d and t_i are thickness of the irradiated SiC disk and irradiated SiC layer respectively. Based on equation 3.16 and 3.17, thermal conductivity of irradiated SiC layer could be obtained.

To improve accuracy of the derived thermal conductivity of irradiated layer, the unirradiated layer of as-cut irradiated SiC disk was ground to different thicknesses while thickness of irradiated layer keeps constant (~46 μm). Thermal diffusivities of irradiated SiC disks with different thicknesses were measured by laser flash technique. Based on those thermal diffusivities of irradiated SiC disks with different thickness and linear relation between $\frac{1}{\alpha_d}$ and $\frac{1}{t_d}$ (as shown in Equation 3.17), one can carry out linear fitting of $\frac{1}{\alpha_d}$ - $\frac{1}{t_d}$ to get slope and intercept that can be utilized to derive thermal diffusivity/conductivity of irradiated SiC layer.

3.4.3 Results

3.4.3.1 Phase composition and microstructure

Physical property (e.g. density and grain size) and thermal property (e.g. thermal diffusivity and conductivity) of SiC ceramics sintered by SPS are listed in Table 3. 7. Concerning sample ID, NA18 stands for SiC ceramics sintered by SPS at 1850 ºC for 10 min under uniaxial pressure of 60 MPa using nano SiC as starting powder; 1, 2 and 3 stand for 3 SiC specimens fabricated at same conditions which are subsequently exposed to proton irradiation at damage level of 0.05, 0.10 and 0.25 dpa respectively.

Table 3. 7 Physical and thermal properties of SiC ceramics sintered by SPS at 1850 ºC for 10 min using nano SiC as starting powder.

Sample ID*	Density (g/cm^3)	Relative density** (%)	Grain Size (nm)	Thermal diffusivity (mm^2/s)	Thermal conductivity (W/(m•K))
NA18-1	3.01	93.9		66.9 ± 0.218	138 ± 0.449
NA18-2	3.00	93.6	475 ± 78.8	68.9 ± 0.334	142 ± 0.685
NA18-3	2.99	93.2		70.4 ± 0.143	143 ± 0.292

Note: (1) * NA18 stands for SiC ceramics sintered by SPS at 1850 ºC using nano SiC as starting powder; the number of 1, 2 and 3 after NA18 stands for three SiC ceramics fabricated at same conditions which are subsequently exposed to proton irradiation at damage level of 0.05, 0.10 and 0.25 dpa respectively; (2) ** relative density is obtained by dividing measured density over the theoretical density (3.21 g/cm^3) of SiC ceramics.

According to Table 3. 7, SiC ceramics with relative density of ~93.6% can be obtained by SPS at 1850 ºC for 10 min under uniaxial pressure of 60 MPa without any sintering aid. The sintering condition of SPS required for densifying SiC ceramics is less severe than counterparts of other sintering techniques [35-38]. It was reported that pure SiC ceramics with very low relative density

(~70%) was obtained by hot pressing sintering technique at 2150 ºC under uniaxial pressure of 25 MPa [38]. Such enhanced densification of SPS might be related to its unique features (e.g. pulsed electric field and high heating rate). High heating rate results in quick pass of low-temperature regions at which surface diffusion takes place and leads to particle coarsening. Larger particle size generally results in smaller driving force for densification [37]. Hence, high heating rate of SPS could keep larger driving force for densification to high temperature and increases densification rate. In addition, although high pulsed direct current of ~950 A at 1850 °C was adopted during SPS in this study, current mainly went through graphite punches/dies rather than the SiC compacts because the SiC compacts without sintering additive had much higher electrical resistivity (~10^{-3} ohm•m) than that (~10^{-6} ohm•m) of graphite pieces used in SPS [39, 40]. In other words, pulsed current in SPS mainly went through graphite dies to generate Joule heat and thus mainly affect sintering temperature and heating rate. Pulsed electric field (~27 V/cm in this study calculated by dividing voltage over thickness of SiC compacts) is present on SiC compacts but interaction between pulsed electric field and densification of SiC compacts without any sintering additive is not clear.

Figure 3. 18(a) shows GIXRD spectra of unirradiated SiC layer and irradiated SiC layer at different damage levels. As mentioned in section 3.4.2.2.1, penetration depth of X-ray in SiC is around 23.5 μm below irradiated surface, which was calculated using equation 3.15 in which the experimental density (~3.00 g/cm^3) of sintered SiC ceramics was used. Figure 3. 17 demonstrates damage profile of SiC ceramics irradiated by protons in the selected beam energy and current. It should be noted theoretical density (~3.21 g/cm^3) of SiC was selected when SRIM and equation 3.14 were used to get the damage profile. Firstly, SRIM simulates the collision among the incident high-energy ion and atoms inside matter (lattice) without considering pore effects. In the sintered SiC ceramics, pores distribute either in triple/multiple junctions of SiC grains or sample surface and are hardly present inside SiC lattice. Also, only isolated pores are present in sintered SiC ceramics because of low porosity (~6.4%). It is thus suggested that the small amount of pores (porosity of ~6.4%) have negligible effects on the SRIM output which determines the basic characteristics (i.e. shape, position of Bragg peak, maximum penetration depth) of damage profile. Figure 3. 19 shows the cross section of proton irradiated SiC disk at the damage level of 0.25 dpa and irradiation temperature of 340 ºC

characterized via optical microscopy. According to Figure 3. 19, there is a clear boundary between irradiated SiC layer and unirradiated layer and thickness of irradiated SiC layer is around 46 μm.

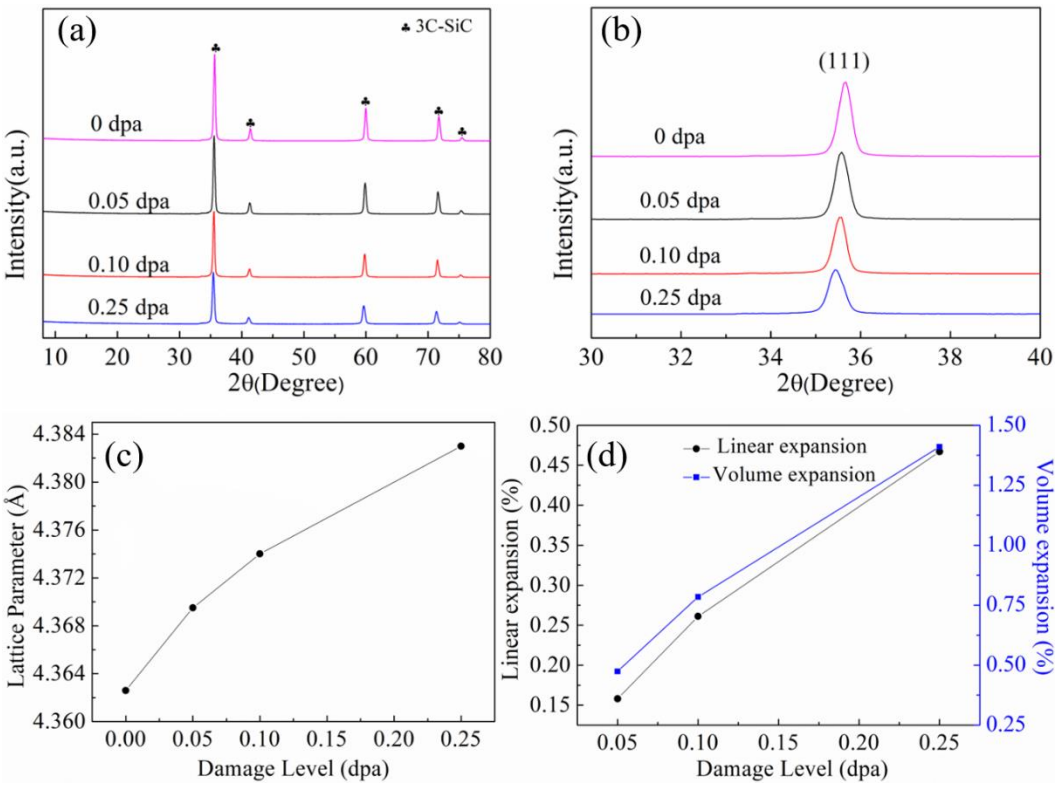

Figure 3. 18 GIXRD spectra (incidence angle of 8°), lattice parameter and unit cell expansion of irradiated SiC disks as a function of damage level: (a) GIXRD spectra of unirradiated SiC layer and irradiated SiC layer at different damage levels; (b) main peak corresponding to the lattice plane (111) in GIXRD spectra of unirradiated SiC layer and irradiated SiC layers at different damage levels; (c) refined lattice parameter of unirradiated SiC layer and irradiated SiC layers at different damage levels; (d) unit cell linear and volume expansion of irradiated SiC layer at different damage levels.

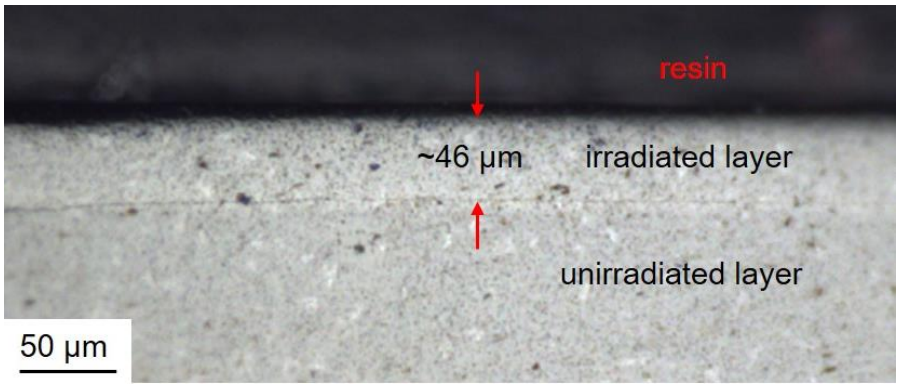

Figure 3. 19 Cross section of proton irradiated SiC disk at the damage level of 0.25 dpa and irradiation temperature of 340 ºC.

Secondly, the damage rate and level could be affected by the density of sintered SiC ceramics according to equation 3.14 but such effects are very small. Specifically, as density decreased from 3.21 g/cm^3 (theoretical density of SiC) to ~3.00 g/cm^3 (density of the sintered SiC ceramics), damage level achieved for the irradiation time of 1 h only increased from 0.050 dpa to 0.053 dpa. The deviation of damage level caused by the pores are much smaller than the difference among the used damage level (0.05 dpa, 0.10 dpa and 0.25 dpa). Therefore, it is suggested to that small amount of pores (porosity of ~6.4%) in sintered SiC ceramics have negligible effects on the damage profile. Ning et al. studied the damage profiles of pure SiC ceramic and SiC ceramic containing 5 vol% ferritic alloy as a sintering additive [13]. Although those SiC ceramics possessed different relative density (99% for pure SiC and 94% for SiC with alloy), they had very similar damage profile in terms of position/height of the Bragg peak. Specifically, the Bragg peak of SiC ceramic with 5 vol.% alloy located at 1.92 μm, which was slightly smaller than that (1.97 um) of pure SiC ceramics. Also, those SiC ceramics had same peak height [13].

According to Figure 3. 17, SiC within the penetrated depth (23.5 μm) is subject to the damage rate which is close to the selected damage rate (marked by red arrow) used to calculate total irradiation time for target damage levels. It is thus reasonable to use the GIXRD result to evaluate effects of damage level on lattice parameter of irradiated SiC layer. According to Figure 3. 18(a), only 3C-SiC (also called as β-SiC) is present in all SiC layers despite damage level. Also, the main peak

representing lattice plane (111) of irradiated SiC layers shifts to lower Bragg angles (2θ) compared with counterpart of unirradiated SiC layer (Figure 3. 18(b)), implying irradiation-induced lattice expansion. Furthermore, extent of peak shift increases with damage level. Pawley fit method programmed in software of PANalytical HighScore Plus is used to fit whole XRD spectrum to refine unit cell lattice parameter (a_i for irradiated SiC layer and a_u for unirradiated SiC layer). Figure 3. 18(c) demonstrates refined lattice parameters. It is noted that goodness of fit (GOF) for all XRD spectra is smaller than 2.1. According to Figure 3. 18(c), higher damage level leads to larger lattice parameters. Unit cell linear expansion (defined as $(a_i - a_u)/a_u$) and unit cell volume expansion (defined as $(a_i^3 - a_u^3)/a_u^3$) of irradiated SiC layers are shown in Figure 3. 18(d). According to Figure 3. 18(d), highest unit cell volume expansion of 1.4075% was obtained in the SiC layer irradiated at highest damage level of 0.25 dpa. The unit cell volume expansion determined by XRD has been proven to be comparable to macroscopic swelling obtained by measuring dimension change after irradiation [18, 41, 42]. Underlying mechanism responsible for unit cell volume expansion will be discussed below.

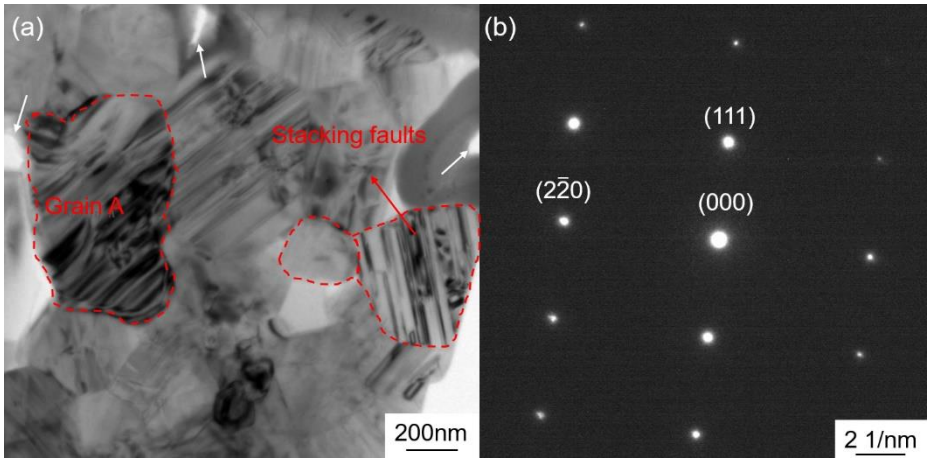

Figure 3. 20 TEM image and electron diffraction pattern of a SiC ceramic sintered at 1850 ºC for 10 min by SPS prior to proton irradiation: (a) bright field TEM image; (b) electron diffraction pattern of the grain A marked in Figure 3. 20(a), beam direction is parallel to the zone axis $[11\bar{2}]$. A red dotted line indicates a grain boundary and a white arrow indicates a pore.

Figure 3. 20 shows bright field TEM image and electron diffraction pattern of a SiC ceramic sintered at 1850 ºC for 10 min by SPS prior to proton irradiation. In Figure 3. 20(a), white arrows indicate

pores while red dotted lines stand for grain boundaries. Grain size of SiC were measured based on several bright field TEM images of the sintered SiC ceramic and is 475 ± 78.8 nm. Some SiC grains contain several parallel lines with grey/dark grey contrast which represent stacking faults [43]. The electron diffraction pattern (Figure 3. 20(b)) of grain A marked in Figure 3. 20(a) has been indexed and demonstrates that grain A is 3C-SiC phase, which is consistent with XRD result (Figure 3. 18(a)). In addition, although stacking faults can be observed in some grains (e.g. grain A), neither extra diffraction spot nor streaking of diffraction spots has been found in the electron diffraction pattern of grain A, suggesting low-density stacking fault is present in the sintered SiC ceramic [44].

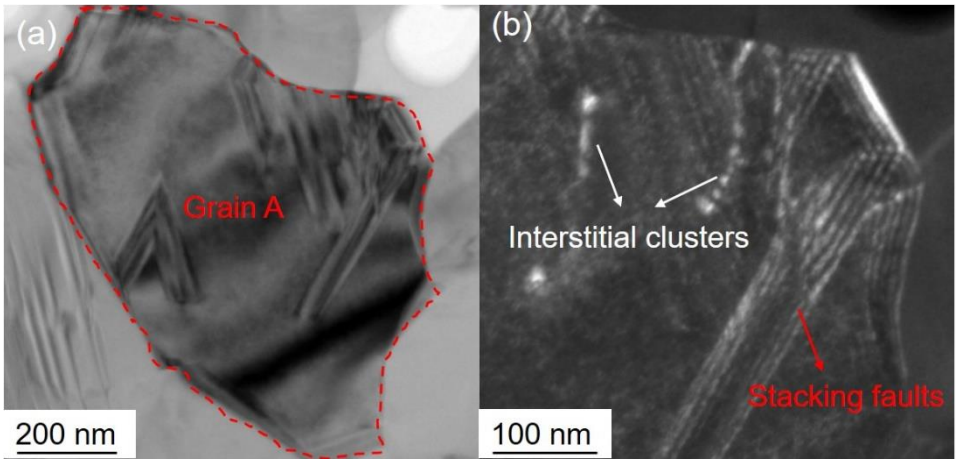

Figure 3. 21 TEM images of the proton irradiated SiC at irradiation temperature of 340 ºC and damage level of ~3.8 dpa: (a) bright field TEM image; (b) weak beam dark field image corresponding to the grain A marked in Figure 3. 21(a). A red dotted line indicates a grain boundary and white dots indicated by white arrows are irradiation induced interstitial clusters.

To study microstructure of irradiated SiC, a thin lamella was prepared by FIB on cross section of the SiC disk irradiated at damage level of 0.25 dpa. Given that proton irradiation results in a non-uniform damage profile in SiC ceramics (as shown in Figure 3. 17), the lamella was specifically made in the central position of Bragg peak which is 46 μm below irradiated surface. Figure 3. 17 shows that the SiC lamella experienced damage level of ~3.8 dpa. Figure 3. 21 shows TEM images of the irradiated SiC at irradiation temperature of 340 ºC and damage level of 3.8 dpa. Figure 3. 21(a) is a bright field image of the irradiated SiC. A red dotted line indicates a grain boundary. Figure 3. 21(b) is weak beam dark field image of the irradiated SiC. The dots with white contrast indicated by white arrows

in Figure 3. 21(b) are irradiation induced small interstitial clusters while parallel lines with white contrast indicated by red arrow are stacking faults [18]. Presence of interstitial clusters may have influence on unit cell volume expansion and thermal conductivity, which will be discussed below. It should be noted that other grains in the SiC lamella have been checked by TEM but neither black spot defects nor interstitials clusters was observed.

3.4.3.2 Thermal conductivity

As mentioned in section 3.4.2.2.2, linear fitting of $\frac{1}{\alpha_d}$ - $\frac{1}{t_d}$ could provide slope and intercept that can be utilized to derive thermal diffusivity of irradiated SiC layer. Thermal diffusivity of unirradiated SiC layer is the reciprocal of intercept (equation 3.17). Thermal diffusivity of irradiated SiC layer can be derived with intercept, slope and constant thickness (46 μm) of irradiated layer (equation 3.17). Figure 3. 22(a), (b) and (c) demonstrate linear fitting results of irradiated SiC disks at damage level of 0.05 dpa, 0.10 dpa and 0.25 dpa respectively. According to Figure 3. 22(a)-(c), relatively good linear fitting on thermal diffusivities of those 3 samples (adjusted R-square > 0.92) can be achieved. Derived thermal diffusivities of unirradiated layer of those 3 samples are 66.1 $\pm$ 1.76 mm^2/s, 68.6 $\pm$ 2.20 mm^2/s and 70.8 $\pm$ 2.84 mm^2/s, which are very close to counterparts of sintered SiC ceramics prior to proton irradiation (shown in Table 3. 7). Fitting quality is hard to be further improved due to limited values (samples are too thin and brittle to withstand multiple grinding process). Derived thermal diffusivities of irradiated SiC layer at different damage levels can be converted to thermal conductivities of irradiated SiC layer with known specific heat and density, which are shown in Figure 3. 22(d).

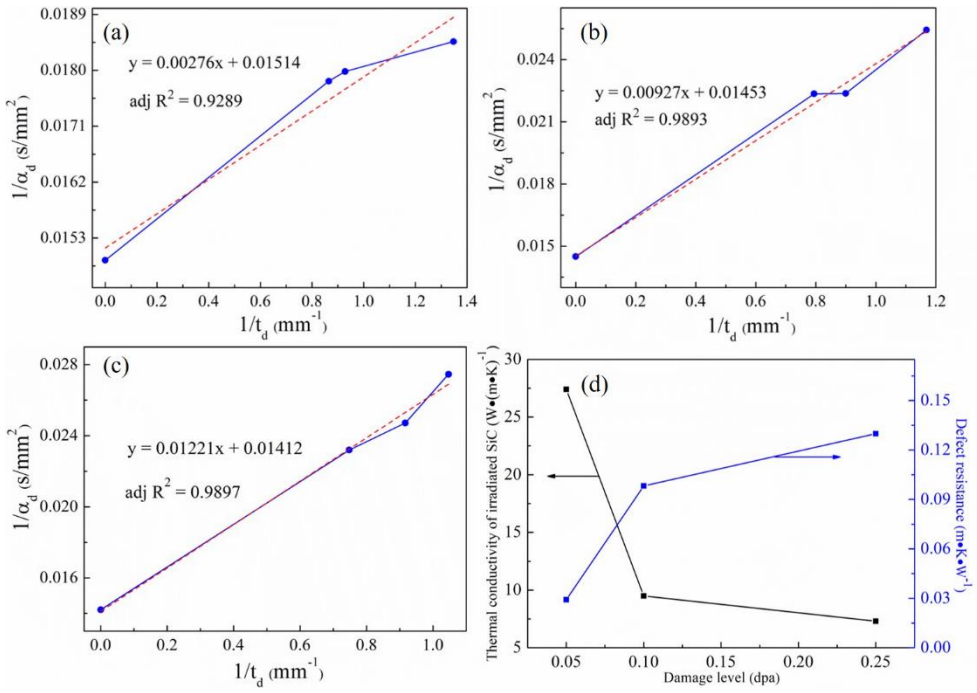

Figure 3. 22 Thermal diffusivity/conductivity at 30 ºC of irradiated SiC disks at different damage levels: (a) linear fitting on SiC disks irradiated at 0.05 dpa; (b) linear fitting on SiC disks irradiated at 0.10 dpa; (c) linear fitting on SiC disks irradiated at 0.25 dpa; (d) thermal conductivity (black line) and defect resistance (blue line) of irradiated SiC layer as a function of damage level. Defect resistance is defined as $(1/K_i - 1/K_u)$, $1/K_i$ and $1/K_u$ are thermal resistivities of irradiated layer and unirradiated layer respectively. Red dotted lines in Figure 3. 22(a), (b) and (c) are fitted lines while solid lines connect experimental data.

According to Figure 3. 22(d), thermal conductivity of irradiated SiC layer are lower than 27.4 W/(m•K) while thermal conductivity of SiC ceramics prior to irradiation are around 138-143 W/(m•K) (Table 3. 7). Specifically, thermal conductivity of irradiated SiC layer at damage level of 0.10 dpa is 9.50 ± 0.53 W/(m•K), which is about 93.3% lower than derived counterpart (141 ± 4.54 W/(m•K)) of unirradiated SiC layer. The 93.3% decrease in thermal conductivity of sintered SiC after proton irradiation at 0.10 dpa and irradiation temperature of 340 °C in this study is similar to that (95% decrease in thermal conductivity) of CVD-SiC after neutron irradiation at same damage level of 0.10 dpa and irradiation temperature of 300 °C [6]. In addition, thermal conductivity degradation increases with increasing damage level. To better correlate thermal conductivity degradation with point defects/defect clusters induced by irradiation in following discussion, thermal conductivity

degradation is described by new term 'defect resistance' (referred to thermal resistivity change after irradiation, i.e. $(\frac{1}{k_i} - \frac{1}{k_u})$) introduced by Snead et al. [6]. Effects of damage level on defect resistance of irradiated SiC layer is shown as the blue line in Figure 3. 22(d). According to Figure 3. 22(d), defect resistance of proton irradiated SiC layer at irradiation temperature of 340 °C in this study increases by 237% (from 0.029 ± 0.0046 (m•K)/W to 0.098 ± 0.0059 (m•K)/W) as damage level is increased by 100% (from 0.05 dpa to 0.10 dpa). Further increase of damage level (from 0.10 dpa to 0.25 dpa) leads to only around 32% increase of defect resistance (from 0.098 ± 0.0059 (m•K)/W to 0.13 ± 0.0077 (m•K)/W).

In addition, defect resistance (0.098 ± 0.0059 (m•K)/W) of proton irradiated SiC layer at irradiation temperature of 340 °C and damage level of 0.1 dpa is higher than counterpart (0.079 (m•K)/W) of neutron irradiated CVD-SiC at irradiation temperature of 300 °C and same damage level [6]. Larger defect resistance (0.098 (m•K)/W versus 0.079 (m•K)/W) of proton irradiated SiC in this study could be possibly attributed to non-uniform damage profile in proton irradiated SiC. The derived thermal conductivity by serial model is an average value of irradiated SiC layer which consists of plateau part exposed to target damage level and Bragg's peak exposed to much higher damage level (as shown in Figure 3. 17). In contrast, uniform damage profile was present in neutron irradiated CVD-SiC. Future work includes characterization of thermal conductivity of the plateau part in irradiated SiC layer exposed to target damage level by more appropriate method (e.g. Time-domain thermoreflectance) [45].

3.4.4 Discussion

Above results demonstrate that proton irradiation leads to swelling described by unit cell volume expansion and significant thermal conductivity degradation described by defect resistance. Furthermore, both volume expansion and defect resistance increase with damage level but increase extent at low damage level of 0.05-0.10 dpa is higher than that at high damage level (0.10-0.25 dpa). Following discussion mainly focus on underlying mechanism responsible for volume expansion and defect resistance as well as their dependence on damage level. It is noted that due to small size (atomic scale) of irradiation induced point defects and relative low damage level of 0.05-0.25 dpa in

this study, it is difficult to distinguish and quantify different type of defects only based on experimental data. Hence, following discussion involves not only experimental data but also theoretically work about defect evolution.

3.4.4.1 Defect evolution during proton irradiation

Displacement cascade is initiated when high energy particles (e.g. neutron, proton and electron) collide with an atom in a lattice, which results in formation of different types of irradiation induced defects/defect clusters [46]. Ab initio molecular dynamics (AIMD) calculation results showed that displacement threshold energy required for creating different types of defects in C sublattice is 20 eV which is 43% lower than counterpart (35 eV) in Si sublattice [29]. It is thus expected that more defects in C sublattice will be generated during irradiation. Moreover, recombination and clustering of irradiated induced defects evolve progressively and have significant effects on defect evolution during irradiation.

Recombination and clustering of irradiation induced defects are determined by migration energy of different defect types. Density functional theory (DFT) was used to calculate migration energies of different types of defects. It was found that vacancy-type defects and antisite-type defects had much higher migration energies than counterparts of interstitial-type defects [47]. For instance, migration energies of neutral Si and C vacancies are around 3.5 eV and change with charge state of vacancy. Migration energies of antisite defects (e.g. Si_C and C_{Si}) are between 3.6 eV and 4.0 eV [48]. Migration energies of vacancy-type defects and antisite-type defects are so high that they can be considered as immobile at irradiation temperature of 340 °C in this study. Such limited mobility of vacancy-type defects below 790 °C were also verified by positron annihilation spectroscopy [17]. In comparison, migration energies of C and Si interstitials are between 0.67-0.89 eV, which is very similar to counterparts in metals [47]. Migration energies of interstitial-type defects are so low that they possessed observable mobility at very low temperature (30 °C) [6]. In summary, at investigated irradiation temperature (340 °C), interstitials of C and Si are highly mobile while antisite defects (e.g. Si_C and C_{Si}) and vacancy type defects (e.g. V_C and V_{Si}) are immobile. High mobility of interstitial type defects could promote not only annihilation of corresponding vacancy but also formation and growth

of interstitial clusters because interstitial clusters result in lower strain energy than that of same amount of single interstitial defect [6]. MD simulation results showed that 81% single point defect (e.g. V_C, Si_C, C_{Si}, and V_{Si}) and 19% interstitial clusters containing up to 4 interstitials were survived after SiC was irradiated by 50 KeV Si atom at 300 K [14].

Despite migration energy, energy barrier for recombination reaction is another important factor that contributes to defect evolution, which could be obtained by DFT. For example, DFT calculation results showed that energy barrier for annihilation of C interstitial and C vacancy is 0.92 eV that is much higher than counterpart (0.03 eV) for annihilation of Si interstitial and Si vacancy [47, 49]. Lower displacement threshold energy in C sublattice of SiC and higher energy barrier for annihilation of C defects together result in more C type defects than Si type defects in irradiated SiC. Such expectation was confirmed by Molecular dynamics (MD) simulations. It was reported that the number of surviving Si vacancies and interstitials after displacement cascade was less than third of C vacancies and interstitials [14, 50].

Although there is lack of MD simulations on proton irradiation effects on SiC, final defect characteristics of proton irradiated SiC at 340 °C could be speculated based on displacement threshold energy, migration energy and energy barrier for recombination reaction. At proton irradiation temperature of 340 °C, number of point defects/defects clusters after short time displacement cascades should be in a decreasing sequence as follows: C Frenkel pairs (V_C and C interstitial), Si_C/C_{Si}, Si Frenkel pair (V_{Si} and Si interstitial), interstitial clusters of C-rich or Si-rich [14, 47, 51]. In addition, it should be mentioned that long-time defect evolution are impossible to be obtained by MD simulations due to their intrinsic time-scale limitations (from picoseconds to nanoseconds) so MD simulation results about defect evolution during irradiation are suitable for low damage level [2, 52]. Given low damage level adopted in this study ($\leq$ 0.25 dpa), it is therefore reasonable to use above speculation to describe lattice defects in irradiated SiC that will be correlated to unit cell volume expansion and defect resistance (thermal conductivity degradation).

3.4.4.2 Proton irradiation induced volume expansion

Swelling is a common phenomenon in neutron/ion irradiated SiC ceramics and used to evaluate dimensional stability [7, 53]. For proton irradiated SiC disks at irradiation temperature of 340 °C in this study, swelling is verified by unit cell volume expansion obtained from GIXRD spectra (Figure 3. 18(d)). The unit cell volume expansion of proton irradiated SiC at damage level of 0.1 dpa is around 0.78%, which is smaller than counterpart (~1.29%) of neutron irradiated CVD-SiC at same damage level and a slightly higher irradiation temperature of 380 °C [18]. The volume expansion difference between proton irradiated SiC and neutron irradiated SiC cannot be explained in terms of damage rate. It was reported that lower damage rate of neutron irradiation compared with counterpart of proton irradiation at same damage level could be balanced in principle by lower irradiation temperature to achieve similar microstructure for stainless steel used in nuclear reactors [9]. If this applies to SiC ceramics, it could be inferred that at same damage level of 0.1 dpa microstructure of neutron irradiated SiC at irradiation temperature 380 °C should be similar to counterpart of proton irradiated SiC at higher irradiation temperature. Generally, higher irradiation temperature leads to higher mobility of interstitials and more annihilation of interstitial and corresponding vacancy, resulting in less irradiation-induced defects and lower volume expansion. However, volume expansion in proton-irradiated SiC disk at 340 °C and damage level of 0.1 dpa is lower than reported counterpart of neutron irradiated SiC at 380 °C and same damage level. Hence, lower unit cell volume expansion of proton irradiated SiC cannot be attributed to higher damage rate of proton irradiation than that of neutron irradiation. It is noted that proton irradiated SiC in this study is not fully dense (relative density of ~93.6%) while fully dense CVD-SiC is used in neutron irradiated SiC in reference [18]. It is suggested that pores in sintered SiC ceramics irradiated by proton in this study might provide space to relax volume expansion caused by irradiation induced defects/defect clusters and thus result in lower volume expansion compared with counterpart of neutron irradiated fully dense SiC [54, 55].

Although different types of defects/defect clusters generated after proton irradiation, it is still necessary to figure out contributions of different defects/defect clusters on volume expansion of SiC

ceramics. Excess volumes of point defect/defect clusters (defined as volume difference between perfect unit cell and unit cell with defects/defect clusters) have been calculated by MD simulation [56]. It was found that excess volumes of Si interstitials and C interstitials were 27.88-37.22 X 10^{-30} m^3 and 15.33-16.48 X 10^{-30} m^3 respectively. In comparison, excess volumes of Si vacancy and C vacancy were 1.85 X 10^{-30} m^3 and 2.68 X 10^{-30} m^3 respectively [56]. Based on excess volume and numbers of the irradiation induced defects, one could speculate that interstitials of C and Si make greatest contribution to lattice expansion and vacancy of C and Si almost does not have effects on volume expansion. Hu et al. also verified vacancy-type defects made minimal contribution to swelling of irradiated SiC [17].

In addition, important contribution of interstitial clusters to lattice expansion should also be considered especially at relatively high damage level [57]. With increasing damage level, irradiation induced interstitials not only actively involve into recombination reactions but also promotes formation and growth of immobile interstitial clusters due to reduction of total strain energy and relatively low defect binding energy of interstitial clusters [6]. Figure 3. 21(b) confirms that interstitial clusters are present in the proton irradiated SiC at high damage level of 3.8 dpa. It may be speculated that interstitial clusters should contribute less to unit cell volume expansion than counterpart of same number of single interstitials. Yano et al. found that volume expansion of neutron irradiated SiC at irradiation temperature of 500 °C could be relaxed after annealing the sample above 500 °C. The lower volume expansion after annealing was accompanied by microstructural transition from black spot defects (smaller interstitial clusters) to well-developed Frank dislocation loops (larger interstitial clusters), indicating that growth of interstitial clusters could reduce volume expansion [58]. Thus, it is expected that unit cell volume expansion increases with damage level but increase extent gradually decrease with increasing damage level due to formation and growth of interstitial clusters. Such expectation is consistent with volume expansion dependence on damage level (Figure 3. 18(d)) in this study. In summary, interstitial-type defects make dominant contribution to unit cell volume expansion of proton irradiated SiC at 340 °C and contribution from interstitial clusters increases with damage level.

3.4.4.3 Damage level effects on defect resistance

Defect resistance was correlated to defect type, size and density (concentration) based on simplified Callaway models [6, 59, 60]. Effects of defects types on defect resistance could be examined by MD simulation methods. Crocombette et al. adopted equilibrium molecular dynamics (EMD) simulation to calculate defect resistance caused by different types of defects and one special defect cluster (V_C-Si_C) [61, 62]. It was found that defect resistance caused by a type of radiation-induced point defect was proportional to its concentration. The proportional coefficient was mainly determined by defect type [62]. For instance, Si type defects (e.g. V_{Si} and Si_{TSi}) caused higher defect resistance than counterparts of corresponding C type defects at same concentration. The Si interstitial surrounded by Si tetrahedra (Si_{TSi}) possessed highest proportional coefficient of around 3.2 (m•K)/W which is 2.5 times as that of C interstitial surrounded by Si tetrahedra (C_{TSi}) [62]. Given that proportional coefficient (< 0.5 (m•K)/W) of antisite defects (e.g. C_{Si} and Si_C) at 300 K were smaller than counterparts (> 1.25 (m•K)/W) of interstitials and vacancies, contribution from antisite defects in defect resistance is ignored. As mentioned above in section 3.4.4.1, interstitials of C and Si are highly mobile while vacancy type defects (e.g. V_C and V_{Si}) are immobile, it has been always simply assumed that vacancy type defects dominated defect resistance in irradiated SiC [6, 62]. The assumption about vacancy dominating defect resistance might not be reasonable for SiC ceramics exposed to high damage level (>0.1 dpa) because increasing damage level promotes formation and growth of interstitial clusters and more contribution from interstitial clusters to thermal conductivity degradation are expected. Figure 3. 21(b) confirms that interstitial clusters are present in the proton irradiated SiC at high damage level of 3.8 dpa. Considering the defect cluster (V_C-Si_C) has slightly lower proportional coefficient (2.41 (m•K)/W) than that (3.09 (m•K)/W) of Si vacancy (V_{Si}) [62], relatively lower increase extent of defect resistance at high damage level of 0.10-0.25 dpa compared with that at low damage level of 0.05-0.10 dpa (Figure 3. 22(d)) in this study is suggested to be caused by more contribution from interstitial clusters. In summary, large defect resistance (significant thermal conductivity degradation) of proton irradiated SiC in this study is mainly caused by vacancy-type defects and interstitial clusters. It is also suggested that contribution from interstitial clusters to total defect resistance increases with damage level.

3.4.5 Conclusions

In this study, SiC ceramics with relative density of 93% were fabricated by SPS and subsequently exposed to proton irradiation at irradiation temperature of 340 °C and damage level of 0.05, 0.10 and 0.25 dpa. Evolution of microstructure and thermal conductivity after proton irradiation were studied and conclusion can be summarized as follows:

(1) The unit cell volume expansion (0.47%-1.41%) and significant thermal conductivity reduction (79.9%-95% lower than that of unirradiated SiC) after proton irradiation were verified by X-ray diffraction and laser flash technique respectively. Such volume expansion and thermal conductivity degradation have been correlated with point defects (i.e. vacancy-type defects and interstitial-type defects) and interstitial clusters induced by proton irradiation via combing TEM data with theoretical simulation from literature. It is suggested that interstitial-type defects make dominant contribution to unit cell volume expansion of proton irradiated SiC because of their much high excess volume (volume difference between perfect unit cell and unit cell with defects) while vacancy-type defects and interstitial clusters are responsible for significant thermal conductivity degradation.

(2) Furthermore, higher damage level resulted in higher volume expansion and lower thermal conductivity but variation extent of volume expansion and thermal conductivity at high damage level of 0.10-0.25 dpa was smaller than that at low damage level of 0.05-0.10 dpa, which is suggested to be caused by more contribution from interstitial clusters at high damage level.

(3) The evolution of microstructures and thermal conductivity of proton-irradiated SiC have demonstrated similarities with the counterparts of neutron irradiated SiC ceramics, suggesting the possibility of substituting neutron irradiation with proton irradiation which would make it easier to fundamentally depict the evolution mechanism of a number of properties of SiC ceramics under nuclear environment.

References

[1] N.S. Jacobson, D.L. Myers, Active oxidation of SiC, Oxidation of metals 75(1-2) (2011) 1-25.

[2] C. Jiang, D. Morgan, I. Szlufarska, Structures and stabilities of small carbon interstitial clusters in cubic silicon carbide, Acta materialia 62 (2014) 162-172.

[3] L.L. Snead, T. Nozawa, Y. Katoh, T.-S. Byun, S. Kondo, D.A. Petti, Handbook of SiC properties for fuel performance modeling, Journal of nuclear materials 371(1-3) (2007) 329-377.

[4] K. Yueh, K.A. Terrani, Silicon carbide composite for light water reactor fuel assembly applications, Journal of Nuclear Materials 448(1-3) (2014) 380-388.

[5] S.J. Zinkle, K.A. Terrani, J.C. Gehin, L.J. Ott, L.L. Snead, Accident tolerant fuels for LWRs: A perspective, Journal of Nuclear Materials 448(1-3) (2014) 374-379.

[6] L. Snead, S. Zinkle, D. White, Thermal conductivity degradation of ceramic materials due to low temperature, low dose neutron irradiation, Journal of nuclear materials 340(2-3) (2005) 187-202.

[7] L.L. Snead, Y. Katoh, S. Connery, Swelling of SiC at intermediate and high irradiation temperatures, Journal of nuclear materials 367 (2007) 677-684.

[8] W. Jiang, H. Wang, I. Kim, Y. Zhang, W.J. Weber, Amorphization of nanocrystalline 3C-SiC irradiated with Si+ ions, Journal of Materials Research 25(12) (2010) 2341-2348.

[9] G. Was, J. Busby, T. Allen, E. Kenik, A. Jensson, S. Bruemmer, J. Gan, A. Edwards, P. Scott, P. Andreson, Emulation of neutron irradiation effects with protons: validation of principle, Journal of nuclear materials 300(2-3) (2002) 198-216.

[10] P. Wady, A. Draude, S. Shubeita, A. Smith, N. Mason, S. Pimblott, E. Jimenez-Melero, Accelerated radiation damage test facility using a 5 MV tandem ion accelerator, Nuclear Instruments and Methods in Physics Research Section A: Accelerators, Spectrometers, Detectors and Associated Equipment 806 (2016) 109-116.

[11] C. Liu, B. Chen, X. Li, Y. Zhao, Effects of proton irradiation on the microstructure and mechanical properties of Amosic-3 silicon carbide minicomposites, Journal of Materials Science & Technology 35(12) (2019) 2935-2941.

[12] X. Wang, H. Zhang, T. Baba, H. Jiang, C. Liu, Y. Guan, O. Elleuch, T. Kuech, D. Morgan, J.-C. Idrobo, Radiation-induced segregation in a ceramic, Nature Materials (2020) 1-7.

[13] K. Ning, K. Lu, Ion irradiation effect on spark plasma sintered silicon carbide ceramics with nanostructured ferritic alloy aid, Journal of the American Ceramic Society 101(8) (2018) 3662-3673.

[14] F. Gao, W.J. Weber, Atomic-scale simulation of 50 keV Si displacement cascades in β-SiC, Physical Review B 63(5) (2000) 054101.

[15] T. Yano, T. Iseki, High-resolution electron microscopy of neutron-irradiation-induced dislocations in SiC, Philosophical Magazine A 62(4) (1990) 421-430.

[16] Y. Katoh, N. Hashimoto, S. Kondo, L. Snead, A. Kohyama, Microstructural development in cubic silicon carbide during irradiation at elevated temperatures, Journal of nuclear materials 351(1-3) (2006) 228-240.

[17] X. Hu, T. Koyanagi, Y. Katoh, B.D. Wirth, Positron annihilation spectroscopy investigation of vacancy defects in neutron-irradiated 3C-SiC, Physical Review B 95(10) (2017) 104103.

[18] D.J. Sprouster, T. Koyanagi, E. Dooryhee, S. Ghose, Y. Katoh, L.E. Ecker, Microstructural evolution of neutron irradiated 3C-SiC, Scripta Materialia 137 (2017) 132-136.

[19] M. Rohde, Reduction of the thermal conductivity of SiC by radiation damage, Journal of Nuclear Materials 182 (1991) 87-92.

[20] Y. Katoh, T. Nozawa, L.L. Snead, K. Ozawa, H. Tanigawa, Stability of SiC and its composites at high neutron fluence, Journal of Nuclear Materials 417(1-3) (2011) 400-405.

[21] T. Yamamoto, H. Kitaura, Y. Kodera, T. Ishii, M. Ohyanagi, Z.A. Munir, Consolidation of nanostructured β‐SiC by spark plasma sintering, Journal of the American ceramic Society 87(8) (2004) 1436-1441.

[22] M. Mulla, V. Krstic, Mechanical properties of β-SiC pressureless sintered with Al_2O_3 additions, Acta metallurgica et materialia 42(1) (1994) 303-308.

[23] J.S. Lee, Y.S. Ahn, T. Nishimura, H. Tanaka, S.H. Lee, Ultra‐Low‐Temperature Sintering of Nanostructured β-SiC, Journal of the American Ceramic Society 94(2) (2011) 324-327.

[24] M.I. Idris, S. Yamazaki, K. Yoshida, T. Yano, Defects annihilation behavior of neutron-irradiated SiC ceramics densified by liquid-phase-assisted method after post-irradiation annealing, Nuclear Materials and Energy 9 (2016) 199-206.

[25] T. Koyanagi, S. Kondo, T. Hinoki, The influence of sintering additives on the irradiation resistance of NITE SiC, Journal of nuclear materials 417(1-3) (2011) 435-439.

[26] C.M. Parish, K.A. Terrani, Y.-J. Kim, T. Koyanagi, Y. Katoh, Microstructure and hydrothermal corrosion behavior of NITE-SiC with various sintering additives in LWR coolant environments, Journal of the European Ceramic Society 37(4) (2017) 1261-1279.

[27] T. Cheng, J.R. Keiser, M.P. Brady, K.A. Terrani, B.A. Pint, Oxidation of fuel cladding candidate materials in steam environments at high temperature and pressure, Journal of Nuclear Materials 427(1-3) (2012) 396-400.

[28] R.E. Stoller, M.B. Toloczko, G.S. Was, A.G. Certain, S. Dwaraknath, F.A. Garner, On the use of SRIM for computing radiation damage exposure, Nuclear instruments and methods in physics research section B: beam interactions with materials and atoms 310 (2013) 75-80.

[29] R. Devanathan, W.J. Weber, F. Gao, Atomic scale simulation of defect production in irradiated 3C-SiC, Journal of Applied Physics 90(5) (2001) 2303-2309.

[30] M.I. Mendelson, Average grain size in polycrystalline ceramics, Journal of the American Ceramic society 52(8) (1969) 443-446.

[31] W. Parker, R. Jenkins, C. Butler, G. Abbott, Flash method of determining thermal diffusivity, heat capacity, and thermal conductivity, Journal of applied physics 32(9) (1961) 1679-1684.

[32] I. Barin, Thermochemical data of pure substances, VCH (1989).

[33] C. Lee, F. Pineau, J. Corelli, Thermal properties of neutron-irradiated SiC; effects of boron doping, Journal of Nuclear Materials 108 (1982) 678-684.

[34] D. Hasselman, L.F. Johnson, Effective thermal conductivity of composites with interfacial thermal barrier resistance, Journal of composite materials 21(6) (1987) 508-515.

[35] S. Dong, D. Jiang, S. Tan, J. Guo, Preparation and characterization of nano-structured monolithic SiC and Si3N4/SiC composite by hot isostatic pressing, Journal of materials science letters 16(13) (1997) 1080-1083.

[36] K. Raju, D.-H. Yoon, Sintering additives for SiC based on the reactivity: a review, Ceramics International 42(16) (2016) 17947-17962.

[37] K. Biswas, Solid state sintering of SiC-ceramics, Materials Science Forum, Trans Tech Publ, (2009), 71-89.

[38] E. Ermer, P. Wiesław, S. Ludosław, Influence of sintering activators on structure of silicon carbide, Solid state ionics 141 (2001) 523-528.

[39] Z. Munir, U. Anselmi-Tamburini, M. Ohyanagi, The effect of electric field and pressure on the synthesis and consolidation of materials: A review of the spark plasma sintering method, Journal of materials science 41(3) (2006) 763-777.

[40] Y.-W. Kim, S. Kultayeva, J. Sedláček, O. Hanzel, P. Tatarko, Z. Lenčéš, P. Šajgalík, Thermal and electrical properties of additive-free rapidly hot-pressed SiC ceramics, Journal of the European Ceramic Society 40(2) (2020) 234-240.

[41] G. Newsome, L.L. Snead, T. Hinoki, Y. Katoh, D. Peters, Evaluation of neutron irradiated silicon carbide and silicon carbide composites, Journal of Nuclear Materials 371(1-3) (2007) 76-89.

[42] T. Koyanagi, M. Lance, Y. Katoh, Quantification of irradiation defects in beta-silicon carbide using Raman spectroscopy, Scripta Materialia 125 (2016) 58-62.

[43] L. Ogbuji, T. Mitchell, A. Heuer, The β→αTransformation in poly crystalline SiC: III, the thickening of α plates, Journal of the American Ceramic Society 64(2) (1981) 91-99.

[44] W.S. Seo, K. Koumoto, Stacking Faults in β-SiC Formed during Carbothermal Reduction of SiO2, Journal of the American Ceramic Society 79(7) (1996) 1777-1782.

[45] M. Khafizov, C. Yablinsky, T.R. Allen, D.H. Hurley, Measurement of thermal conductivity in proton irradiated silicon, Nuclear Instruments and Methods in Physics Research Section B: Beam Interactions with Materials and Atoms 325 (2014) 11-14.

[46] A. Aitkaliyeva, L. He, H. Wen, B. Miller, X.-M. Bai, T. Allen, Irradiation effects in Generation IV nuclear reactor materials, Structural Materials for Generation IV Nuclear Reactors, Elsevier (2017), 253-283.

[47] N. Swaminathan, D. Morgan, I. Szlufarska, Role of recombination kinetics and grain size in radiation-induced amorphization, Physical Review B 86(21) (2012) 214110.

[48] M. Bockstedte, A. Mattausch, O. Pankratov, Ab initio study of the migration of intrinsic defects in 3 C− SiC, Physical Review B 68(20) (2003) 205201.

[49] G. Roma, J.-P. Crocombette, Evidence for a kinetic bias towards antisite formation in SiC nano-decomposition, Journal of nuclear materials 403(1-3) (2010) 32-41.

[50] R. Devanathan, W.J. Weber, T.D. de La Rubia, Computer simulation of a 10 keV Si displacement cascade in SiC, Nuclear Instruments and Methods in Physics Research Section B: Beam Interactions with Materials and Atoms 141(1-4) (1998) 118-122.

[51] G.D. Samolyuk, Y. Osetsky, R.E. Stoller, Molecular dynamics modeling of atomic displacement cascades in 3C–SiC: Comparison of interatomic potentials, Journal of Nuclear Materials 465 (2015) 83-88.

[52] Y. Katoh, L.L. Snead, I. Szlufarska, W.J. Weber, Radiation effects in SiC for nuclear structural applications, Current Opinion in Solid State and Materials Science 16(3) (2012) 143-152.

[53] A. Debelle, A. Boulle, A. Chartier, F. Gao, W.J. Weber, Interplay between atomic disorder, lattice swelling, and defect energy in ion-irradiation-induced amorphization of SiC, Physical Review B 90(17) (2014) 174112.

[54] Y. Katoh, T. Koyanagi, J.L. McDuffee, L.L. Snead, K. Yueh, Dimensional stability and anisotropy of SiC and SiC-based composites in transition swelling regime, Journal of Nuclear Materials 499 (2018) 471-479.

[55] T. Koyanagi, Y. Katoh, Mechanical properties of SiC composites neutron irradiated under light water reactor relevant temperature and dose conditions, Journal of Nuclear Materials 494 (2017) 46-54.

[56] J. Li, L. Porter, S. Yip, Atomistic modeling of finite-temperature properties of crystalline β-SiC: II. Thermal conductivity and effects of point defects, Journal of Nuclear Materials 255(2-3) (1998) 139-152.

[57] C. Liu, L. He, Y. Zhai, B. Tyburska-Püschel, P. Voyles, K. Sridharan, D. Morgan, I. Szlufarska, Evolution of small defect clusters in ion-irradiated 3C-SiC: Combined cluster dynamics modeling and experimental study, Acta Materialia 125 (2017) 377-389.

[58] T. Yano, T. Suzuki, T. Maruyama, T. Iseki, Microstructure and annealing behavior of heavily neutron-irradiated β-SiC, Journal of Nuclear Materials 155 (1988) 311-314.

[59] J. Callaway, Model for Lattice Thermal Conductivity at Low Temperatures, Physical Review 113(4) (1959) 1046-1051.

[60] T.M. Tritt, Thermal conductivity: theory, properties, and applications, Springer Science & Business Media (2005).

[61] T. Lingner, S. Greulich-Weber, J.-M. Spaeth, U. Gerstmann, E. Rauls, Z. Hajnal, T. Frauenheim, H. Overhof, Structure of the silicon vacancy in 6 H− SiC after annealing identified as the carbon vacancy–carbon antisite pair, Physical Review B 64(24) (2001) 245212.

[62] J.-P. Crocombette, L. Proville, Thermal conductivity degradation induced by point defects in irradiated silicon carbide, Applied Physics Letters 98(19) (2011) 191905.

Chapter 4 Conclusions and future work

4.1 Conclusions

The aim of this project was to further understand the influences of sintering additive, microstructure, and proton irradiation on thermal conductivity of spark plasma sintered SiC ceramics. The thesis consists of three articles: In article I, the influences of grain size, sintering additive distribution and content on thermal conductivity of SiC ceramics with Al_2O_3-Y_2O_3 were discussed in detail; In article II, the sintering additive Al_2O_3-Y_2O_3 was substituted with Y_2O_3-Sc_2O_3 due to the negative role of Al in reducing thermal conductivity. Then grain growth was studied and correlated with thermal conductivity of SiC ceramics with Y_2O_3-Sc_2O_3. In article III, pure SiC ceramics without sintering additives were adopted to investigate microstructure and thermal conductivity evolution after proton irradiation.

Article I studied thermal conductivity of SiC ceramics sintered by SPS at 1650-1750 °C for 10-60 min with 3-10 wt.% Al_2O_3-Y_2O_3 as a sintering additive. When the holding time was increased from 10 min to 60 min, discrete distribution of sintering additive was replaced by the continuous sintering additive network, as confirmed by HAADF and STEM-EDS results. Presence of such continuous sintering additive network could increase interfacial thermal resistance and decreases thermal conductivity from 104 ± 0.54 W/(m•K) to 96.6 ± 0.42 W/(m•K). For the SiC ceramics composed of continuous SiC matrix and discrete secondary phase (YAG), when sintering additive content was increased from 3 wt.% to 10 wt.%, grain size and thermal conductivity decreased. Importance of grain size and sintering additive content were evaluated via combining experimental data with the Hasselman and Johnson model. It was found that the decrease in grain size plays a dominant role in reducing the thermal conductivity of the SiC ceramic with the higher sintering additive content. The results suggest that grain size is an important factor controlling thermal conductivity.

In article II, grain growth of SiC ceramics was studied and correlated with thermal conductivity. The SiC ceramics were fabricated by SPS at final sintering temperature of 1750-1850 ºC for 5-240 min with 3 wt.% Y_2O_3-Sc_2O_3 as a sintering additive. Grain growth were affected by holding time and final sintering temperature. At 1850 ºC, rapid grain growth from 0.71 ± 0.06 μm to 1.39 ± 0.31 μm

(dynamic Ostwald ripening) takes place in initial 5 min followed by moderate grain growth from 1.39 ± 0.29 μm to 2.00 ± 0.54 μm (static Ostwald ripening) in rest 110 min of isothermal periods. At 1750 ºC, only static ripening is observed. The dominant grain growth mechanism during static ripening process changes from interface reaction at 1750 ºC to atom diffusion at 1850 ºC.

Moreover, underlying mechanism for the higher thermal conductivity of SiC ceramics with larger grain size were figured out via combining experimental data with the Eastman model. It was found that grain growth not only reduced the number of grain boundary per unit volume but also resulted in lattice purification, as verified by STEM-EDS analysis. Both of them are suggested to be responsible for the high thermal conductivity. The results suggest that thermal conductivity of sintered SiC ceramics could be further increased by selecting sintering additives which are insoluble in SiC lattice and could effectively remove oxygen impurity from starting SiC powders.

Article III investigates the microstructure and thermal conductivity evolution of pure SiC ceramics exposed to proton irradiation at damage level of 0.05-0.25 dpa and temperature of 340 °C. Unit cell volume expansion of 0.47%-1.41% was confirmed by XRD and significant thermal conductivity reduction (79.9%-95% lower than that of unirradiated SiC) was observed by laser flash technique. Furthermore, the volume expansion and thermal conductivity degradation were correlated with irradiation induced point defects/defect clusters described via combing TEM data with theoretical simulation from literature. It is suggested that interstitial-type defects dominate unit cell volume expansion because of their much high excess volume (volume difference between perfect unit cell and unit cell with defects) while vacancy-type defects and interstitial clusters are responsible for significant thermal conductivity degradation. In addition, increasing damage level led to larger volume expansion and lower thermal conductivity and the degree of variability of volume expansion and thermal conductivity reduction decreases with increasing damage level, implying more contribution from interstitial clusters at high damage level. Article III is the preliminary study about effects of proton irradiation on SiC ceramics, which explored the potential of simulating neutron irradiation using proton irradiation. The evolution of microstructures and thermal conductivity of proton-irradiated SiC have demonstrated similarities with the counterparts of neutron irradiated SiC ceramics, suggesting the possibility of substituting neutron irradiation with proton irradiation which would make it easier to

fundamentally depict the evolution mechanism of a number of properties of SiC ceramics under nuclear environment.

Overall, the thesis has further the understanding about how sintering additive and microstructure affect thermal conductivity of SiC ceramics and has investigated for the first time on how proton irradiation influences microstructure and thermal conductivity of spark plasma sintered SiC ceramics.

4.2 Future work

(1) Study sintering additive distribution of the SiC sintered with 10 wt.% Al_2O_3-Y_2O_3 for 10 min

The conclusion of Article I shows that sintering additive distribution changes with holding time based on HAADF and STEM-EDS results of the SiC ceramics with 3 wt.% Al_2O_3-Y_2O_3. HAADF and STEM-EDS work should be carried out in the sintered SiC ceramic with 10 wt.% Al_2O_3-Y_2O_3 for 10 min to further verify sintering additive distribution is determined by holding time rather than sintering additive content.

(2) Study effects of rare-earth cation radius on thermal conductivity of sintered SiC ceramics

The conclusion of Article II shows that rare-earth oxide (Y_2O_3-Sc_2O_3) could remove oxygen impurity of starting SiC powders and result in lattice purification during grain growth. Given the ability of getting oxygen is highly related to radius of rare-earth cations, it is inspiring to fabricate SiC ceramics with different types of single rare-earth oxide to not only correlate rare-earth cation radius with lattice purification but also achieve higher thermal conductivity.

(3) Quantify irradiation induced defects using Raman spectroscopy

In Article III, although irradiation induced defects with very small size (atomic scale) are not visible in conventional TEM, they can result in shift and broadening of longitudinal optical peak in Raman spectra of irradiated SiC [1-3]. Quantification of such peak changes in Raman spectra could roughly estimate distance between invisible defects.

References

[1] T. Koyanagi, Y. Katoh, M.J. Lance, Raman spectroscopy of neutron irradiated silicon carbide: Correlation among Raman spectra, swelling, and irradiation temperature, Journal of Raman Spectroscopy 49(10) (2018) 1686-1692.

[2] T. Koyanagi, M. Lance, Y. Katoh, Quantification of irradiation defects in beta-silicon carbide using Raman spectroscopy, Scripta Materialia 125 (2016) 58-62.

[3] X. Chen, W. Zhou, Q. Feng, J. Zheng, X. Liu, B. Tang, J. Li, J. Xue, S. Peng, Irradiation effects in 6H–SiC induced by neutron and heavy ions: Raman spectroscopy and high-resolution XRD analysis, Journal of Nuclear Materials 478 (2016) 215-221.